

STUDIES ON MEMBRANE PROTEIN FOLDING
BY SURFACE ENHANCED INFRARED
ABSORPTION SPECTROSCOPY

INAUGURAL DISSERTATION
to obtain the academic degree
Doctor rerum naturalium (Dr. rer. nat.)
submitted to the Department of Biology, Chemistry and Pharmacy
of Freie Universität Berlin

by
Axel Baumann
from Meißen

2017

This thesis was conducted from April 16, 2012 until May 15, 2018, with an interruption between January 01, 2015 until July 31, 2016. It was supervised by Dr. Ramona Schlesinger, Freie Universität Berlin, Institute of Experimental Physics - Genetic Biophysics

1. Reviewer: Dr. Ramona Schlesinger
Freie Universität Berlin
Department of Physics
Institute of Experimental Physics - Genetic Biophysics

2. Reviewer: Prof. Dr. Markus Wahl
Freie Universität Berlin
Department of Biology, Chemistry and Pharmacy
Institute of Chemistry and Biochemistry - Biochemistry

Disputation on December 21, 2017

Danksagung

Da sich meine Doktorarbeit widererwarten eher unkonventionell gestaltet hat, möchte ich an dieser Stelle einer Vielzahl von Personen meinen ganz besonderen Dank aussprechen. Als erstes möchte ich explizit Frau Dr. Ramona Schlesinger für die Übernahme der Betreuung meiner Doktorarbeit danken. Während meiner Anstellung am Forschungszentrum Jülich GmbH in der Gruppe von Herrn Prof. Georg Büldt, der mich leider nicht mehr als Doktorand übernehmen konnte, lernte ich Ramona kennen, woraus sich sehr ergiebige und angenehme Kooperationsarbeiten entwickelten. In meiner Zeit in Jülich konnte ich leider aus mehreren Gründen mein damaliges Projekt nicht mit einer Promotionschrift abschließen. Jedoch durch die Kooperation und dann später sogar Übernahme meiner Betreuung mit und durch federführend Ramona, kann ich nun diese Danksagung in meiner beendeten Thesis verfassen. Vielen Dank Ramona! Eine weitere diesbgl. wichtige Person ist Herr Prof. Markus Wahl, dem ich für die Bereiterklärung der Zweitbegutachtung danken möchte. Dies gilt vorausnehmend natürlich auch für die anderen Mitglieder der Prüfungskommission, die mir zum jetzigen Zeitpunkt noch nicht bekannt sind.

Besonderen Dank gilt Herrn Dr. Kenichi Ataka, der durch seine spektroskopische Expertise ein ganz wesentlicher Mitbetreuer meiner Arbeit war und von dessen langjähriger Erfahrung ich profitieren durfte. Diesbezüglich und auch freundschaftlich möchte ich hier Frau Dr. Silke Kerruth hervorheben, der ich sowohl auf fachlicher, freundschaftlicher und für unzählige andere Dinge nicht weiß wie ich danken kann. Silke, dich behalt ich!

Weiterhin möchte ich auch Herrn Prof. Joachim Heberle für seine Unterstützung, Rat und Tat danken. Für Rat, Tat und entspannte und lustige Zusammenarbeit möchte ich Moritz Sängler, Hendrik Mohrmann, Sven Stripp, David Ehrenberg, Emanuel Pfitzer, Franziska Sellnau, Fucsia Crea und Matia Saita danken. Besonders möchte ich Dr. Nils Krause danken fürs Helfen, Essengehen und seine Freundschaft. Dank auch an Maria Walter für Zusammenarbeit, Unterstützung und die vielen, vielen kleinen Dinge. Frau Dorothea Heinrich und Kirsten Hoffmann möchte ich ebenfalls für die exzellente Zusammenarbeit danken. Die Gruppen von Ramona und Joachim möchte ich fachlich und menschlich besonders hervorheben und auch wenn ich nicht alle hier nennen kann, möchte ich jedes einzelne Mitglied auf diese Weise bedenken und meinen Dank aussprechen. Ich bin froh, dass ich schlussendlich bei euch ge-

landet bin. Zudem möchte ich auf diesem Wege Soraya Taabache hervorheben, die ich zwischen meiner Zeit in Jülich und in Ramonas Gruppe kennenlernen durfte.

Obwohl sich die Jahre in Jülich speziell gestalteten, durfte ich in dieser Zeit dennoch wertvolle Freundschaften schließen. Vielen Dank Daryan Kempe, Tina Züchner und Ramona Choy. Ich bin froh das ihr da wart und auch immer noch seid.

Neben den vielen lieben bereits genannten Menschen aus meinem Arbeits- und auch Freundschaftsumfeld, möchte ich nun den Menschen aus meinem anderen Leben danken. Zunächst möchte ich meinen Eltern für die unbeschreibliche Unterstützung danken, nicht nur während der letzten Jahre sondern überhaupt immer. Ohne euch wäre ich nicht hier. Ich danke meinen Brüdern und deren Familien, meiner Tante Luise und meiner Cousine Alexandra.

Ganz besonderen Dank möchte ich Denise Reichel und Ulrike Klöß aussprechen, die nicht nur langjährige sehr gute Freunde sind, sondern mich auch während der langen Zeit meiner gesundheitlichen Probleme extrem unterstützt haben. Bzgl. des letzteren möchte ich Herrn Dr. Kausch und Herrn Dr. Burkard-Meier nennen, dank derer ich unter anderen diese Zeit hintermich bringen konnte. Aber auch andere Freundschaften haben sich diesbzgl. während der letzten Jahre als ganz besonders erwiesen. Danke, dass es euch gibt: Hartmut Zech und Jürgen Werry, Katarina Moos und Michael Mainz.

Mit der Hoffnung, ich habe niemanden vergessen, danke ich, last but not least, der Kaffeemaschine.

Contents

List of Abbreviations	iv
1 Introduction	1
1.1 The “protein folding problem”	1
1.2 Membrane proteins and folding	4
1.2.1 Membrane proteins	4
1.2.2 Lipid bilayer milieu and effect on protein stability	5
1.2.3 Bacteriorhodopsin (bR) and other microbial rhodopsins	6
1.2.4 Folding of polytopic transmembrane proteins	8
1.3 Motivation and experimental concept	11
2 Theoretical Background	14
2.1 Nanodiscs	14
2.2 Cell-free protein expression	16
2.3 Infrared (IR) spectroscopy	17
2.3.1 Molecular vibrations and IR spectroscopy on proteins	18
2.3.2 Dispersive and Fourier transform infrared (FTIR) absorption spectroscopy	25
2.3.3 IR difference absorption spectroscopy	28
2.3.4 Surface-enhanced infrared absorption spectroscopy (SEIRAS)	28
3 Materials	34
4 Methods	42
4.1 Standard methods	42
4.1.1 Preparation and transformation of competent <i>E.coli</i> cells	42
4.1.2 SDS-PAGE	43
4.1.3 Agarose Gel Electrophoresis	43
4.1.4 Sequencing	44
4.2 Protein constructs for protein expression	44
4.2.1 Bacteriorhodopsin (bR) and bR variants	44
4.2.2 Other α -helical membrane proteins	46
4.2.3 Emerald green fluorescent protein (EmGFP)	47
4.3 Nanodiscs	47
4.3.1 Commercial nanodiscs	47
4.3.2 Membrane scaffold protein MSP1D1 and nanodisc assembly	47
4.4 Cell-free protein expression	49

CONTENTS

4.4.1	MembraneMax TM HN protein expression kit	50
4.4.2	PURExpress [®] In Vitro Protein Synthesis kit E6800S	51
4.4.3	Expression of bR into commercial nanodiscs	51
4.4.4	Expression of bR into MSP1D1/DMPC nanodiscs	53
4.4.5	Expression of other microbial rhodopsins into nanodiscs	54
4.5	SEIRAS experiments on membrane protein folding <i>in situ</i>	54
4.5.1	Instrumentation	54
4.5.2	Surface preparation	55
4.5.2.1	Ni-NTA SAM to immobilize nanodiscs to the SEIRAS prism	55
4.5.2.2	Nanodisc immobilization	57
4.5.3	Expression and folding of bR	58
4.5.4	Probing the functionality of bR in the SEIRAS folding experiment	59
4.5.5	BR folding experiment without immobilized nanodiscs	64
4.5.6	Impact of the co-factor retinal on the bR folding process	64
4.5.7	Cell-free expression of emerald green fluorescent protein (EmGFP)	64
4.5.8	Initial experiments on folding of other microbial rhodopsins	65
4.5.9	SEIRA spectra processing	65
5	Results and Discussion	67
5.1	Cell-free bR expression into nanodiscs	67
5.1.1	Commercial nanodiscs	67
5.1.2	Nanodisc assembled by MSP1D1 and DMPC	70
5.2	Cell-free expression of other microbial rhodopsins into nanodiscs	75
5.3	SEIRAS experiments on membrane protein folding <i>in situ</i>	76
5.3.1	Spectral examination of the Ni-NTA SAM surface preparation	76
5.3.2	Nanodisc immobilization to the Ni-NTA SAM	77
5.3.3	Folding of bR	85
5.3.4	Functionality of bR in the SEIRAS folding experiment	100
5.3.5	Impact of the co-factor retinal on the bR folding process	105
5.3.6	Cell-free expression of EmGFP	108
5.3.7	Folding of other microbial rhodopsins	109
6	Conclusion and Outlook	114
7	Summary	120
8	Zusammenfassung	121
	Bibliography	123
	List of publications	139
A	Supplementary IR spectra	140

B Plasmids and protein constructs	142
--	------------

List of Abbreviations

aa	amino acid
AFM	atomic force microscopy
Al₂O₃	aluminum oxide
ANTA	N α ,N α -bis(carboxymethyl)-L-lysine
Apo-AI	apolipoprotein A-I
ATP	adenosine-5'-triphosphate
ATR	attenuated total reflection
p.a.	pro analysi
APS	ammonium persulfate
BO	bacterioopsin
bop	bacterioopsin
bR	bacteriorhodopsin
CFU	colony forming unit
ChR2	channelrhodopsin 2
Chop2	channelopsin 2
CV	column volume
CFCF	continuous-flow cell-free
CECF	continuous-exchange cell-free
cryo-TEM	cryogenic transmission electron microscopy
Cr	<i>Chlamydomonas reinhardtii</i>
DMPC	1,2-dimyristoyl- <i>sn</i> -glycero-3-phosphocholine
DMSO	dimethylsulfoxid
DNA	deoxyribonucleic acid
dNTP	deoxynucleotide triphosphate
DPC	n-dodecylphosphocholine
DTSP	3',3'-Dithio-bis(N-succinimidylpropionate)
DTT	dithiothreitol
EDTA	ethylenediaminetetraacetic acid
E-field	electric field
EM	electromagnetic
EMT	effective medium theory

LIST OF ABBREVIATIONS

EmGFP	emerald green fluorescent protein
FTIR	Fourier transform infrared
GPCR	G-protein coupled receptor
HCl	acidic acid
H₂O	water
H₂O₂	hydrogen peroxide
H₂SO₄	sulfuric acid
HF	hydrofluoric acid
HeNe	helium neon
HDL	high density lipoprotein
HgCdTe	mercury cadmium telluride
Hs	<i>Halobacterium salinarum</i>
H. salinarum	Halobacterium salinarum
H. halobium	Halobacterium halobium
6xHis-tag	hexahistidine-tag
7xHis-tag	heptahistidine-tag
10xHis-tag	decahistidine-tag
IMAC	immobilized metal affinity chromatography
IPTG	isopropyl- β -D-thiogalactopyranoside
IR	infrared
Kan	kanamycin
LED	light-emitting diode
mRNA	messenger ribonucleic acid
MCT	mercury cadmium telluride
MWCO	molecular weight cut-off
MIR	mid-infrared
MSP	membrane scaffold protein
MCS	multiple cloning site
Na₂SO₃	sodium sulfite
NaAuCl₄	sodium tetrachloroaurate(III) dihydrate
Na₂S₂O₃	sodium thiosulfate
Nd:YAG	neodymium-doped yttrium aluminum garnet
NH₄F	ammonium fluoride
NH₄Cl	ammonium chloride
Ni-NTA	nickel nitrilotriacetic acid
NIR	near infrared
NMWL	nominal molecular weight limit
NTA	nitrilotriacetic acid

LIST OF ABBREVIATIONS

PBS	phosphate buffered saline
PCR	polymerase chain reaction
PURE	protein synthesis using recombinant elements
OD	optical density
ORF	open reading frame
RAIRS	reflection absorption infrared spectroscopy
RNA	ribonucleic acid
SAM	self-assembled monolayer
SDS-PAGE	sodium dodecyl sulfate polyacrylamide gel electrophoresis
SDS	sodium dodecyl sulfate
SEC	size exclusion chromatography
SEM	scanning electron microscopy
SEIRA	surface-enhanced infrared absorption
SEIRAS	surface-enhanced infrared absorption spectroscopy
SERS	surface-enhanced Raman scattering
Si	silicon
SLB	solid supported bilayer
SMFS	single molecule force spectroscopy
S/N	signal/noise
SRI	sensory rhodopsin I
SopI	sensory opsin I
SRII	sensory rhodopsin II
SopII	sensory opsin II
SRP	single recognition particle
TDC	transition dipole coupling
TDM	transition dipole moment
tRNA	transfer ribonucleic acid
tmRNA	transfer-messenger ribonucleic acid
TSP	thio-(N-succinimidylpropionate)
TEMED	N,N,N',N'-Tetramethylethylenediamine
UV	ultra violet
wt	wild type
Xe arc	xenon arc

Chapter 1

Introduction

Along with carbohydrates and lipids, proteins are a major molecule class within cellular systems and assemble a multitude of tasks as well as participate in many biochemical mechanisms and reaction cascades. In order to obtain correct function, a protein has to fold correctly from the nascent polypeptide chain into its final 3D structure [1]. Consequently, the folding of a protein ultimately affects biological health *vs.* disease [2]. Therefore, it is indispensable to understand the biophysical and biochemical principles of such folding processes.

1.1 The “protein folding problem”

The idea of the existence of defined structure elements within a protein and consequently a specific folding process, was supported by the advent of structural biology, initiated by the work of John Kendrew and Max Perutz, who published the first X-Ray structures of myoglobin and hemoglobin, respectively [3]. Supported by experimental evidence, Anfinsen and colleagues postulated, that thermodynamic interactions encoded in the amino acid sequence of the protein, are responsible for its stabilization and thus, the folding towards its final native state with global minimum Gibbs free energy under its specific environmental conditions [4, 5]. This postulate was later known as “thermodynamic hypothesis” of protein folding [6]. Therein, it does not matter from which conformational state folding starts, solely thermodynamic interactions are helping the protein through the conformational space towards its global minimum, pathway-independent [5, 7, 8]. This principle was later referred to as thermodynamic control of protein folding [7]. In 1969, Levinthal questioned this hypothesis (known as Levinthal paradox). He argued, that the time of finding the conformation with minimum free energy by random search and assuming all possible starting conformations of a linear polypeptide strand, would take years, which is inconsistent to the natural process of protein biosyn-

1. Introduction

thesis, where the protein reaches the native state within milliseconds or faster. Levinthal concluded a pre-determined pathway through possible intermediate states necessary for correct folding in order to fold fast enough, analogous to reaction coordinates in known biochemical reactions [9–11]. This implied a principle, mechanism or code by which the protein can determine the path through the huge conformational space. Conversely, this means, just a certain starting point results in the right native state. In other words, starting at a wrong conformational state can lead to a pathway where the protein gets trapped within an intermediate state, or where the protein ends up in a miss-folded state or where the protein has to travel along a route which takes longer than the optimal one. Thus, there are a multitude of final states, of which just one is the native one. Consequently, it is not required, that the native state is at a global thermodynamic minimum, instead it can also be a local minimum, which is in other words, the optimal thermodynamic state under the given environmental conditions. These considerations were designated as kinetic control of the folding reaction [7, 8].

The unleashed debate on folding principles raised three fundamental questions, which historically built the center of the protein folding problem:

“The physical folding code: How is the 3D native structure of a protein determined by the physicochemical properties that are encoded in its 1D amino-acid sequence?”

“The folding mechanism: A polypeptide chain has an almost unfathomable number of possible conformations. How can proteins fold so fast?”

“Predicting protein structures using computers: Can we devise a computer algorithm to predict a protein’s native structure from its amino acid sequence?” [3]

By assuming kinetic control of protein folding, it was first tried to identify folding pathways experimentally with the general goal to deduce fundamental folding principles to decrypt the unknown underlying selection rule by which the protein finds the right folding track towards the native state [8]. First phenomenological folding models derived from such experiments are the on-pathway, off-pathway and the sequential model (i.e. containing intermediate states), what Baldwin described as classical view [8].

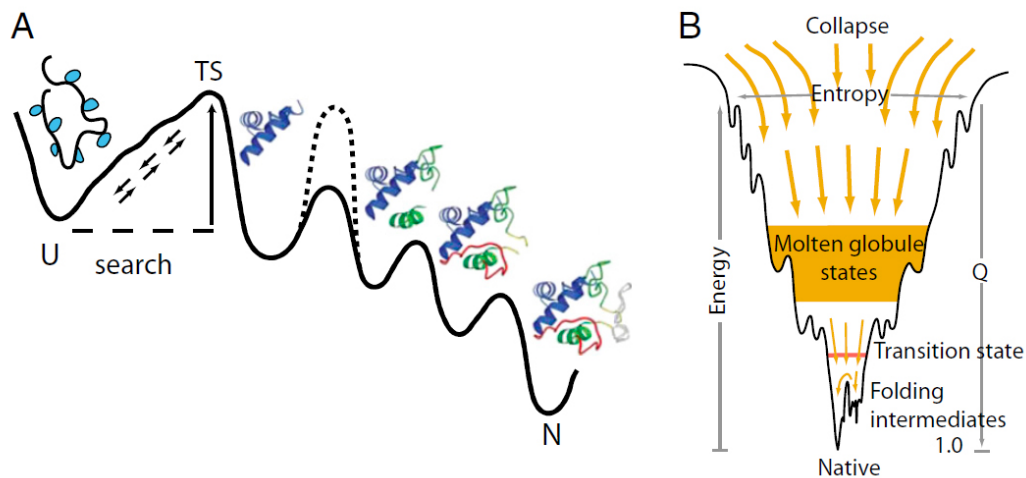


Figure 1.1: Classical *vs.* new view of protein folding. (A) The classical view as defined folding pathway. The dashed line is intended to illustrate a kinetic barrier. U is the unfolded state, TS a transition state and N the native state. (B) New view as multi-track folding along a funneled energy landscape. The figure was extracted from [2].

By combining experimental results and the advances in theoretical modeling, new models of folding were established, which Baldwin called the new view of folding [8, 12]. Fundamental models, on the basis of thermodynamic processes, which occur in a biological realistic time scale and could be linked to experimental data, are briefly described in the following. The sequential, framework or hierarchic model starts out from the formation of secondary structures by local interactions within the polypeptide chain. Then random diffusion collision leads to the formation of higher ordered structures. The diffusion collision model defines the protein as an amalgamation of several unstable quasiparticles called microdomains. These microdomains can assemble very quickly by random search. After formation, they form increasingly stable coalescences by diffusion collision until the final native state is formed. A further model is the hydrophobic collapse model. It is based on the idea, that the folding of the amino acid sequence is determined by interactions between hydrophobic side chains. The sequestration from the hydrophilic environment leads to a sudden hydrophobic collapse of the polypeptide chain, leading to a collapsed intermediate state (called molten globule), which is partially folded. Further hydrophobic contacts lead to folding around this molten globule until the final state. The last model mentioned here, is the nucleation condensation model, which compares folding to the chemical process of crystallization,

1. Introduction

i.e. the collapse around a diffuse nucleus [12, 13]. These concepts support the idea of thermodynamic control of the folding process, i.e. that folding is a stochastic process and that folding events are driven by the thermodynamics of the polypeptide chain, which can be described by a funnel shaped energy landscape [8, 12, 14]. Hence, this new view of protein folding represents the first step towards the replacement of the concept of distinct sequential intermediates with an energy funnel concept, energy landscapes and parallel events (see Fig. 1.1) [2, 8]. In that context, existing experimental and theoretical results can be described by various energy landscape shapes. Thereby, the conformational space is spanned by an x - and y -axis. The z -axis represents the internal free energy of a certain chain conformation, i.e. for example the sum of hydrogen bonds, ion-pairs, torsion angle energies, hydrophobic and solvation free energies [8].

1.2 Membrane proteins and folding

1.2.1 Membrane proteins

In biological systems, membrane proteins serve for cell signaling, cell adhesion, ion conductivity and build interfaces with e.g. cell wall and cytoskeleton [1]. They are naturally embedded in biological membranes, which mainly consist of glycerolipids, phospholipids, sterols, proteins, carbohydrates as well as glycolipids and glycoproteins. They build the physical barrier between the cell in- and exterior as well as enable compartmentalization within the cell (membranes of cell organelles). It can be distinguished between proteins not passing the membrane (peripheral proteins), passing the membrane (integral or intrinsic or transmembrane proteins) and as a special case polypeptide toxins [15]. Integral membrane proteins can be structurally differentiated by the number of segments spanning through the membrane and by their orientation relative to the membrane (Fig. 1.2 A). Among transmembrane proteins, the most abundant structure elements are the single-pass α -helix, the α -helical bundle and the β -barrel (Fig. 1.2 B) [1, 16, 17].

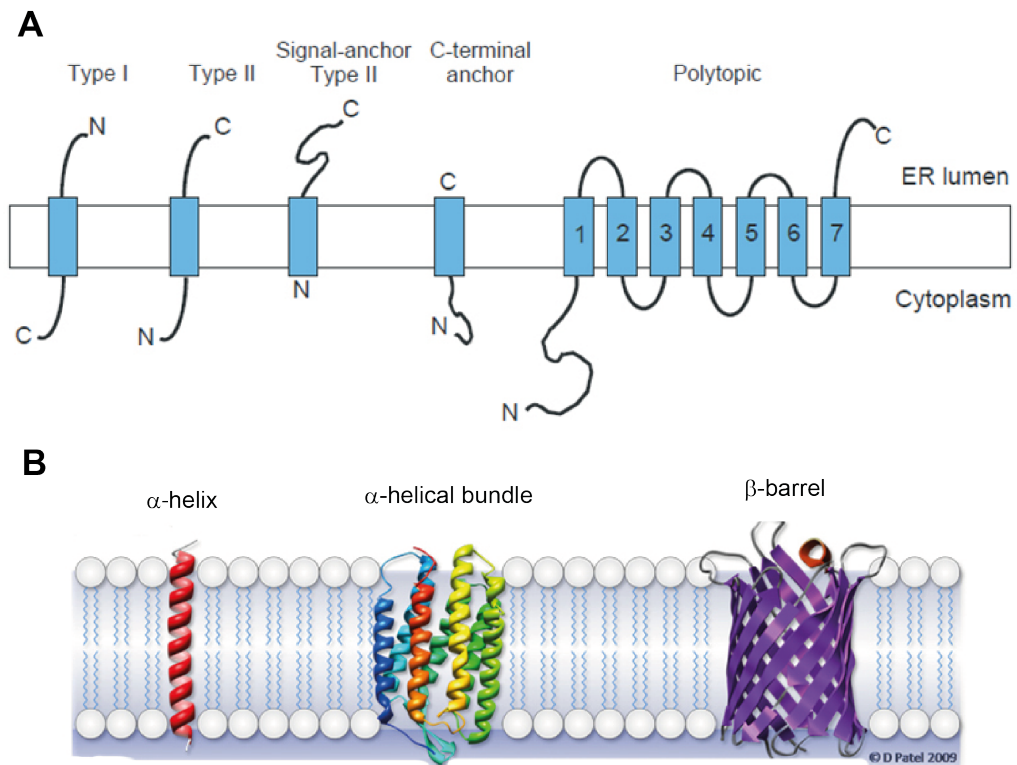


Figure 1.2: Classification of membrane proteins. (A) Subcategories of integral membrane proteins. Figure extracted from [18]. (B) Classification by their overall structure. Figure extracted from [17]. Depicted are a single α -helix, the α -helical bundle and the β -barrel.

Major functional classes of membrane proteins are active and passive transporters, receptors, enzymes as well as anchors and proteins serving adhesion [1]. To guarantee functionality, they have to remain stable in their given environment. Therefore, apart from the hydrophilic milieu of the lipid bilayer exterior, they have additionally to face the physical and chemical characteristics of the bilayer interior [19–22].

1.2.2 Lipid bilayer milieu and effect on protein stability

To understand the stability and dynamics (e.g. folding process) of a membrane protein within a lipid bilayer environment, a comprehensive knowledge about the chemical and physical characteristics of the protein and the lipid bilayer themselves as well as their interactions and consequential properties is mandatory. In the literature, such properties are described on an atomistic level towards global characteristics of molecular assemblies [19,20]. An idea of inter- and intramolecular interactions is given by figure 1.3. The composition of the lipid bilayer strongly influences these interactions. Here, a distinction is made between annular lipids (i.e. solvent lipids or boundary lipids), non-

1. Introduction

annular lipids (i.e. co-factor lipids bound within proteins or at protein–protein interfaces) and bulk lipids (i.e. not in contact with the membrane protein) [19].

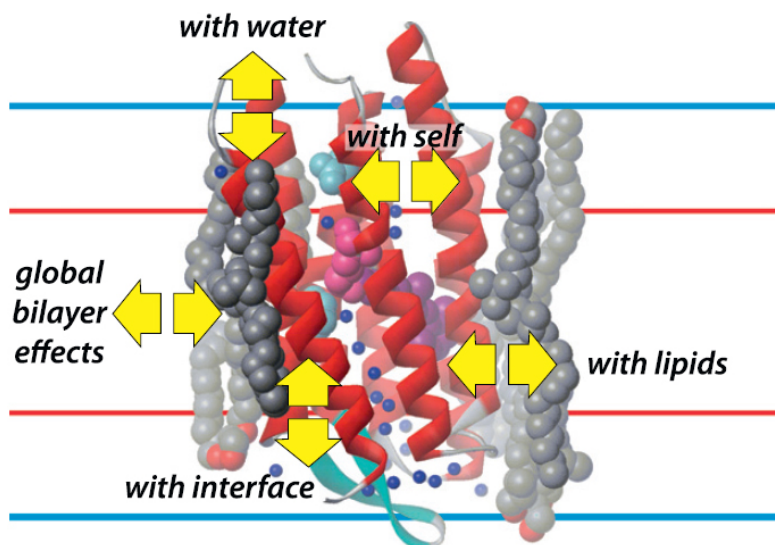


Figure 1.3: Illustration of interactions in a lipid bilayer containing a transmembrane protein by Cymer *et al.*, extracted from [21].

The chemical structure of a lipid, i.e. its fatty acid alkyl chain and especially the lipid head group, determines its chemical characteristics (e.g. hydrogen bonding, hydrophobic effects, charge interactions, van der Waals contacts) and physical parameters (e.g. the space occupied by the lipid, dimensions of its reactive regions). Consequently, the more complex a composition of a lipid bilayer is the more diverse are its properties, which can impact an integrated membrane protein. Hence, the lipid composition can influence the incorporation and folding of a membrane protein [19, 20].

The properties and stability of a lipid bilayer are predominantly determined by the balance of hydrophobic effects as well as inter- and intramolecular charge interactions [19]. Physicochemical properties of a lipid bilayer, which can effect protein stability and dynamics, are for example the charge interactions of its head group region, its hydrophobic thickness, its gel to liquid crystalline phase transition, its viscosity, its interfacial tension and elastic strain [19].

1.2.3 Bacteriorhodopsin (bR) and other microbial rhodopsins

In this thesis, predominately bacteriorhodopsin (bR) was employed to study folding of transmembrane proteins. It is a 7- α -helical transmembrane proton pump from the halophilic archaeon *Halobacterium salinarum*. The chromophore all-*trans*-retinal is bound to lysin 216 forming a Schiff base [23, 24].

A structure of bR with its bound chromophore retinal is shown in figure 1.4.

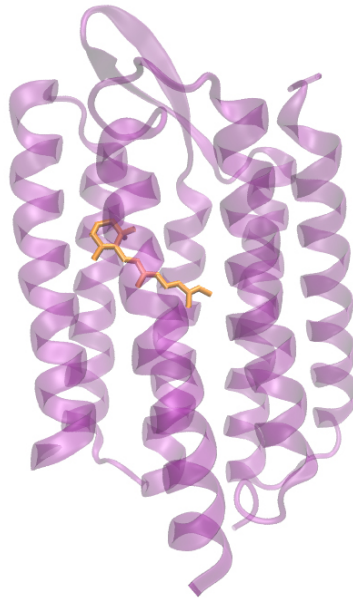


Figure 1.4: Structure of monomeric bacteriorhodopsin (purple) from *Halobacterium salinarum* and its co-factor retinal (orange). Reconstituted from the protein data bank RCSB PDB ID 5A45 [25] using the software VMD1.9.1.

Successfully folded and thus functional bR undergoes a unique photo-induced photocycle [26]. Under illumination the chromophore all-*trans*-retinal undergoes all-*trans* to 13-*cis*-isomerization leading to a deprotonation/ protonation reaction cascade between the chromophore and acidic amino acid side chains of bR cycling between different intermediate states of the photocycle, which absorb light at characteristic wavelength (Fig. 1.5). The photocycle leads to a proton gradient through the lipid bilayer transporting protons towards the extracellular space [23, 24, 27]. The proton gradient is then used by an adenosine-5'-triphosphate (ATP) synthase to create ATP, which serves as chemical energy storage [28].

Because of its internally bound co-factor, functional wild-type bR absorbs visible light at approximately 560 nm and hence appears purple. Within the membrane of *H. salinarum* bR assembles trimers, which in turn are closely packed in a two dimensional hexagonal lattice. This property gives the membrane of *H. salinarum* a representative purple color [23]. Since decades bR's structure and function had been studied extensively, which makes it to one of the most well analyzed membrane proteins [28, 33]. It is remarkably stable and easy to prepare by homologous or cell-free protein expression [22, 23]. Because of its structural and functional similarities with other transmembrane pro-

1. Introduction

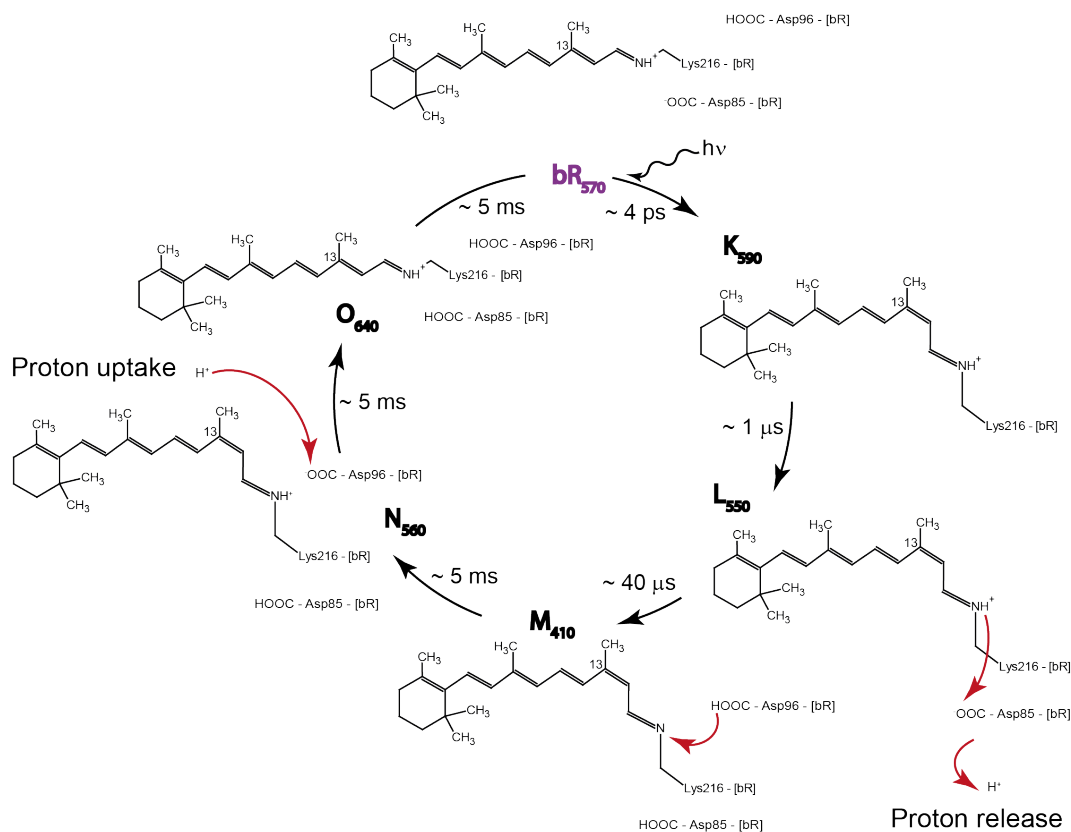


Figure 1.5: Photocycle of bR. The cycle was drawn in correspondence to [24, 29–31]. The respective life times for bR in 25 mM Na/KPi, pH 5.6, 1.5 % (w/v) anagrade n-Octyl- β -D-Glucopyranoside at room temperature were drawn next to the black arrows [24, 32].

teins, it serves as prototype within a multitude of research areas. Such topics comprise for example the functional understanding of retinal proteins and G-protein coupled receptors (GPCRs), which are key players in the animal visual process or the propagation of the action potential of neurons. Other trends address the energy conversion as alternative energy source and the potential as optogenetic tool [33, 34].

Additionally to bR, three other membrane proteins were employed in this thesis, sensory rhodopsin I (SRI), sensory rhodopsin II (SRII) and the transmembrane region of channelrhodopsin 2 (ChR2). All of them are structurally similar to bR and covalently bind the co-factor retinal. For more detail see the reviews [35–38].

1.2.4 Folding of polytopic transmembrane proteins

In the context of the protein folding problem (section 1.1), questions regarding essential factors, principles and pathways, that determine the transition, insertion and folding of a membrane protein, have been occupying experimentalists

and theoreticians for over 35 years [21,22]. *In vivo*, a membrane protein has to travel from the starting point of its biosynthesis, the ribosome, towards its final destination, the membrane, without aggregation due to the interactions of its distinctive hydrophobic regions with the aqueous environment. Thereafter, for the majority of polytopic transmembrane proteins, the insertion into the membrane proceeds co-translationally mediated by a protein-conducting channel, a translocon [16, 22]. During that passage the protein can fold at different stages of the transition/integration process, already within the ribosomal tunnel, at its exit moiety, within the translocon, during membrane insertion and within the membrane. All these different surrounding conditions can influence the folding route in a particular manner. Convergent, inherent interactions of the amino acid (aa) sequence and especially interactions between secondary structure elements, e.g. helix-helix contacts, affect the folding process significantly [20, 21].

Most polytopic transmembrane proteins are α -helical and β -barrel proteins (Fig. 1.2) [16]. Among them, α -helical transmembrane regions are the majority [16, 22]. In eucaryotes, typically, after protein translation has been started, a single recognition particle (SRP) binds to the N-terminus of the nascent polypeptide chain, which puts the protein synthesis on hold. When docking to the translocon, the SRP is released and the synthesis continues as an directional process including orientation and lateral release of the transmembrane regions into the lipid bilayer [22]. In procaryotes, the insertion into the membrane proceeds similarly [22]. However, here also post-translational pathways are known, at which the protein is fully synthesized and stabilized by chaperones before docking and integration into the membrane [22]. At this point, an important exception shall be noted. Several animal toxins can autonomously integrate and fold into a membrane without the help of any assisting molecules [20]. The pathway of β -barrel outer membrane proteins found in Gram-negative bacteria represents another fundamental mechanism of transition, integration and folding. After synthesis in the cytosol, the protein is passed through the inner membrane by a translocon. Subsequently it is stabilized by chaperones and guided to the Bam complex, a multiprotein machinery anchored in the outer membrane of the bacterium, which catalyzes the insertion process [22, 39, 40]. But still, many details of these transition, translocation and insertion mechanisms, hence the accompanied folding process, remain unclear, not least, because they are difficult to analyze experimentally [21].

1. Introduction

For polytopic α -helical transmembrane proteins, establishing a complete and general folding model *in vivo* based on experimental data could not be achieved so far [21]. Nevertheless, in order to understand the constraints of membrane protein formation, interactions of structural units like α -helices with each other and with the lipid bilayer were considered [20, 21]. Experimentally, such thermodynamic pathways are partially accessible *in vitro* and rely on the assumption that folding is an equilibrium-thermodynamical process [21]. A prominent example is the four-step model (Fig. 1.6), which combines the three-step-model of Jacobs and White [41] and the two-stage model of Popot and Engelman [42]. It describes the energetics of partitioning, folding, insertion and association of an α -helix at and within a lipid bilayer [21].

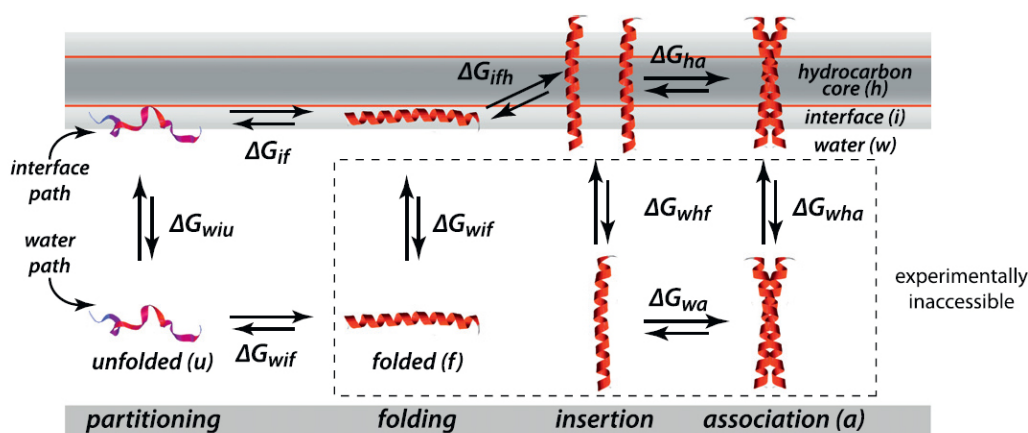


Figure 1.6: Four-step model to describe partitioning, folding, insertion, and association of an α -helix (red) in context of a lipid bilayer. ΔG is the Gibbs free energy, w indicates water, i, interface, h, hydrocarbon core, u, unfolded, f, folded and a, association. Extracted from [21].

Most what we know about folding of polytopic α -helical transmembrane proteins at present derived from studies on bR [22], starting with the work of Khorana and co-workers [43]. BR was found to assemble highly stable α -helical structures. Denaturation/renaturation experiments showed, that bR could hardly be denatured even by sodium dodecyl sulfate (SDS) [22]. Only by denaturing using organic solvents with subsequent transfer into SDS bR could be completely denatured [22]. Despite this harsh treatment, bR could be refolded and even bound its co-factor retinal again, resulting in its fully functional state, structurally identical to the wild-type protein [22]. Even when cut into two segments, bR could reassemble into its functional state [22]. Further experiments using separated α -helices led to the so called two-stage model of membrane protein folding by Popot and Engelman [42], which was

expanded to a three-stage model later on [44]. The authors separate the membrane protein folding pathway into two parts, the insertion process and the folding process, the latter at and in the lipid bilayer [16, 42]. The model is based on experiments with single bR α -helices, which were brought into contact to a lipid bilayer. They could show, that these single segments could autonomously integrate into the lipid bilayer, associate with each other and even re-bind the co-factor retinal. Three stages of folding were concluded: Stage one, the formation of separated α -helices within the membrane, stage two, the helix association, and stage three, partitioning of additional polypeptide regions (e.g. loops) or co-factor binding. This model had been confirmed many times [45]. Hunt *et al.* analyzed the reconstitution behavior of bR when all seven transmembrane helices were synthesized separately in advance and subsequently brought into contact with each other and lipid vesicles. They could show, that the first five helices associate spontaneously and form a stable structure. Contrary, helix F and G could form helices and associate only if the first five helices were established before. Unfolding studies on bR by single molecule force spectroscopy (SMFS) showed [46] consistent results.

Over the last decades predominantly unfolding/refolding studies repeatedly showed for a multitude of membrane proteins, that even in the absence of cellular factors (e.g. chaperones or translocons), a significant number of membrane proteins could regain their fully functional states [22]. This suggests, that membrane proteins, within the limitations of their thermodynamics as proposed for soluble proteins, adapt to the environment in which they were brought into rather than needing specific factors that dictate their folding [22, 47]. Hence, the final state of a membrane protein does not necessarily need to be the thermodynamic minimum, instead it could reside in an optimum state depending on the given environmental conditions [22]. In that context and in consideration of the crowded cellular milieu, helper molecules like chaperones or translocons seem more optimization than necessity [22]. Hence, on the basis of multiple possible folding pathways, the question arises if the folding process observed by unfolding/refolding studies really reflects the folding behavior during protein biosynthesis *in vivo* and thus shows the importance to study such processes under more native conditions.

1.3 Motivation and experimental concept

Usually membrane protein folding is studied by denaturing a functional protein and watching it when it folds back. Very often the protein does not unfold completely, instead it remains partially folded [20, 48–51]. In the case of bR, in

1. Introduction

most unfolding experiments by detergent treatment at least four helices remain folded [50]. So the refolding process starts from an undefined, not completely unfolded state [49]. This partially folded domains can alter the folding pathway [52]. Also, the refolding process starts from a full length amino acid sequence whereas the natural process starts from a growing polypeptide chain when the ribosome translates a genetic code into an amino acid sequence. Furthermore, the molecular environment of the folding scenario in a unfolding/refolding experiment is not comparable with the physiological conditions within a cell. Data from such experiments and the advances from simulations led to our today's understanding of protein folding. But the question remains, is protein folding *in vitro* different from folding of a nascent polypeptide chain during protein biosynthesis?

It is very difficult to watch live cell events like the folding process by spectroscopic techniques, because of the complexity of such systems. To circumvent these difficulties but stay close to natural processes, an *E. coli* based cell-free protein expression system shall be used, which drives transcription and translation. For membrane protein production, nanodiscs shall be supplemented, which mimic the cell membrane (Fig. 1.7 C). As a model protein, bacteriorhodopsin (bR), a 7- α -helical transmembrane proton pump from *Halobacterium salinarum*, shall be expressed, which is supposed to fold co-translationally synchronous with membrane insertion [53]. In comparison to a living cell, such a system in a reaction tube is accessible by spectroscopic techniques like UV/Vis spectroscopy.

Because of the advantage of infrared (IR) spectroscopy to access secondary structural information of a protein, membrane protein folding during protein biosynthesis is intended to be approached by surface-enhanced infrared absorption spectroscopy (SEIRAS). SEIRAS uses an Fourier transform infrared (FTIR) setup in attenuated total reflection (ATR) mode with a rough gold film covered silicon prism (Fig. 1.7 A and B). Conventional FTIR techniques would also monitor the huge number of other components in the cell-free expression system and the excess of water, which would overlay the signals of interest from the folding process. This is different for SEIRAS. When the IR beam gets totally reflected at the silicon/gold interphase, the excitation of surface plasmons generates an enhanced electromagnetic (EM) field in close proximity to the surface, which is approximately 10 nm towards the lumen of the sample chamber. This defined space allows selective measurements with monolayer resolution.

Consequently, a Ni-NTA layer shall be built up atop the gold film, by which nanodiscs are tethered via a histidine-tag. Thereafter, the components of the protein expression system shall be added onto the nanodisc monolayer. In the next step, the transcription and translation of bR shall be initialized by adding the DNA. The entire process shall be monitored by SEIRAS. Due to the intensity limitation of the enhanced electromagnetic (EM) field, processes in the bulk solution, i.e. in the cell-free expression system, remain invisible whereas processes occurring at the nanodisc monolayer are detectable. The experimental concept is shown in figure 1.7.

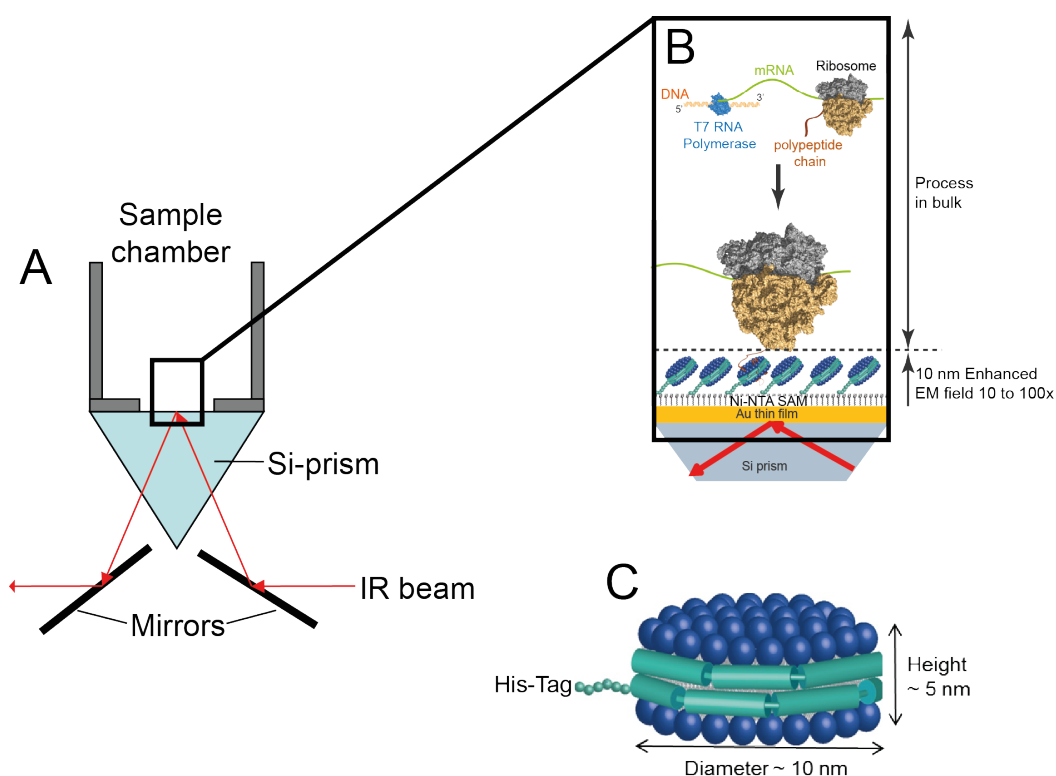


Figure 1.7: Experimental concept: (A) SEIRA sample chamber at the Si prism with totally reflected IR-beam; (B) Cutout of (A) during the experiment. Shown are the gold surface immobilized nanodiscs via Ni-NTA HIS-tag affinity binding. The cell-free expression system is placed atop the nanodisc monolayer. During the experiment, protein transcription and translation occur within this bulk phase, with ribosomes (brown) synthesizing the membrane proteins (here bR in pink) which can fold into the nanodiscs. The enhanced EM-field decays with approximately 10 nm distance from the gold surface; (C) Graphical illustration of a here used nanodisc.

Chapter 2

Theoretical Background

2.1 Nanodiscs

From the top view, nanodiscs are discoidal lipid bilayer patches wrapped by two α -helical membrane scaffold proteins (MSPs) in a belt like fashion (Fig. 2.1). The MSPs shield the hydrophobic region of the lipid bilayers from the aqueous environment [54–56].

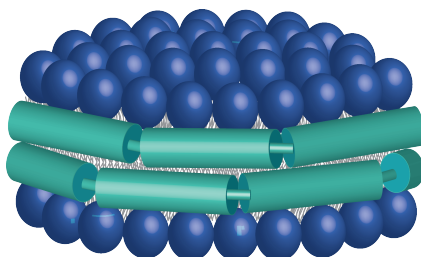


Figure 2.1: Schematic drawing of a nanodisc. The lipid head group region of the lipid bilayer is symbolized by blue spheres and the MSPs by the green cylinders. The figure was prepared using Adobe Illustrator CS5 according to [57].

These nanometer-scaled phospholipid bilayers were developed by Sligar and co-workers [55], based on studies on human high density lipoprotein (HDL). Human HDLs are a class of plasma lipoproteins, which are not covalently bound assemblies of phospholipids, cholesterol, cholesterol esters, triacylglycerides and predominately apolipoprotein A-I (Apo-AI) and -II. Physiologically, they are key devices in reverse cholesterol transport from tissue cells towards the liver. HDL fractions undergo various transformations by a self-assembly process: from a lipid poor aggregated state via a discoidal state towards a more spherical form [58].

Sligar *et al.* [55] modified the amino acid sequence of Apo-AI, so that it forms stable disc-like phospholipid bilayer patches as environment to recon-

stitute membrane proteins. They were able to express a protein construct by standard recombinant gene expression techniques in *E.coli*. When solubilized with detergents and addition of phospholipids, this protein construct, termed MSP, was able to self-assemble into discoidal phospholipid bilayers during detergent removal [55]. These membrane fragments were trademarked nanodiscs. The self-assembly process showed a remarkable precision in generation of nanodiscs with monodisperse size distribution, at which one nanodisc was enclosed by two MSPs. The first developed and tested MSP construct was MSP1 (Fig. 2.2) [54, 55] to generate nanodiscs with a diameter of 10 nm and 5.5 nm in height.

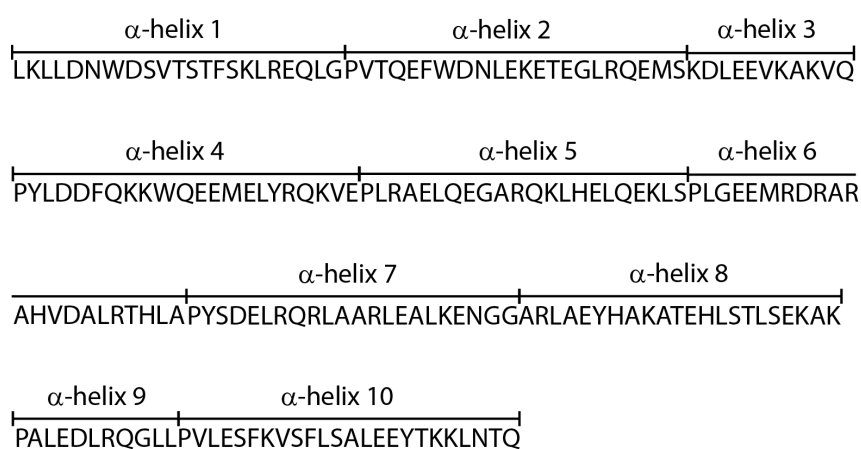


Figure 2.2: Amino acid sequence of MSP1. α -helices are indicated according to [59, 60]. The figure was prepared using Adobe Illustrator CS5.

Nanodiscs are water soluble and stable under physiological conditions. The membrane is accessible from both sides. Properties as diameter and thickness are tunable by the length of the MSPs amino acid sequence and the type of lipid used, respectively [54]. Furthermore, the used lipid or lipid composition determines the chemical nature of the membrane, e.g. charge, reactive groups, hydrophobicity, as well as physical characteristics like the rigidity of the membrane, which are important features for membrane protein structure, function and biogenesis [19].

However, the initial goal for Sligar *et al.* was the stable reconstitution of purified, recombinant membrane proteins into a native environment (i.e. phospholipids), which are functional and soluble in an aqueous phase. Therefore, the process of nanodisc assembly was extended by introducing a detergent solubilized membrane protein to the self-assembly process. The result were soluble, monodisperse, homogeneously reconstituted membrane proteins on satisfactory concentration ranges [55, 61]. This represented a methodolog-

2. Theoretical Background

ical breakthrough for structural and functional biochemistry and biophysics of membrane proteins, since they were now much better accessible to study. During the last decades nanodisc technology expanded rapidly, as did its application range [62].

2.2 Cell-free protein expression

In vitro protein expression systems provide the necessary transcription/translation machinery for a protein biosynthesis. Based on the pioneering work of Buchner, Nirenberg and Mathaei [63] cell-free protein expression systems became a powerful tool for high-throughput production of functional soluble and membrane proteins as well as diverse peptides. They are utilized in a wide interdisciplinary application range, e.g. in structural and functional proteomics, in diagnostics and therapeutics as well as protein evolution and engineering [64–67]. Cell-free protein expression represents a high-potential method and still develops exponentially with growing interest in various industrial sectors (e.g. biotechnology, personalized medicine and pharmaceuticals) [65,66].

Most of these systems are based on crude cell extracts, which are depleted of cell debris and exogenous deoxyribonucleic acid (DNA) and messenger ribonucleic acid (mRNA). The lysate is supplemented by energy components, e.g. ATP, free amino acids and template specific DNA polymerases. By addition of the protein encoding DNA, the protein expression is initiated and proceeds under the respective temperature and other conditions, e.g. stirring [63].

At present, a lot of different cell-free protein expression systems exist. They can be differentiated with respect to their configuration, their source of lysate as well as productivity and automation [64]. Historically, two configurations are defined. One is called uncoupled, which means that mRNA is added to the cell lysate, so that no transcriptional, just the translational part of the protein expression takes place. The other is the coupled or linked configuration [63,64], in which transcription as well as translation proceeds due to initiation by the template DNA. Over the past decades a multitude of different cell-free systems were developed based on crude cell lysates derived from different procaryotic and eucaryotic cell types [63]. Such systems are based on for example *E.coli*, yeast, wheat germ, rabbit reticulocyte or insect cell lysates [63,64]. Additionally, the Ueda lab [68] developed a system of recombinant, purified components expressed in *E.coli*, which they termed **protein synthesis using recombinant elements** (PURE). The compositions of these systems are completely defined whereas for systems based on crude cell extracts they are not. With regard to productivity and automation, different formats of cell-

free reactions are batch-fed formatted reactions, continuous-flow cell-free (CFCF), semi-continuous-exchange cell-free (CECF) and CECF as well as the bilayer based translation systems [64].

The open access to the cellular machinery in cell-free protein expression systems represents many advantages in comparison to the classical expression of proteins in host cells. Without physical barriers, e.g. the cell wall, modifications of the system by supplements, the removal of the product, system monitoring and rapid sampling can be easily accomplished [66]. Without the difficulties of heterologous or homologous protein expression and purification like the loss of product, protein aggregation, cell toxicity or inclusion bodies etc., can be circumvented. Hence, reaction volumes and process times can be reduced. Moreover, cell-free protein expression is supposed to favor increased proper folding and decreased aggregation of expressed proteins [67]. The challenge of low protein yields in comparison to cell based protein expression could be overcome during the last years by achieving yields in industrial scale [65, 66]. Nevertheless, not every system serves every purpose. With regard to the aim of application the right system has to be chosen, because, besides the mentioned general advantages, each system has its own advantages and disadvantages as well as degree of modifiability (see [63]). With the appropriate system, even traditionally challenging proteins can be faced as toxins or membrane proteins [64, 65]. Moreover, optimization can be accomplished by tunable post-translational modification. Even incorporation of unnatural amino acids, different kinds of labeling and other specific protein variants for biophysical investigations can be performed. Especially with the regard to membrane proteins, cell-free protein expression systems can be a powerful method. Over the past decades, the combination of bio-mimetic membrane systems with cell-free expression reactions led to the successful production of water stabilized, functional membrane proteins [69, 70]. Here, the combination of nanodiscs with cell-free protein expression systems shall be noted in particular. It represents a simple and highly efficient approach to insert membrane proteins by cell-free protein expression *in operandi* [71, 72].

2.3 Infrared (IR) spectroscopy

The term vibrational spectroscopy refers to two techniques: IR spectroscopy (= absorption of IR radiation) and Raman spectroscopy (= inelastic scattering of electromagnetic radiation, typically from ultra-violet to near infrared (NIR) [73]). After its discovery and first investigations on these effects in the late 19th and the early 20th century, methodological and technical possibilities grew

2. Theoretical Background

rapidly in the 1960s. Now, even complex biological molecules can be studied by these methodologies such as lipids, carbohydrates and proteins [74].

In protein research, vibrational spectroscopy is a strong tool for the identification and characterization of dynamic processes, for example intermediate states or diverse inter- and intramolecular interactions [74, 75]. Advantages for this work are for example: the independency of the physical state (i.e. solution, solid, crystal or monolayer), almost no sample size restriction, information about the conformational state of a protein and surrounding conditions of vibrating groups [74, 76].

2.3.1 Molecular vibrations and IR spectroscopy on proteins

Molecules can absorb IR radiation by their rotational and vibrational transition. The **simplest case** to describe the IR absorption of molecular vibrations is a diatomic molecule. Its vibration can be described by the harmonic oscillator. The possible system states and their associated energy eigenvalues can be calculated quantum mechanically by solving the time-independent Schrödinger equation for the one-dimensional harmonic oscillator [77, 78]:

$$\hat{H}\psi = -\frac{\hbar^2}{2\mu} \frac{d^2\psi}{dx^2} + \frac{1}{2}kx^2\psi = E\psi \quad (2.1)$$

with μ , the reduced mass for the relative motion of two point charges m_1 and m_2 by

$$\mu = \frac{m_1 m_2}{m_1 + m_2} \quad (2.2)$$

and \hat{H} , the Hamilton operator, ψ , the wave function, which describes the states by the associated energy eigenvalues E , k , the force constant, and x , the dimension in which the movement takes place (i.e. the distance of the atoms). Solving the equation yields the energy eigenvalues of the molecule's vibrational levels for the one-dimensional harmonic oscillator:

$$E_v = h\nu\left(v + \frac{1}{2}\right) = \hbar\omega\left(v + \frac{1}{2}\right) = \hbar\sqrt{\frac{k}{\mu}}\left(v + \frac{1}{2}\right) \quad (2.3)$$

$$v = 0, 1, 2, 3, \dots$$

with $\nu = \frac{\omega}{2\pi}$, $\hbar = \frac{h}{2\pi}$ and $\omega = \sqrt{\frac{k}{\mu}}$, where ν is the frequency, v is the vibrational quantum number, h , the Planck's constant and ω , the angular frequency. For the selection rule for vibrational transitions applies $\Delta v = \pm 1$.

This can be expressed in wavenumbers by

$$\frac{E_v}{hc} = \tilde{\nu}(v + \frac{1}{2}) = G(v) \quad (2.4)$$

with the harmonic vibrational wavenumber

$$\tilde{\nu} = \frac{1}{2\pi c} \sqrt{\frac{k}{\mu}} = \Delta G(v) \quad (2.5)$$

which represents the distance between the vibrational levels of the harmonic oscillator [77, 78].

This description using the potential function of an harmonic oscillator implies equidistant vibrational energy levels and an infinite number of possible excitations, which is unlikely as every molecule dissociates with respective excitation. Furthermore, the model of the harmonic oscillator results in negative distances of the atoms for high excited states. To describe this in-harmonic behavior, the Morse potential is applied, in which the potential energy function converges towards the atoms dissociation energy with decreasing distances of the energy levels (Fig. 2.3) [79].

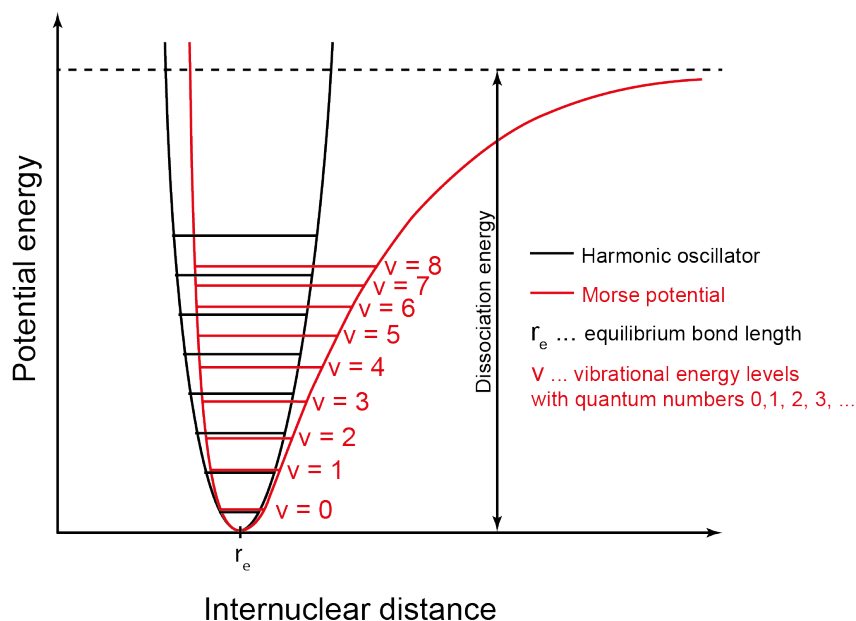


Figure 2.3: Schematic representation of the harmonic oscillator and Morse potential energy functions of a diatomic molecule. The figure was prepared using Adobe Illustrator CS5 analogously to [79].

Solving the Schrödinger equation for the in-harmonic oscillator using the Morse potential gives [77, 78]

2. Theoretical Background

$$E_v = \hbar\omega\left(v + \frac{1}{2}\right) - \frac{(\hbar\omega)^2}{4D}\left(v + \frac{1}{2}\right)^2 \quad (2.6)$$

or

$$G(v) = \left(v + \frac{1}{2}\right)\tilde{\nu} - \left(v + \frac{1}{2}\right)^2 \frac{\tilde{\nu}^2}{4D} \quad (2.7)$$

with D , the dissociation energy between the continuum boundary and the potential minimum. For the selection rule of vibrational transitions applies $\Delta v = \pm 1, \pm 2, \pm 3, \dots$. The distance between the energy levels is now described by

$$\Delta G(v) = \tilde{\nu} + 2\left(v + 1\right) \frac{\tilde{\nu}^2}{4D} \quad (2.8)$$

For multi-particle systems the model of the one-dimensional harmonic oscillator can be transferred to the N -dimensional harmonic oscillator. For the consideration of the multi-particle system, all three coordinates are considered in which an atomic nucleus can move. For all atoms of the system these are $3N$ degrees of freedom. Because of the complexity of such systems an analytical solution is not possible. Simplifications are indispensable, which deliver the result of the Schrödinger equation for the multi-dimensional problem:

$$E = \sum_i^{3N} \hbar\nu_i\left(v_i + \frac{1}{2}\right) \quad (2.9)$$

Consequential, an N -atomic molecule has $3N$ fundamental transition frequencies ν_i . Furthermore, every result of eq. 2.9 can be assigned to a coordinate Q , which is the linear combination of the former Cartesian coordinates x . Hence, the symmetry of the molecule has an impact on Q . Thus, every fundamental frequency can be assigned to a coordinate Q , which is termed a normal mode of the system. Therefore, the total number of normal modes of a molecule is $3N$, which is defined by its atoms N , three degree of motional freedom and its symmetry. All other movements are linear combinations of these normal modes. Vibrational normal modes (hereafter referred to as normal modes) are uncoupled and can be considered independent oscillators, where all participating vibrations (i.e. the former x coordinates) of one normal mode have the same frequency. The frequencies of the infrared radiation which correspond to the normal modes of the molecule can be absorbed [77, 78].

Subtracting the translational and rotational degrees of freedom, the number of vibrational **normal modes** is calculated as $3N - 6$ (for non-linear molecules)

or $3N - 5$ (for linear molecules), respectively. Basic molecular vibrations can be differentiated between [76]:

- vibrations changing distances between atoms known as valence or stretching vibrations ν , which can be symmetrically (s) or asymmetrically (as) to each other if more than two atoms are participating,
- vibrations changing angles between molecular groups known as deformation or bending vibrations δ , which can be:
 - in-plane (ip, i.e. vibration within the plane spanned by three or more atoms) or
 - out-of-plane (op, i.e. vibration of an atom out of a three or more atom spanned plane),
- and torsion vibrations τ (torsion of a σ -bond which connects two planes spanned by three or more atoms).

In **macromolecular systems**, frequencies of many vibrational modes and coupled modes shape the IR absorption signal. However, the absorption properties of certain molecular vibrations and their interactions with each other assist to conclude for example on the chemical structure and building blocks as well as dynamic processes of the molecule. For **proteins**, the IR spectra can be influenced by their protein backbone, their amino acid side chains, bound ligands and co-factors, hydrogen bonding, redox states etc. [76]. Thereby, the protein backbone is of particular importance for the secondary structure evaluation of a protein. The backbone is a sequence of peptide bonds, which are identical and, taken individually, essentially planar and thus geometrically fixed. A sequence of such rigid units produces repetitive structure elements, each containing the same fingerprint vibrations. Due to superposition of these fingerprint vibrations, demonstrative absorption bands in a certain spectral range can be observed: the **amide modes**. According to theoretical calculations a peptide bond has 12 normal mode vibrations, whereas six are significantly stronger than the others: amide A and B, amide I, amide II, amide III and skeletal stretches (see Tab.2.1) [76,80]. Amide modes are dominant in protein IR spectra, which shall be illustrated by the example of bR in purple membrane in figure 2.4.

2. Theoretical Background

Table 2.1: Representative amide modes of a peptide bond, adapted from [76,80].

Amide mode	Potential energy distribution (%)	Spectral region [cm ⁻¹]	
Amide A:	ν -NH (100)	~3310–3270	designated amide A, often part of Fermi resonance doublet, other component is amide B 3100–3030 cm ⁻¹ (resonance with overtone of amide II (α -helix) or amide II combination mode(β -sheet))
Amide I:	ν -CO (83), ν -CN (15), δ -CCN (11), ip δ -CN (<2)	~1650	hardly effected by amino acid side chains, rather by secondary structure of the backbone; commonly used for secondary structure analysis
Amide II:	ip δ -NH (49), ν -CN (33), ip δ -CO (12), ν -CC (10), ν -NC (9)	~1550	
Amide III:	ip δ -NH (52), ν -CC (18), ν -CN (14), ip δ -CO (11)	~1400–1200	significantly influenced by backbone and side chain vibrations
Skeletal Stretch:	ν -NC _{α} (77), ν -CC (17)	~1200	well defined but weak; expected to mix with side chain coordinates, resulting in complex modes ~1200–800 cm ⁻¹
	ν -CN (31), ν -CC (17), ν -CO (16), δ -CNC (14), δ -CCN (10)	~880	

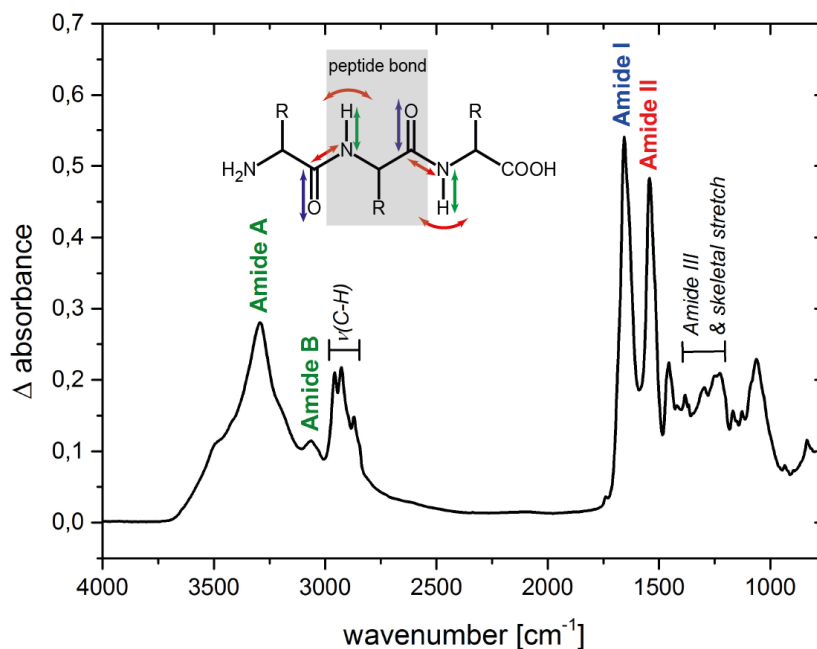


Figure 2.4: Exemplary assignment of the most representative amide modes in proteins by means of a background subtracted ATR-FTIR spectrum of bR in purple membrane, which was dried on a Si-ATR crystal (data by courtesy of Dr. Sven T. Stripp, FU Berlin, Germany). The chemical structure in the upper part illustrates the peptide bonds in the protein backbone with the amino acid side chains (R), and color coded arrows, representing the dominant vibrational motions of the amide modes described in table 2.1. Amide III and the skeletal stretch vibrations are hidden by the optical properties of the Si crystal. The C-H stretch vibrations $\nu(\text{C-H})$ are caused by the alkyl chains of the purple membranes polar lipids and amino acid side chains. The figure was prepared using Origin9.0 and Adobe Illustrator CS5.

In consequence to the rigid nature of a peptide bond, the primary structure of a protein is altered by changing the dihedral angles between the peptide bond plains. The resulting configuration (**secondary structure**) of the amino acid sequence further confines the spectral features of the amide modes, i.e. band shape and position. Basic secondary structure elements are the right-handed α -helix, the β -sheet, turn and random structures. To analyze the secondary structure, the most representative amide mode is **amide I**, as indicated in table 2.1, since amino acid side chain vibrations hardly alter the mode (thus the band) but secondary-structure configurations. Table 2.2 shows examples of the spectral ranges of the amide I band regarding these structures based on various data from the literature [76].

2. Theoretical Background

Table 2.2: Spectral ranges of amide I band position with regard to basic secondary structures, adapted from [76].

Secondary structure	Band position in $^1\text{H}_2\text{O}$ [cm^{-1}]	
	Average	Extremes
α -helix	1654	1648–1657
β -sheet	1633	1623–1641
β -sheet	1684	1674–1695
Turns	1672	1662–1686
Disordered	1654	1642–1657

Because of the multitude of vibrations and coupling effects in macromolecular systems such as proteins, amide modes superimpose and mask structural details. Possible coupling can occur with other normal modes, combination modes or over tones. The specific absorption properties of the amide mode vibrations for different configurations of the protein structure play a major role in **secondary structure analysis** from experimental data. Thereby, for example time-resolved measurements can give insights in folding reactions, folding changes or tertiary structure formation. To extract meaningful information from absorption patterns and interpret them with the help of theoretical or reference values, common data evaluation methods are used. Those are based on band narrowing and curve fitting and secondly, pattern recognition calculations by means of known spectra [76].

To understand which interactions shape the amide I mode and how (i.e. **structure-spectrum relationship**), theoretical models are utilized. Therefore, commonly considered intra-backbone effects are through-bond coupling, hydrogen-bonding, the dielectric constant of the environment and transition dipole coupling (TDC). **Through-bond coupling** and the **dielectric constant** of the environment play a minor role in the theoretical consideration. However, this is different for **hydrogen-bonding**. Its strength correlates with the maximum of the amide I signal. This allows a differentiation of certain secondary structures to some extent and conclusions of the solvation state of e.g. α -helices (i.e. helices in aqueous environment show slight differences in the amide I band compared to helices in a lipidic environment). Admittedly, **TDC** is the dominant effect that influences the shape of the amide I band (as well as the amide II and partially the amide III band). The TDC model describes the interaction between oscillating dipoles of neighboring amide groups, whereas the coupling depends on the relative orientation, the distance between

and the frequency of the dipoles. Coupling of oscillating dipoles and the symmetry of the backbone influence the polarization of the oscillators transition dipole moment (TDM). The dipole moment of the whole oscillating system is different than that of a single TDM. This leads to different transition energies resulting in a frequency shift of the absorbed energy. Furthermore, it allows one to make conclusions about allowed and forbidden transitions. With regard to infinite secondary structures, this concept has been proven to be the most simplest (evaluated according the perturbation theory by Miyazawa) and to be in good approximation to experimental data. Improved models contain various interactions like hydrogen-bonding, through-bond coupling or polypeptide size [76].

2.3.2 Dispersive and Fourier transform infrared (FTIR) absorption spectroscopy

In **dispersive IR absorption spectroscopy**, the absorbance of a sample within a respective wavelength range is probed at each wavelength. The absorption at a certain wavelength can be calculated by the Lambert-Beer's law when intensity losses due to other processes (e.g. scattering, diffraction or reflectance) are neglected:

$$A = E_{\lambda} = \lg\left(\frac{I_0}{I}\right) = \epsilon cd \quad (2.10)$$

with A, the absorption at wavelength λ , E_{λ} the decade extinction (or decade absorbance), I_0 , the intensity of the incident light, I, the intensity of the transmitted light, ϵ , the molar (decade) absorption coefficient, c, the concentration of the sample and d, the path length of the light beam through the sample [77].

Scanning the sample in that way is time consuming. Furthermore, the used optics decrease the signal to noise ratio. Thus, for low sample concentrations and for reactions faster than the scanning velocity the obtainable information is strongly reduced [81].

In **FTIR absorption spectroscopy** these features could be optimized, basically, by using the interferometer unit of the spectrometer. In the following, the interferometer principle is briefly explained by the classical Michelson interferometer geometry (Fig. 2.5).

2. Theoretical Background

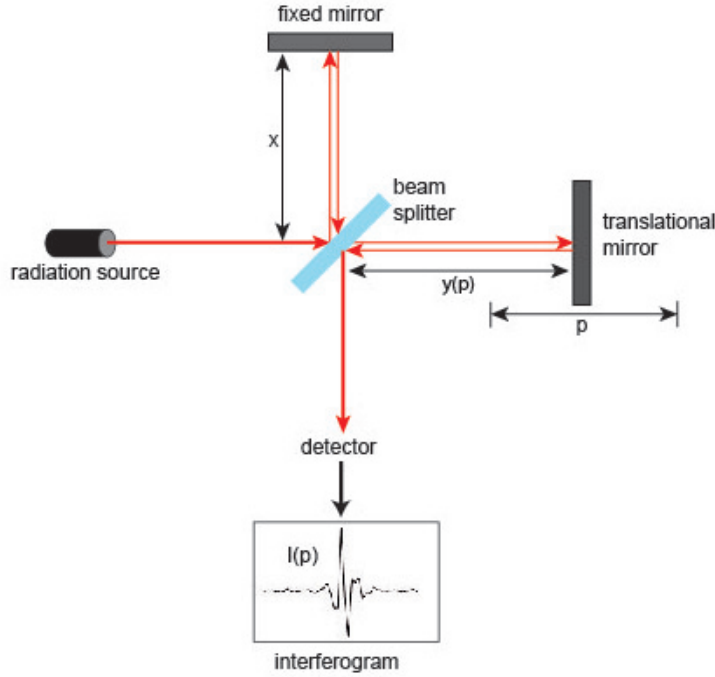


Figure 2.5: Geometry of a Michelson interferometer. The figure was prepared using Adobe Illustrator CS5.

An infrared beam is split by a beam splitter at which 50 % of the incoming beam is perpendicularly reflected towards a fixed mirror with distance x and 50 % of the incoming beam passes through the splitter towards a movable mirror with distance $y(p)$. After reflection at the mirrors the beams reunite at the same splitter and interfere with each other. Depending on the position of the movable mirror, the beam of the movable mirror is phase shifted with regard to the other beam, which leads to constructive or destructive interference, respectively. Hence, the measured intensity I of the reunited beam depends on the phase shift γ , which is equivalent to the mirror position p . If a polychromatic beam enters the interferometer as in the case of Globar radiation, the measured signal at the detector for a certain p is the superposition of all the beams spectral components. Moving the mirror once from p_{max} to p_{min} yields the total output intensity $I(p)$ of the interfering beams as function of the mirror position, which is described for the ideal case by [74, 81]

$$\frac{1}{2}I_0 + I(\gamma) = \frac{1}{2} \int_0^{\nu_{max}} S(\nu) d\nu + \frac{1}{2} \int_0^{\nu_{max}} S(\nu) \cos(2\pi\nu\gamma) d\nu \quad (2.11)$$

with the total integrated intensity I_0 of the IR beam which enters the interferometer and the spectral intensity $S(\nu)$ of a spectral component with

the frequency ν . The spectrum is limited by ν_{max} . $I(\gamma)$ changes as the mirror moves, hence, it represents the interferogram $I(p)$ and can be written as:

$$I(\gamma) = \frac{1}{4} \int_{-\infty}^{+\infty} S(\nu) e^{i2\pi\nu\gamma} d\nu \quad (2.12)$$

The intensity spectrum $S(\nu)$ can be obtained by inverse Fourier transformation:

$$S(\nu) = 4 \int_{-\infty}^{+\infty} I(\gamma) e^{-i2\pi\nu\gamma} d\gamma \quad (2.13)$$

The spectral resolution limit is defined by the maximum movement range of the mirror with

$$\Delta\tilde{\nu} = \frac{1}{2p_{max}} \quad (2.14)$$

The critical parameter is the mirror configuration. To guarantee interference and exact assignment of the mirror position to the output signal intensities, the exact localization and adjustment of the mirror has to be maintained during the entire measurement. To assure the latter, a laser is typically coupled parallel to the IR beam.

If the path difference between the mirrors is zero or an integer number of $\frac{\lambda_{Laser}}{2}$, the beams interfere constructively because the phase shift γ of the interfering beams is zero (called zero-crossing). By counting the zero-crossings of the lasers interferogram the mirror position can be determined. [81]

The following **advantages** arise from the described instrumental setup [74]:

- Multiplex- or Fellgett's advantage: The sample can be probed over an entire spectral region at the same time. Thus, measurements for faster reactions are possible. The speed to measure one spectral region is basically limited by the speed of the mirror movement. Thus, multiple scans for a short time interval are possible. Furthermore, the signal to noise (S/N) ratio is substantially increased as in the case of grating instruments. Averaging the spectra additionally increases the S/N ratio.
- Jacquinot's advantage: Reduction of optical losses by the use of large apertures when the beam enters the interferometer.
- Connes advantage: High absolute wave number accuracy and high resolution by applying the control laser.

2. Theoretical Background

2.3.3 IR difference absorption spectroscopy

Some differences of a state A to state B of a sample are hardly or not visible by just comparing their IR absorbance spectra. The same applies for changes due to molecular reaction mechanisms (usually changes in the order of 0.1 %), which can be chemical reactions, e.g. protonation/deprotonation, conformational or environmental changes, flexibility changes in structure or changing of the extinction coefficient. If changes are not directly visible from the absorption spectra, **difference spectra**, i.e. subtracting the absorbance of state B from A, can reveal insight to changes. The ideal difference spectrum shows exclusively changes between the states and strongly discriminates the background. Positive bands relate to state B and negative bands relate to state A. Since many reactions compose of a series of transient states, it is advisable to follow the reactions directly in the sample chamber starting from the stable state A. Resulting spectra are termed reaction-induced difference absorption spectra. This method enables the investigation of molecule-protein interactions, light-induced reactions, protein folding, redox reactions etc. It is sensitive to side-chain effects, diverse inter-/intramolecular effects and backbone changes. Hence, one may consider a difference absorption spectrum of a protein at a particular state as fingerprint spectrum of the respective conformational change [74,81].

Changing chemical motifs within the structure can be used selectively to discriminate or emphasize vibrational modes (e.g. deuteration leads to a shift of amide I). Common methodological approaches in FTIR difference absorption spectroscopy are site-directed mutagenesis of amino acid side chains or isotopic labeling. Spectra are typically compared with model spectra of comparable molecules or which are achieved by normal mode analysis [81].

2.3.4 Surface-enhanced infrared absorption spectroscopy (SEIRAS)

Surface-enhanced infrared absorption spectroscopy (SEIRAS) is an IR spectroscopic technique, which uses an optimized technical set up and sample preparation methodology. The SEIRA effect benefits from the phenomenon, that IR absorption of molecules are altered when adsorbed to or near thin films or colloids of certain metals, transition metals (predominantly noble metals) or some polar dielectric nanostructures [82,83].

In this study, thin gold films were used. Therefore the mechanistic principles of surface enhancement of this noble metal are described below.

Motivated by studies on surface-enhanced Raman scattering (SERS) [84–

86], Hartstein *et al.* [87] observed for the first time enhanced IR absorption bands during a measurement characterizing organic molecules adsorbed to a noble metal film in Kretschmann ATR configuration. Although, the enhanced absorption signal was later corrected to be an oil contamination instead the organic analyte, the enhancement per se was doubtless and significant [88–90]. Extensive studies to understand the nature and mechanism of the SEIRA effect [88,89,91–98] lead to the rapid expansion of theoretical and experimental work on the effect as well as on exploiting the applicational potential along with growing interdisciplinary scientific interest.

From the experiment towards the SEIRA model

Surface-enhanced infrared absorption was observed in attenuated total reflection (ATR), transmission and in reflection experiments with metal-overlayer as well as metal-underlayer sample preparation. The first experimental results showed significant dependencies of the effect with regard to [83,89,94]:

- the metal type,
- the thickness and morphology of the metal layer surface (associated with the metals aggregation behavior and deposition methodology),
- the type of the analyte and thickness of the respective layer,
- the polarization state of the incident EM field,
- the angle of the incident beam and
- the orientation of the analyte molecule towards the surface and thus the manner of adsorption (i.e. chemi- or physisorbed).

Metal films of aggregated island-like nanostructures with pores and crevices had proven to be beneficial for the enhancement, in which the diameter of the islands are beneath the wavelength of the incident radiation [95,98]. Soon it became obvious that the total enhancement was most likely the result of at least two contributing components [91]. One component is effective within one molecular monolayer (short-range) and one extends some few monolayers (long-range) [83,93,96,98]. By analyzing the transmission spectra of various thick metal films revealed, it could be shown, that, depending on the thickness, the absorption range of the metal reaches into the mid-infrared (MIR). The

2. Theoretical Background

absorption intensities were linear proportional to observed enhanced absorption intensities of an organic analyte when adsorbed to such films. Therefore, an effect of surface plasmon resonance seemed to be very likely to explain the enhancement [96]. These and other experimental results were in very close concordance with observations for SERS [95]. Therefore, theoretical models for the enhancement mechanism of SEIRA were developed in analogy to the described SERS mechanism [82].

Although the detailed physical mechanism of the SEIRA effect is still unclear, the present general consensus describes two mechanisms predominately contributing to the total enhancement: an electromagnetic (EM) and a chemical mechanism [83].

The electromagnetic mechanism

The island-like structure of the metal films are approximated as packed prolate or oblate ellipsoids according to scanning electron microscopy (SEM) [82, 83]. A graphic illustration of the EM mechanism is depicted in figure 2.6.

The electric field (E-field) components of the incident field \vec{E}_{inc} , which are parallel to the macroscopic surface plane, excite surface plasmon or localized surface plasmon resonance within the thin metal film by polarization of its free electron gas density [83, 94, 95]. The resulting **induced dipole produces an E-field** \vec{E}_p , which is much stronger than \vec{E}_{inc} and decays very sharply with increasing distance from the metal surface, leading to a limitation of the enhancement effect within approximately one molecular monolayer distance [83, 99]. Thus, the enhanced E-field is the convolution of \vec{E}_p and \vec{E}_{inc} which acts on the analyte in the luminal space [83]. In that range, molecular vibrational modes can be excited which are observed as enhanced absorption of the incident radiation [83]. The enhanced E-field is stronger when densely packed metal islands interact, which is comparable to aggregated island-structures with pores and crevices [94]. The induced dipoles of neighboring islands can couple. It is even stronger close to the tip of spheroidal particles [99], or when enhanced E-fields of neighboring islands superpose as they decay into such pores and crevices. So, this effect is most prominent in the space between islands (referred in the literature as cavity site model) [94]. In the immediate vicinity of the local outer-metal surface the field lines of the enhanced E-field are oriented perpendicular to the local surface [98]. This explains the observed selectivity of the enhancement with regard to certain molecular vibrations, i.e. orientation dependency of the analyte towards the surface [93, 98], which is discussed in

the paragraph of the SEIRA **surface selection rule**.

Even more crucial at the metal interface and considered to be the most prominent contribution, is another **induced dipole** effect [83]: By dipole coupling between oscillating dipoles of **surface adsorbed molecules** with **local plasmon modes** at the metallic interface, the **polarizability of the metal changes** at frequencies of the molecular vibrations, thus the optical properties (i.e. transmittance and reflectance) of the thin metal film change too. It should be noted that the absorbance of metal islands in the MIR is much stronger as compared to molecular vibrations and the volume fraction of the metal is drastically higher than the one of the analyte layer. In that way, the rather small effect of locally changed metallic plasmon modes is amplified in a manner of an antenna.

Thus, the **orientation** of an analyte molecule is a key factor to explain the enhancement mechanism of SEIRA. However, the orientation is not just important for aligning molecular vibrations along an enhanced E-field, it also affects the enhancement, if it is beneficial for a parallel and in-phase alignment of similar vibrations from same neighbor molecules [83]. Based on this orientation effect, chemisorption of molecules to the metal film supports the enhancement effect rather than physisorption.

Calculations of the IR absorption enhancement factors by theoretical models delivered a qualitative picture of the mechanism, but no detailed quantitative one [82]. These models can be classified into three types: separated particle models, finite number of particle models, and film models. The latter agree best with experimental observations [82]. Since the particles are much smaller than the wavelength of the incident radiation, the metal/analyte-layer is considered as a composite layer with an effective dielectric function ϵ_{eff} [94, 100]. In that way, an absorption enhancement can be evaluated by calculating changes in transmittance or reflectance, respectively, as well as the average electric field strength within the metal layer by Fresnel's formula as three component system (e.g. substrate/composite layer/air) [82], which is discussed elsewhere [94, 98]. The effective dielectric function of a composite layer contains the electric properties of the layer [82]. Effective medium theories (EMT) deliver such ϵ_{eff} . For thin-films of aggregated metal-islands, enhancement factors for most of experimental data could be simulated by the Bruggeman effective medium approximation [98]. The advantage of this model is the consideration of also stronger interactions when islands are aggregated, e.g. dipole interactions [89].

2. Theoretical Background

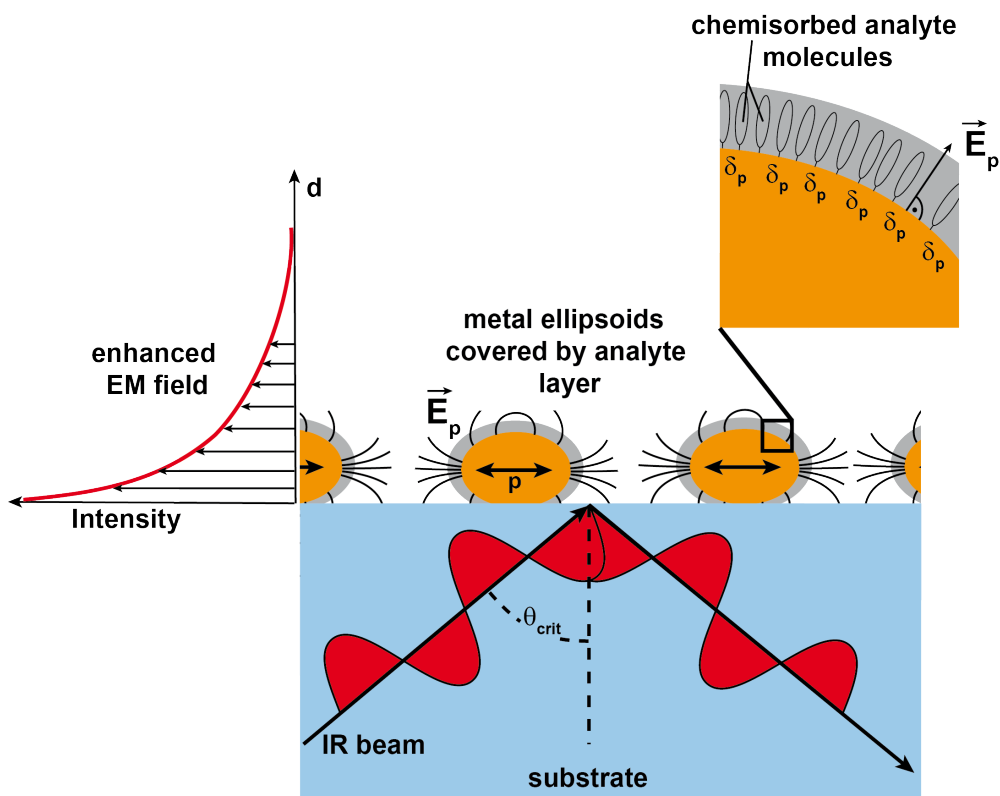


Figure 2.6: EM mechanism of ATR-SEIRA: An IR beam is totally reflected at the substrate/dielectric interface by the critical angle θ_{crit} . The surface is covered by a thin metal (orange) film coated by an analyte layer (gray), which are modeled as ellipsoids. The induced metallic dipole p is parallel to the macroscopic surface and produces a strong E-field \vec{E}_p (depicted as black field lines). The intensity of the enhanced EM field decays sharply with distance d to the surface (left graph). The cutout depicts chemisorbed analyte molecules with synchronous orientation to \vec{E}_p which is perpendicular to the local metal surface in immediate vicinity. Strong molecular vibrational modes can induce a local metal dipole δ_p at the interface. The figure was prepared using Adobe Illustrator CS5.

Other effects to explain the origin of SEIRA, as e.g. surface plasmon polariton waves or the mirror dipole effect, were discussed extensively but dismissed since they show poor agreements with the experimental data.

The chemical mechanism

Since chemisorbed molecules give larger enhancement intensities as compared to physisorbed molecules a chemical contribution to the total enhancement is suggested to be likely. The previous mentioned orientation effect can also be used to explain a possible coupling of strong neighboring molecular vibrational modes. But also hypotheses stressing models in terms of charge-transfer or "intensity borrowing" are discussed. But all of these discussions are speculative, which is why the chemical contribution to SEIRA is still under debate [83].

Surface selection rule and orientation of molecules on the surface

The experimental data revealed an enhancement selectivity of certain molecular vibrational modes and moreover the entire absence of certain modes when compared with classical FTIR spectra [93,98]. Comparison of SEIRA spectra with equivalent reflection absorption infrared spectroscopy (RAIRS) data showed concordance in the band spectrum. Thus, it was suggested that the RAIRS surface selection rule is valid for SEIRAS as well [98]. It says that molecular TDMs with their axis parallel to the acting enhanced EM field are enhanced most. This effect diminishes with increasing alignment of the TDM axis to be perpendicular to the field, where it finally disappears. Is the acting field perpendicular to the surface, this effect consequently becomes surface specific: Molecular vibrations perpendicular to the surface are most prominent and disappear with increasing parallel orientation towards the surface. Together with the short-range character of the SEIRA EM effect and the polarization of vibrational modes by chemisorption of the analyte to the surface, the rule explains the enhancement selectivity [83,98].

Chapter 3

Materials

Because of the today's standardization and transferable nature of standard chemicals, disposables and equipment, the following tables list kits, patented sample technologies, buffers, media etc., which are considered to be not as common or to be rare or sensitive for the study. Used chemicals were purchased at least in pro analysi (p.a.) grade. Thus, if not mentioned in this chapter or in the text, the respective chemical, tool, equipment etc. from an optional provider can be used.

Table 3.1: Chemicals

Designation	Supplier
Antarctic phosphatase and NEbuffer	New England Biolabs GmbH, Germany
all- <i>trans</i> retinal	Sigma Aldrich, Germany
Difco Brain Heart Infusion (BHI)	Becton, Dickinson and Company, Sparks, Maryland, USA
cOmplete TM protease inhibitor cocktail	Roche Deutschland Holding GmbH
DMSO (PCR Reagent)	DMSO, PCR Reagent, D9170, Sigma Aldrich, Germany
FastDigest [®] restriction enzymes and buffers	Fermentas Thermo Fisher Scientific Inc., USA
GeneJet TM plasmid miniprep kit	Fermentas Thermo Fisher Scientific Inc., USA
GeneJet TM gel extraction kit	Fermentas Thermo Fisher Scientific Inc., USA

GelRed TM nucleic acid gel stain	Biotium, Hayward, CA, USA
GeneRuler 1 kb Plus DNA ladder	Thermo Fisher Scientific Inc., USA
H ₂ SO ₄ 99.999 %	Sigma–Aldrich, Merck KGaA, Germany
Lipids	Avanti Polar Lipids Inc., USA
MembraneMax TM <i>HN</i> protein expression kit	Invitrogen TM Thermo Fisher Scientific Inc., USA
Ni-NTA affinity resin	Qiagen GmbH, Germany
Phusion [®] HF Polymerase and buffer	New England Biolabs GmbH, Germany
PURExpress [®] <i>In Vitro</i> Protein Synthesis kit E6800S	New England Biolabs GmbH, Germany
QIAGEN plasmid maxi kit	Qiagen GmbH, Germany
QIAquick gel extraction kit	Qiagen GmbH, Germany
Zero Blunt [®] PCR cloning kit	Invitrogen TM Thermo Fisher Scientific Inc., USA

Table 3.2: Plasmids

Plasmid name	Provider	Additional information	Plasmid map
pMSP1D1	Addgene Inc., USA	Addgene plasmid 20061, principle investigator Denisov <i>et al.</i> [101]	Appendix B, Fig. B.1
pEXP5–CT/bR	Invitrogen TM Thermo Fisher Scientific Inc., USA	MembraneMax TM <i>HN</i> protein expression kit	Appendix B, Fig. B.3

3. Materials

pRSET- EmGFP	Invitrogen™ Thermo Fisher Scientific Inc., USA	Appendix B, Fig. B.9
-----------------	--	-------------------------

Table 3.3: Primers

Primer name	Sequence
bRD96N:	
Forward primer	5' CCG CTG CTG CTG CTA AAT CTG GCT CTG CTG GTT 3'
Reverse primer	5' AAC CAG CAG AGC CAG ATT TAG CAG CAG CAG CGG 3'

Table 3.4: Cell strains

Designation	Genotyp	Selectable marker	Manufacturer
<i>E. coli</i> BL21CodonPlus (DE3)-RP	<i>argU</i> (AGA, AGG), <i>ileY</i> (AUA), <i>leuW</i> (CUA)	Chlor- amphenicol	Agilent Technologies GmbH & Co.KG, Waldbronn, Germany
<i>E. coli</i> TOP10	F- <i>mcrA</i> Δ (<i>mrr</i> - <i>hsdRMS-mcrBC</i>) Φ 80 <i>lacZ</i> Δ M15 Δ <i>lacX74 recA1</i> <i>araD139</i> Δ (<i>araleu</i>)7697 <i>galU</i> <i>galK rpsL</i> (StrR) <i>endA1 nupG</i>		Thermo Fisher Scientific Life Technologies GmbH, Darmstadt, Germany

Table 3.5: Media, buffer and solutions

Abbreviation	Ingredients	Concentration
dYT	Tryptone	1.6 % (w/v)
	Yeast extract	1 % (w/v)
	NaCl	0.5 % (w/v)
BHI	Difco Brain Heart Infusion	3.7 % (w/v)
dYT agar plate	Tryptone	1.6 % (w/v)
	Yeast extract	1 % (w/v)
	NaCl	0.5 % (w/v)
	Agar	2 % (w/v)
SDS-gel buffer 1	Tris-HCl, pH 6.8	0.5 M
	SDS	0.4 % (w/v)
SDS-gel buffer 2	Tris-HCl, pH 8.8	1.5 M
	SDS	0.4 % (w/v)
SDS running buffer	Glycerol	0.05 % (w/v)
	Tris-HCl	25 mM
	SDS	0.1 % (w/v)
CBB-R250 solution	Ethanol	10 % (w/v)
	Acidic acid	10 % (w/v)
	Coomassie Brilliant Blue R250	0.05 % (w/v)
Blue silver solution [102]	Coomassie Brilliant Blue G250	0.12 % (w/v)
	Ammonium sulfate	10 % (w/v)
	Phosphoric acid	10 % (v/v)
	Methanol	20 % (w/v)
SDS sample buffer	Urea	8 mM
	Tris-HCl	0.2 M
	SDS	2 % (w/v)
	Bromphenol blue	0.05 % (w/v)
	DTT	0.2 M
TAE buffer	Tris-HCl, pH 8	40 mM

3. Materials

	EDTA	2 mM
TBE buffer [10X], 1 L	Tris Base	162 g
	Boric acid	27.5 g
	EDTA sodium salt	9.3 g
	pH 8.3 to 8.7 at 50 °C	
Resuspension buffer	Tris HCl	40 mM
	NaCl	300 mM
	cOmplete™	1 tablet
	pH 8	
MSP buffer 1	Tris HCl	40 mM
	NaCl	300 mM
	Triton X-100	1 % (v/v)
	pH 8	
MSP buffer 2	Tris HCl	40 mM
	NaCl	300 mM
	Cholic acid	50 mM
	pH 8.9	
MSP buffer 3	Tris HCl	40 mM
	NaCl	300 mM
	pH 8	
MSP buffer 4	Tris HCl	40 mM
	NaCl	300 mM
	Imidazole	50 mM
	pH 8	
MSP buffer 5	Tris HCl	40 mM
	NaCl	300 mM
	Imidazole	150 mM
	pH 8	
MSP buffer 6	Tris HCl	40 mM
	NaCl	300 mM
	Glycerol	10 % (v/v)
	pH 8	
MSP buffer 7	Tris HCl	40 mM
	NaCl	100 mM

	pH 8	
TE buffer	Tris HCl	10 mM
	EDTA	1 mM
	pH 8.5	
NaPi [100 mM], ~ pH 7.4	Na ₂ HPO ₄ [100 mM]	77.4 mL
	NaH ₂ PO ₄ [100 mM]	22.6 mL

Table 3.6: Equipment and disposables

Designation	Manufacturer
Amicon [®] Ultra-15 centrifugal filter units (10 kDa nominal molecular weight limit (NMWL))	Merck Millipore, Merck KGaA, Germany
Amicon [®] Ultra-0.5 centrifugal filter devices (10 kDa MWCO)	Merck Millipore, Merck KGaA, Germany
ÄKTA avant 25	GE Healthcare, Germany
AUTOLAB [®] PGSTAT12	Eco Chemie B.V., Netherlands
Branson Sonifier [®] Cell Disruptor B-15	Branson Ultrasonic Corp. 1976, USA
Centriprep [®] centrifugal filter devices (10 kDa NMWL)	Merck Millipore, Merck KGaA, Germany
DuraSampIRII [™]	Smiths Detection, Smiths Group plc., UK
FluoroMax-3 [®] spectrofluorometer	HORIBA Jobin Yvon GmbH, Germany
Horiba LABRAM spectrometer	HORIBA Jobin Yvon GmbH, Germany
Krypton ion laser INNOVA90c	Coherent, USA

3. Materials

LKS.80 Laser Flash Photolysis Spectrometer (self-constructed setup)	According to Applied Photophysics Ltd., UK
MicroPulser TM Electroporator	Bio-Rad, Hercules, CA, USA
Spectra/Por [®] Float-A-Lyzer [®] G2 dialysis units (10 kDa molecular weight cut-off (MWCO))	Sigma-Aldrich, Merck KGaA, Germany
Superdex 200 10/300 GL column	GE Healthcare, Germany
UV/Vis absorption spectrometer NanoDrop2000c	Thermo Fisher Scientific Inc., USA
UV/Vis spectrophotometer UV-2401 PC	Shimadzu Europa GmbH, Germany
Vertex 70 v	Bruker Corporation, USA
Vertex 80 v	Bruker Corporation, USA

Table 3.7: Databases, software and online tools

Designation	Provider
Adobe Master Collection CS5	Adobe Systems Inc., USA
ChemSketch	Advanced Chemistry Development Inc., Canada
Fluorescence SpectraViewer	Thermo Fisher Scientific Inc., USA
GeneBank [®]	National Center for Biotechnology Information, U.S. National Library of Medicine, Bethesda MD, USA

Gwyddion2.37	Petr Klapetek, Department of Nanometrology, Czech Metrology Institute, Czech Republic; David Necas, Plasma Technologies, CEITEC - Central European Institute of Technology, Masaryk University, Czech Republic
Gpes4.9	Eco Chemie B.V., Netherlands
LabSpec	HORIBA Jobin Yvon GmbH, Germany
LKS software	Laser Flash Photolysis Spectrometer Software, Applied Photophysics Ltd., United Kingdom
Matlab	The MathWorks Inc., USA
NCBI BLAST [®]	National Center for Biotechnology Information, U.S. National Library of Medicine, Bethesda MD, USA
SnapGene [®] 3.3.3	GSL Biotech LLC, USA
OPUS	Bruker Corporation, USA
Origin9.0	OriginLab Corporation, USA
ProtParam	SIB ExpASy Bioinformatics Resources Portal, SIB Swiss Institute of Bioinformatics [103]
Protein data bank RCSB PDB	www.rcsb.org [104]
UNICORN [™] 6.1	GE Healthcare, Germany
UV probe software Version 2.32	Shimadzu Europa GmbH, Germany
VMD1.9.1	Developed with NIH support by the Theoretical and Computational Biophysics group at the Beckman Institute, University of Illinois at Urbana-Champaign, USA; http://www.ks.uiuc.edu/

Chapter 4

Methods

If not indicated otherwise, MilliQ–water (18.2 M Ω) or deionized water were used as solvent for buffers and solutions or media, respectively, and experiments were performed at room temperature.

4.1 Standard methods

4.1.1 Preparation and transformation of competent *E. coli* cells

Electrocompetent *E. coli* cells were prepared following the manufacturers application sheet of the MicroPulserTM Electroporator (operating instructions and applications guide, section 5 and 11). Chemical competent cells were prepared following the method of Hanahan [105, 106]. The samples for either electrotransformation or heat shock transformation were mixed as follows. For electrotransformation, 40 μ l of electrocompetent cells from a cryoculture were mixed with 1 μ L or ca. 1 ng plasmid DNA, 1–10 μ L ligation product or amplified plasmid (purified via agarose gel). For heat shock transformation, 100 μ L chemical competent cells were mixed with either 1 μ L or ca. 1 ng plasmid DNA or 5–20 μ L ligation product or agarose gel extracted DNA, respectively. The used cryocultures contained BHI or dYT medium with 40 % (v/v) glycerin final concentration. The electrotransformation was performed according to the manufacturers instructions. For the heat shock transformation (according to Hanahan [105]) the samples were incubated on ice for 30 min. Thereafter, the cells were heat shocked by incubation at 42 °C for 90–120 s. Subsequently, the cells were set on ice for further two minutes. For both methods, after transformation, the cell samples were mixed with 1 mL dYT medium and cultured at 37 °C for 30–60 min. The selection was performed by culturing the cells on a dYT agar plate containing the respective antibiotics.

4.1.2 Sodium Dodecyl Sulfate Polyacrylamide Gel Electrophoresis (SDS-PAGE)

For protein analysis, standard sodium dodecyl sulfate polyacrylamide gel electrophoresis (SDS-PAGE) [1, 107] using a 4 % collecting gel and a 15 % separating gel, was utilized. The composition of the gels is documented in table 4.1.

Table 4.1: Ingredients for an SDS-PAGE to analyze protein samples.

SDS gel	Ingredients	Volume
4 % Collecting gel	Acrylamide/ Bisacrylamide [30 %]	640 μ L
	H ₂ O	3.04 mL
	SDS-Gel buffer 1, pH 6.8	1.24 mL
	APS [10 % (w/v)]	45 μ L
	TEMED	5 μ L
15 % Separating gel (5.5 mm x 8.5 mm x 0.75 mm) = width x height x depth)	Acrylamide/ Bisacrylamide [30 %]	3 mL
	H ₂ O	1.44 mL
	SDS-Gel buffer 2, pH 8.8	1.5 mL
	APS [10 % (w/v)]	60 μ L
	TEMED	6 μ L

In order to prepare and denature the sample for the SDS-PAGE, the sample was mixed with SDS sample buffer 4:1 (usually 20 μ L final volume). To evaluate the molecular weight of the protein bands afterward, different commercial protein molecular weight markers were applied. Which one was used will be indicated at the respective figure of the gel. The employed SDS running buffer is listed in table 3.5. After the SDS-PAGE was processed (running condition: ca. 200 V), the gel containing the separated protein sample was stained by either CBB-R250 solution or blue silver solution [102]. After usually one night incubation at room temperature under rocking conditions, the gel was destained by incubation with 10 % (v/v) acidic acid under the same conditions.

4.1.3 Agarose Gel Electrophoresis

For DNA analysis, standard agarose gel electrophoreses [1] was performed. Therefore, 1 % (w/v) agarose was solved in TAE buffer, which was also the running buffer used for the electrophoresis. In order to stain the sample DNA, the gel was supplemented with GelRedTM (dilution 1:10000). GelRedTM inter-

4. Methods

calates in nucleic acids, which can be visualized in this way by ultra violet (UV) light. The sample was mixed with 10X Fast Digest Green Buffer before loading it onto the gel. To evaluate the size distribution of the DNA fragments in the gel after the electrophoresis, the molecular weight marker GeneRuler 1 kb Plus DNA ladder was used.

4.1.4 Sequencing

DNA samples were analyzed by sequencing, using the sequencing service of Eurofins Genomics GmbH (Germany).

4.2 Protein constructs for protein expression

4.2.1 Bacteriorhodopsin (bR) and bR variants

Bacteriorhodopsin (bR)

For the studies on bR folding, the plasmid pEXP5-CT/bR was used for cell-free protein expression and as template for bR variants (provided by the protein expression kit MembraneMaxTM HN; see appendix B Fig. B.3). The plasmid carries a synthetic gene for bR, which encodes a 249 amino acid big protein (26.9 kDa). The sequence was approved by DNA sequencing using the service Eurofins Genomics GmbH and evaluated using NCBI BLAST[®], which matched the database GeneBank[®] accession number entry AAA72184.1 (bacteriorhodopsin; synthetic construct) of 100 %. For the nucleotide sequence and protein parameters see appendix B, figure B.4 and table B.1. Cell-free expressed bR using this template DNA was analyzed by laser flash photolysis in section 4.5.4.

Plasmid propagation:

Chemically competent *E. coli* TOP10 were heat shock transformed with pEXP5-CT/bR. After cell culture on a dYT agar plate (with 200 µg/mL ampicillin final concentration), one colony forming unit (CFU) was cultured in 3–5 mL dYT medium including 200 µg/mL ampicillin final concentration at 37 °C over night. The plasmid was extracted using the QIAGEN plasmid maxi kit and tested for yield and purity by the UV/Vis absorption spectrometer NanoDrop-2000c measuring the absorption at 260 nm, 280 nm and 230 nm. The plasmid was eluted and stored in TE buffer or 10 mM Tris (pH 8-9), respectively, at -20 °C.

BR variant D96N (bRD96N)

The point mutation was introduced by QuikChange site-directed mutagenesis (based on [108]) using pEXP5-CT/bR (appendix B, Fig. B.3) as template with a concentration of 0.18 $\mu\text{g}/\mu\text{L}$ including the respective primers (Tab. 3.3).

PCR protocol:

Milli-Q [®] water (18.2 M Ω)		35.5 μl
Phusion [®] HF buffer	5x	10 μl
dNTP Set	[10mM]	1 μl
Foward primer (Tab. 3.3)	[100 pmol/ μl]	1.5 μl
Reverse primer (Tab. 3.3)	[100 pmol/ μl]	1.5 μl
pEXP5-CT/bR	[0.16 $\mu\text{g}/\mu\text{l}$]	1 μl
Phusion [®] DNA Polymerase		0.5 μl
Cycling conditions:	1) 98 °C	30 s
	2) 98 °C	10 s
	3) 60 °C	60 s
	4) 72 °C	2 min
	loop: 2)–4)	18 times
	5) 72 °C	3 min
	6) 4 °C	hold

The template DNA, deoxynucleotide triphosphate (dNTP) Set and primers were dissolved in TE buffer (pH 7.4) to the final concentrations.

Plasmid isolation:

The PCR-product was digested by 1 μL FastDigest[®] *DpnI* at 37 °C for 1 h. Plasmids amplified in a bacterial host are methylated, which is not the case for PCR products. *DpnI* digests methylated DNA. Thus, the template DNA will be digested whereas the PCR product remains unharmed and can be purified. After digestion, the PCR product was purified using components from the GeneJET[™] plasmid miniprep kit. Therefore, the PCR product was mixed with isopropanol containing buffer in a ratio of 1:5 and purified by solid phase extraction passing the mix through a GeneJET[™] spin column following the manufactures application sheet. The column was washed by ethanol containing buffer 5 times before elution with 10 mM Tris HCl, pH 8. Thereafter, the

4. Methods

plasmid was transferred into electrocompetent *E. coli* TOP10 by electrotransformation. The cells were cultured on a dYT agar plate (supplemented with 200 µg/mL ampicillin final concentration) at 37 °C over night. Afterwards, 6 colonies were picked and cultured in 3 mL dYT medium with 200 µg/mL ampicillin final concentration at 37 °C over night. The plasmid was eluted with 10 mM Tris HCl, pH 8.

Characterization:

The template plasmid pEXP5-CT/bR (appendix B, Fig. B.3) has two restriction sites for *Bgl*II, at 370 bp (in the *bop* gene) and 3417 bp (in the vector). By introduction of the point mutation D96N, the first site is removed and should result in one band instead of two on an agarose gel. Consequently, a 5 µL DNA sample of each clone was digested by 1 µL FastDigest® *Bgl*II for 1 h. The digest was analyzed by 1% (m/v) agarose gel electrophoresis. The construct which showed the expected band in the gel was sequenced by the service Eurofins Genomics GmbH. The sequence and the protein parameter are shown in appendix B, figure B.5 and table B.1, respectively. Additionally, to verify the mutation, the slowed-down photocycle of the variants translation product was analyzed by laser flash photolysis (see section 4.5.4).

4.2.2 Other α -helical membrane proteins

For the cell-free expression of *Hs*SRI, *Hs*SRII and *Cr*ChR2, the following plasmids were used, which encode the respective apoprotein (courtesy of Dr. Ramona Schlesinger, FU Berlin, Germany):

- pEXP5-CT/SopI
- pEXP5-CT/SopII
- pET-27b/Chop2

The construct sequences (sensory opsin I (SopI) Fig. B.6, sensory opsin II (SopII) Fig. B.7 and channelopsin 2 (Chop2) Fig. B.8) and protein parameters (Tab. B.1) are documented in appendix B. According to the provider, the genes for SopI and SopII were cloned from another vector into pEXP5-CT/bR by substitution of the gene for bR with the respective target gene. The original plasmids were used for the successful heterologous expression of *Hs*SRI [36] and *Hs*SRII [37]¹ in *E. coli*. The construct for Chop2 is the transmembrane part

¹ Later, it turned out, that the first N-terminal 15 amino acids were deleted. Nevertheless, *Hs*SRII was expressed successfully.

of the wild-type sequence, i.e. aa 1 to 307 (compare GeneBank[®] accession number entry AF461397) which was fused to a C-terminal 10xHis-tag.

4.2.3 Emerald green fluorescent protein (EmGFP)

The plasmid pRSET-EmGFP (Appendix B, Fig. B.9) was applied in the cell-free EmGFP expression experiments. The sequence and protein parameters are documented in appendix B, figure B.10 and table B.1.

4.3 Nanodiscs

4.3.1 Commercial nanodiscs

For most experiments nanodiscs from the MembraneMax[™] HN protein expression kit were used. These are discoidal 1,2-dimyristoyl-*sn*-glycero-3-phosphocholine (DMPC) bilayers with 10 nm in diameter and 5 nm in height, each wrapped by two 6xHis-tagged, α -helical MSPs in a belt-like fashion [109]. The membrane scaffold protein was not further described by the manufacturer.

4.3.2 Membrane scaffold protein MSP1D1 and nanodisc assembly

For expression of MSP1D1 the plasmid pMSP1D1 (see Tab. 3.2) was used. The gene which carries a coding sequence for a heptahistidine-tag (7xHis-tag) at its 5'-end is implemented upstream into pET-28a(+) in between the *NcoI* and *HindIII* restriction site within the multiple cloning site (MCS). The vector carries a kanamycin (Kan) coding sequence. MSP1D1 was approved by sequencing using the sequencing service Eurofins Genomics GmbH, Germany. The sequence and important protein parameter are shown in appendix B, figure B.2 and table B.1, respectively. The construct is shorter than MSP1, obtained by the deletion of a fragment coding for the first half α -helix (compare Fig. 2.2). It is supposed to assemble mechanically more stable nanodiscs [110], which resist a broader pH range. The diameter is about 10 nm, whereas the height depends on the applied lipid (for DMPC: 5 nm) [101].

MSP1D1 expression

Elektrocompetent *E. coli* BL21CodonPlus(DE3)-RP cells were transformed with pMSP1D1. The transformed cells were cultured at 37 °C in 500 mL dYT medium containing 50 μ g/mL final concentration kanamycin using baffled flasks. During cell culture the optical density (OD) was monitored by the UV/Vis absorption spectrometer NanoDrop2000c. When OD 0.8 was reached, the protein expression was induced by 1 mM IPTG final concentration and further incubated for 4 h. The cells were harvested by centrifugation at 6000 x g

4. Methods

at 4 °C for 10 min with subsequent resuspension in PBS and repeated centrifugation as before. The bacterial cell pellet of 1 L cell culture was shock frozen by liquid nitrogen and stored at -80 °C.

MSP1D1 purification [111]

The cell pellet of 1 L cell culture was resuspended in 50 mL ice cold resuspension buffer using a 25 mL Pasteur glass pipette. Triton X-100 was added with a final concentration of 1 % (v/v). Thereafter, cells were disrupted by ultrasonication on ice using the Branson Sonifier[®] Cell Disruptor B-15, 4 times 60 sec and 4 times 45 sec, with 1 min cooling time in between each sonication. The lysate was centrifuged at 30,000 x g at 4 °C for 25 min. Subsequently, the supernatant was filtered using a syringe filter with 0.45 μ m pore size. A self-made immobilized metal affinity chromatography (IMAC) column (10 mL bed volume Ni-NTA) was equilibrated by means of 5 column volumes (CVs) MSP-buffer 1. The filtered supernatant was passed through the column. Afterwards, the column was consecutively washed starting with MSP-buffer 1, than 2, 3 and finally 4, each with 5 CVs. Following, MSP1D1 was eluted by MSP-buffer 5. Usually, first a 5 mL, second and third a 15 mL and finally again a 5 mL fraction was collected. The elution fractions were immediately supplemented with glycerol, 10 % (v/v) final concentration. All eluates, including the wash fractions and the flow through, were analyzed by a 15 % SDS-PAGE using the molecular weight marker PageRuler[™] Plus Prestained Protein Ladder (Thermo Fisher Scientific Inc., USA). The MSP1D1 containing fractions were pooled and concentrated by means of an Amicon[®] Ultra-15 centrifugal filter unit (10 kDa NMWL) by following the manufacturers instructions. The pool was centrifuged at 3000 x g for 30 min several times until 1 to 2 mL sample volume remained. To remove the imidazole, the concentrates were resuspended in MSP-buffer 6 and centrifuged again. This cycle was repeated until the final imidazole concentration of approximately 5 μ M was reached. The protein concentration was estimated by using the UV/Vis absorption spectrometer NanoDrop2000c measuring the absorption at 280 nm and using the extinction coefficient of 19940 M⁻¹cm⁻¹ for MSP1D1. The concentrate was shock frozen by liquid nitrogen and stored at -80 °C.

Nanodisc assembly [112]

The assembly mix was prepared by keeping the molar ratios recommended by Sligar *et al.* [57]. MSP1D1 (100 μ M final concentration) was mixed with DMPC

in a molar ratio of 1 : 80 in MSP–buffer 6 with n-dodecylphosphocholine (DPC) (0.1 % (w/v) final concentration). The aqueous DMPC stock solution contained sodium cholate in a ratio of 1 : 3. The batch was carefully inter-mixed using a table–top rotator at room temperature for 1 h. For dialysis, Spectra/Por[®] Float–A–Lyzer[®]G2 dialysis units (10 kDa MWCO) were equilibrated by incubation in MSP–buffer 6 at room temperature for at least 15 min. The assembly mix was dialysed against the 10³–fold volume of MSP–buffer 7 at room temperature for 12 to 24 h. The dialysis step was repeated 4 times at 4°C. Thereafter, the mix was centrifuged at 21,000 x g at 4°C for 10 min. The supernatant was concentrated by using Centriprep[®] centrifugal filter devices (10 kDa NMWL) using a swinging bucket rotor and following the manufacturers instructions. The devices were equilibrated by MSP–buffer 7 in a prior centrifugal step. The concentrate was centrifuged at 21,000 x g at 4°C for 10 min. Afterward, it was shock frozen by liquid nitrogen and stored at -80 °C.

Nanodisc characterization

The concentration of MSPD1 was calculated from the absorbance at 280 nm measured with a NanoDrop200c using the extinction coefficient of 19940 M⁻¹cm⁻¹ for MSP1D1. The calculated concentration was divided by two, since two MSPs are supposed to assemble one nanodisc. To evaluate the quality of the prepared nanodisc sample, a fraction was analyzed by size exclusion chromatography (SEC) at 4 °C using a Superdex 200 10/300 GL column in the ÄKTA avant protein purification system with the software UNICORN[™] 6.1 following the manufacturers recommendations. Furthermore, a sample of such nanodiscs was imaged by negative staining in an electron microscopy experiment in collaboration with Prof. Holger Stark, MPI Goettingen, Germany (see section 4.4.4).

4.4 Cell–free protein expression

For experiments in batch and on the SEIRA sample surface, two commercial, coupled cell–free protein expression systems were used. If not stated otherwise, they were applied according to the manufacturers application sheet. The standard protocol and technical details are described in the following two paragraphs.

4. Methods

4.4.1 MembraneMaxTMHN protein expression kit

The MembraneMaxTMHN protein expression kit is an *E. coli* based cell-free protein synthesis system for high-throughput membrane protein expression. Transcription and translation were initiated by adding the template DNA. The kit components were [109]:

- The MembraneMaxTMHN Reagent containing nanodiscs consisting of DMPC with approximately 10 nm in diameter. Each nanodisc is 6xHis-tagged by their two membrane scaffold proteins. The precise membrane scaffold protein construct and the solvent is not described,
- The *E. coli* cell lysat extract *slyD*,
- An reaction (2.5X IVPS) and feed buffer (2XIVPS) for ATP regeneration including salts and other substrates,
- An amino acid mix without methionine,
- Methionine,
- An T7 Enzyme Mix, which contains T7 RNA polymerase.

Detailed description of the chemical composition of the solutions was not provided. For a batch experiment in a test tube, the cell-free protein expression reaction with 100 μL final volume was performed as follows:

1. Preparation of the reaction mix:

<i>E. coli slyD</i> Extract	20 μL
2.5X IVPS Reaction buffer (-amino acids)	20 μL
50 mM Amino Acids (-Met)	1.25 μL
75 mM Methionine	1 μL
MembraneMax TM HN Reagent	2 μL
T7 Enzyme Mix	1 μL
DNA template	1 μg
DNase/RNase-Free Water	to 50 μL

2. Incubation at 37°C, 1200 rpm for 30 min.

3. Preparation of the feeding mix:

2X IVPS Feed buffer (-amino acids)	25 μL
50 mM Amino Acids (-Met)	1.25 μL
75 mM Methionine	1 μL
10 mM all- <i>trans</i> retinal	0.5 μL
DNase/RNase-Free Water	to 50 μL

Here, the chromophore was purchased from Sigma Aldrich as it gave better results as the retinal from the kit. Therefore, a stock solution was prepared by dissolving all-*trans* retinal in ethanol to a final concentration of 25 mM. Subsequently, it was diluted to 10 mM in MilliQ-water.

4. Addition of the feeding mix (from step 3) to the reaction mix after 30 min incubation (from step 2).
5. Incubation for 1.5 to 2 h.

4.4.2 PURExpress[®] *In Vitro* Protein Synthesis kit E6800S

The PURExpress[®] *In Vitro* Protein Synthesis kit E6800S is a cell-free transcription/translation system based on purified recombinant components necessary for *E. coli* protein translation. Thus the ingredients of the reaction solutions are completely known and free of contaminants like exonucleases, RNases, and proteases. Furthermore, target proteins are free of post-translational modifications. Transcription and translation were initiated by adding the template DNA and are based on the T7 RNA polymerase/promoter system [113].

Detailed description of the chemical compositions was not provided. For an experiment in a test tube (in batch), the cell-free protein expression reaction was performed as follows:

1. Combination of the reagents analogous to:

Solution A	10 μ L
Solution B	7.5 μ L
DNA template	10 ng/ μ L final concentration
DNase/RNase-Free Water	to 25 μ L

2. Incubation at 37°C for 2 h.

4.4.3 Expression of bR into commercial nanodiscs

The commercial nanodiscs provided by the MembraneMax[™] *HN* protein expression kit were used to express bR from pEXP5-CT/bR by the MembraneMax[™] *HN* protein expression kit and by the PURExpress[®] *In Vitro* Protein Synthesis kit E6800S. Therefore, both systems were applied in batch mode following the respective standard protocol (sections 4.4.1 and 4.4.2) according to the manufacturers application sheets [109, 113]. Note, regarding the PURExpress[®] system, for bR expression the standard protocol was additionally supplemented with all-*trans* retinal and nanodiscs, each with final concentrations as used in the protocol of the MembraneMax[™] *HN* kit. For each system

4. Methods

two samples were prepared (each with a final volume of 100 μL): a positive control (with template DNA) and a negative control (without DNA). Subsequently, the samples were centrifuged at 21000 x g, at 4 $^{\circ}\text{C}$ for 10 min. The supernatants were analyzed by the UV/Vis spectrophotometer UV-2401 PC using the UV probe software Version 2.32.

The supernatants of the MembraneMaxTM *HN* kit were additionally purified by Ni-NTA affinity chromatography as follows. The samples (each 100 μL) were added to 1 mL equilibrated Ni-NTA affinity resin (corresponded to 500 μL bed volume). For equilibration 50 mM NaPi, 500 mM NaCl, pH 8 was used. For binding, the samples were incubated rotating at 4 $^{\circ}\text{C}$ over night. The next day, the suspensions were centrifuged at 10000 x g at 4 $^{\circ}\text{C}$ for 5 min (supernatant = flow through). Thereafter, the remaining Ni-NTA bed of each sample was washed twice with 1 mL 50 mM NaPi, 500 mM NaCl, pH 8 and subsequently once with 1 mL 50 mM NaPi, 500 mM NaCl, 20 mM Imidazol, pH 8. For every wash, the samples were incubated rotating at 4 $^{\circ}\text{C}$ for 5 min and then centrifuged at 10000 x g at 4 $^{\circ}\text{C}$ for 5 min (supernatant = wash). After the third wash, the analytes were eluted as follows. For each sample, three elution steps were performed: First the remaining Ni-NTA bed was incubated with 1 mL 50 mM NaPi, 500 mM NaCl, 250 mM Imidazol, pH 8 rotating at 4 $^{\circ}\text{C}$ for 5 min. Thereafter, the suspension was centrifuged at 10000 x g at 4 $^{\circ}\text{C}$ for 5 min (supernatant = elution 1). Secondly, the first elution step was repeated (supernatant = elution 2). Third, the first elution step was repeated but using 50 mM NaPi, 500 mM NaCl, 500 mM Imidazol, pH 8 (supernatant = elution 3). Afterwards, flow through, washing fractions and eluates were analyzed by 15 % SDS-PAGE using the molecular weight marker BenchMarkTM Protein Ladder (InvitrogenTM |Thermo Fisher Scientific Inc., USA). The supernatants of the MembraneMaxTM *HN* kit were additionally purified by Ni-NTA affinity chromatography as follows. The samples (each 100 μL) were added to 1 mL equilibrated Ni-NTA affinity resin (corresponded to 500 μL bed volume). For equilibration 50 mM NaPi, 500 mM NaCl, pH 8 was used. For binding, the samples were incubated rotating at 4 $^{\circ}\text{C}$ over night. The next day, the suspensions were centrifuged at 10000 x g at 4 $^{\circ}\text{C}$ for 5 min (supernatant = flow through). Thereafter, the remaining Ni-NTA bed of each sample was washed twice with 1 mL 50 mM NaPi, 500 mM NaCl, pH 8 and subsequently once with 1 mL 50 mM NaPi, 500 mM NaCl, 20 mM Imidazol, pH 8. For every wash, the samples were incubated rotating at 4 $^{\circ}\text{C}$ for 5 min and then centrifuged at 10000 x g at 4 $^{\circ}\text{C}$ for 5 min (supernatant = wash). After

the third wash, the analytes were eluted as follows. For each sample, three elution steps were performed: First the remaining Ni-NTA bed was incubated with 1 mL 50 mM NaPi, 500 mM NaCl, 250 mM Imidazol, pH 8 rotating at 4 °C for 5 min. Thereafter, the suspension was centrifuged at 10000 x g at 4 °C for 5 min (supernatant = elution 1). Secondly, the first elution step was repeated (supernatant = elution 2). Third, the first elution step was repeated but using 50 mM NaPi, 500 mM NaCl, 500 mM Imidazol, pH 8 (supernatant = elution 3). Afterwards, flow through, washing fractions and eluates were analyzed by 15 % SDS-PAGE using the molecular weight marker BenchMark™ Protein Ladder (Invitrogen™ |Thermo Fisher Scientific Inc., USA).

4.4.4 Expression of bR into MSP1D1/DMPC nanodiscs

In collaboration with Dr. Sameer Singh (ICS-6, Research Centre Juelich GmbH, Germany), Dr. Gunnar Schroeder (ICS-6, Research Centre Juelich GmbH, Germany) and Prof. Holger Stark (Max Planck Institute for Biophysical Chemistry Goettingen, Germany) bR incorporated in nanodiscs was prepared for visualization by 3D-cryogenic transmission electron microscopy (cryo-TEM). Self-made nanodiscs (see section 4.3.2) were used to cell-free express bR using the plasmid pEXP5-CT/bR and the MembraneMax™ *HN* protein expression kit. After the reaction took place, the reaction mix was purified by default histidine-tag Ni-NTA affinity chromatography on 0.5 mL bed volume of Ni-NTA affinity resin, which was equilibrated by 40 mM Tris-HCL, 300 mM NaCl, 50 mM Imidazol, pH 8. In detail, 200 µL reaction mix were added to the equilibrated bed of Ni-NTA affinity resin, mixed gently and loaded onto an empty column with 0.4 cm radius. After collecting the flow through, the purple-looking bed was washed by 2 mL equilibration buffer. Thereafter, the analyte was eluted with 1 mL 40 mM Tris-HCL, 300 mM NaCl, 300 mM Imidazol, pH 8. Subsequently, the eluate was further purified by SEC at 4 °C using a Superdex 200 10/300 GL column in the ÄKTA avant protein purification system with the software UNICORN™ 6.1 following the manufacturers recommendations. The fractions of interest were analyzed by standard 15 % SDS-PAGE (using the the molecular weight marker PageRuler™ Prestained Protein Ladder, Fermentas™ |Thermo Fisher Scientific Inc., USA) and negative staining (the latter by Prof. Holger Stark).

4. Methods

4.4.5 Expression of other microbial rhodopsins into nanodiscs

Cell-free protein expression experiments in batch were prepared using the MembraneMaxTM *HN* kit and both previously described nanodisc types to synthesize *HsSRI*, *HsSRII* and *CrChR2*. The reaction products were purified by histidine-tag Ni-NTA affinity chromatography (see section 4.4.4) and analyzed by 15 % SDS-PAGE.

4.5 SEIRAS experiments on membrane protein folding *in situ*

4.5.1 Instrumentation

The SEIRAS setup consists of an ATR optic mounted in the FTIR spectrometer Vertex 70 v (containing a Globar, a ROCKSOLIDTM interferometer, a helium neon (HeNe) laser and a photovoltaic mercury cadmium telluride (MCT) detector) using the software OPUS.

The IR radiation was generated by a Globar and coupled to a ROCKSOLIDTM interferometer. In contrast to classical interferometers using planar mirrors in Michelson configuration, this interferometer type uses retroreflecting cube corner mirrors in a patented pendulum arrangement. By that, mirror delocalizations are strongly reduced, which is highly important with regard to the stability of the measurement, resolution and spectral quality (e.g. high signal-to-noise ratio). A HeNe laser (632.8 nm; 5 mW) is coupled parallel to the IR beam to adjust the beam line. Leaving the interferometer unit, the IR beam enters the evacuated sample chamber. The beam path and default settings of the Vertex 70 v are schematically depicted in Fig. 4.1.

Evacuation of the chamber reduces disturbing signals mainly caused by water vapor and CO₂. By employing an ATR optical setup in Kretschmann configuration [114], the IR beam is directed to a triangular silicon prism, penetrates it and is totally reflected (single reflection 60° incident angle) at the surface planar with the gold film deposited atop. When a light beam passes a boundary surface from a medium with high refractive index n_1 (for silicon 3.35 at 633 nm [115]) towards a medium with low refractive index n_2 (for water 1.33 at 589 nm [116]) the beam gets totally reflected, if the angle of the incident light beam θ is bigger than the critical angle θ_c (for silicon and water 23.37°) with

$$\theta_c = \arcsin(n_2/n_1) \tag{4.1}$$

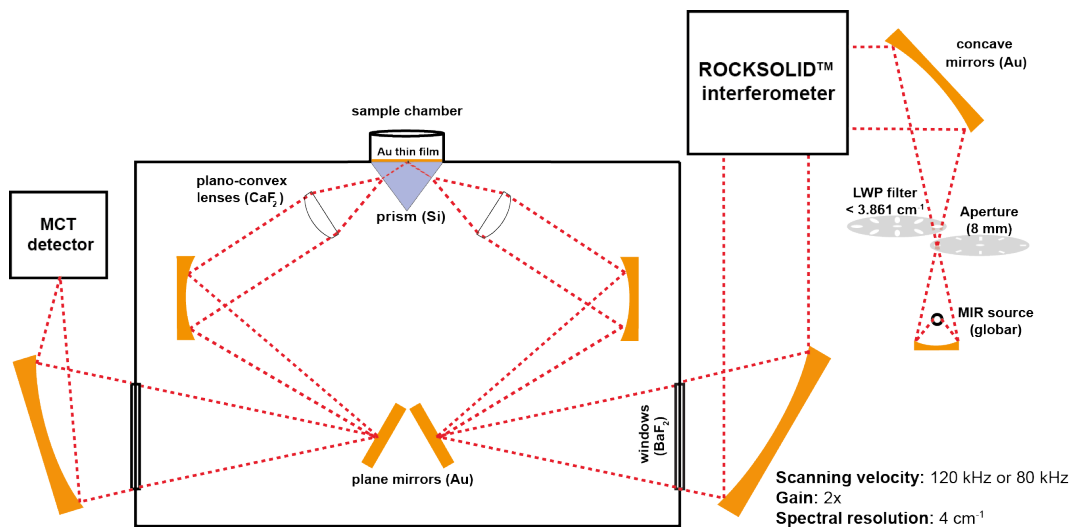


Figure 4.1: Optical path of the IR beam during the SEIRAS measurement with ATR optics in Kretschmann configuration [114] including default settings of the FTIR spectrometer Vertex 70 v.

In case of a metal coated surface, part of the generated evanescent electromagnetic field is absorbed by the metal film which causes surface plasmon resonance. The reflected beam is directed to a photovoltaic MCT detector, which is cooled by liquid nitrogen.

4.5.2 Surface preparation

4.5.2.1 Ni-NTA SAM to immobilize nanodiscs to the SEIRAS prism

To prepare the gold film, the reflective site of a triangular silicon prism was modified by chemical deposition [117]. The silicon prism was cleaned by cooking in piranha solution (37 % HCl : milliQ H₂O : 30 % H₂O₂ = 1 : 1 : 1) at 100 °C for 5 to 10 min. In the second step, the clean reflective site was chemomechanically polished by means of a water dispersion of aluminum oxide (Al₂O₃) until hydrophobicity of the surface could be observed. Afterwards, the surface was covered with 40 % ammonium fluoride (NH₄F) aqueous solution at room temperature for 1 min for activation with fluoride groups. To deposit the gold, the surface was exposed to a mixture of 2 % HF : reduction solution : 0.03 M NaAuCl₄ = 1 : 1 : 1 at 60 °C for 1.5 min. The reduction agent was composed of aqueous 0.3 M sodium sulfite (Na₂SO₃), 0.1 M sodium thiosulfate (Na₂S₂O₃) and 0.1 M ammonium chloride (NH₄Cl). The prism was washed with milliQ water between each step. [81, 118]

Impurities on the prepared gold film were removed by employing cyclic voltammetry. Therefore, the potentiostat/galvanostat AUTOLAB® PGSTAT12

4. Methods

including the software Gpes4.9 was used. The prism was mounted into the self-made, electrochemical sample cell with a gold wire as working electrode, an Ag/AgCl reference electrode, a platinum wire as counter electrode and 0.1 M H₂SO₄ as electrolyte solution (prepared from a 99.999 % stock solution). By default, three cycles were performed between 0.1 V and 1.4 V until solely oxidation and reduction of gold could be observed [81].

Gold surfaces prepared by this method show typically a dense island-structured shape with an island diameter of about 50 – 100 nm (Fig.4.2) and a thickness of 20 – 200 nm [119]. The gold-coated prism was mounted into a Teflon cell which was fixed in the sample chamber of the FTIR spectrometer (Fig. 4.1).

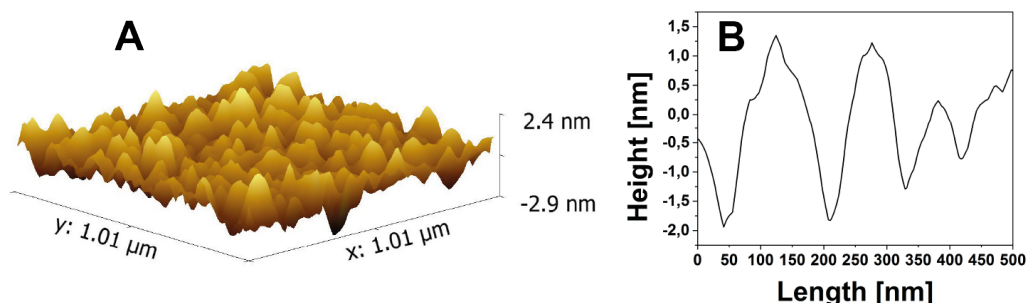


Figure 4.2: Representative cut-out of a gold film prepared by the described method (AFM data by courtesy of Elmar Hubrich, FU Berlin, Germany): (A) Graphic representation of the island-structured gold film by 3D imaging; (B) One line profile with 1 pixel thickness of the cut-out (A); Data were treated by the program Gwyddion2.37.

To build up a nickel nitrilotriacetic acid (Ni-NTA) self-assembled monolayer (SAM) (described in [81,118]) the gold film was exposed to 2.5 mM 3',3-Dithio-bis(N-succinimidylpropionate) (DTSP) in water free dimethylsulfoxid (DMSO) for 30 min to form the first linker molecule (thio-(N-succinimidylpropionate) (TSP)) on the surface covalently bound via a sulfur group to the gold substrate. The development of the monolayer as well as the following steps were monitored by SEIRAS (Fig.5.8). Subsequently, the surface was washed thoroughly with water free DMSO and once with milliQ water. In the second step, N α ,N α -bis(carboxymethyl)-L-lysine (ANTA) (75 mM in 0.5 M K₂CO₃ aqueous solution) was bound to TSP via peptide bond formation in a nucleophilic substitution reaction (Fig. 5.8, B) during 1 h exposure. The surface was washed with milliQ water again. Finally, nickel ions were bound to the carboxylate groups of the novel linker molecule on the surface which form metal-chelate complexes, as depicted in Fig.5.8, C. Therefore, aqueous 50 mM NiSO₄ was

applied to the surface for 1 h. The procedure was performed at 20 °C. The preparation procedure was monitored with the following settings:

For the preparation of the TSP monolayer:

1. Background spectrum with 1024 scans,
2. 15 times 0.1 min each with 10 s retardation,
3. 15 times 0.9 min each with 60 s retardation.

For the preparation of the ANTA or Ni-NTA monolayer:

1. Background spectrum with 1024 scans,
2. 15 times 0.1 min each with 10 s retardation,
3. 15 times 0.9 min each with 60 s retardation,
4. 8 times 1024 scans each with 300 s retardation.

4.5.2.2 Nanodisc immobilization

The nanodiscs were immobilized using the chelate complex formation of the nanodiscs oligo-histidine tag and the Ni-NTA SAM modified SEIRAS prism surface (Fig.4.3).

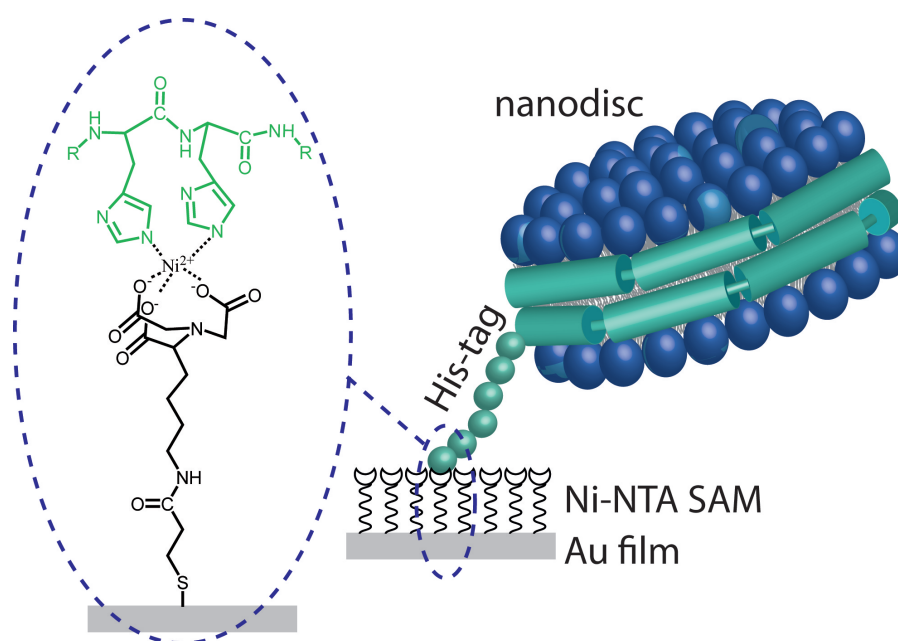


Figure 4.3: Scheme of a nanodisc immobilized to a Ni-NTA SAM (right) and the chemical structure of the Ni-NTA histidine-motive complex (left).

4. Methods

Therefore, the modified SEIRAS prism surface (section 4.5.2.1) was exposed to 50 mM NaPi buffer pH 7.4 to measure the background by 1024 scans. Instantly, the nanodiscs (MembraneMaxTM HN protein expression kit) were added to a final concentration of approximately 1 μ M and measured successively by default:

1. 15 times 0.1 min each with 10 s retardation,
2. 15 times 0.9 min each with 60 s retardation,
3. 8 – 10 times 1024 scans each with 300 s retardation,
4. 10 – 20 times 1024 scans each with 1800 s retardation.

After the measurement, the nanodisc solution remained on top of the surface over night.

4.5.3 Expression and folding of bR

For recombinant expression of bR on the SEIRAS sample surface, the cell-free protein synthesis system MembraneMaxTM HN was applied. After binding the nanodiscs over night (section 4.5.2.2) and washing the surface with 50 mM NaPi buffer (pH 7.4), a background spectrum of the nanodisc layer was taken with 200 μ L buffer atop by 1024 scans. Promptly, 50 μ L reaction mix of the cell-free protein expression system was added including all-*trans* retinal but without the template DNA. The sample was measured as follows until no changes were observed between the spectra:

1. 15 times 0.1 min each with 10 s retardation,
2. 15 times 0.9 min each with 60 s retardation,
3. 8 – 10 times 1024 scans each with 300 s retardation.

Again, a background spectrum was taken with subsequent addition of 50 μ L feeding mix containing approximately 1 μ g DNA (here: pEXP5-CT/bR) to initiate the transcription and translation cycle of the protein biosynthesis. The measurement was performed over night, which was usually 10 to 12 hours at room temperature and no stirring:

1. 15 times 0.1 min each with 10 s retardation,
2. 15 times 0.9 min each with 60 s retardation,
3. 8 – 10 times 1024 scans each with 300 s retardation,
4. 10 – 20 times 1024 scans each with 1800 s retardation.

4.5.4 Probing the functionality of bR in the SEIRAS folding experiment

SEIRA difference spectrum of bR, cell-free expressed into surface tethered nanodiscs

The light-induced absorption difference spectrum of expressed bR was investigated with the intention to probe the expression and functionality of the protein. Therefore, after the procedure described in section 4.5.3, the supernatant atop the sample film was exchanged by 50 mM NaPi, pH 7.4. Subsequently, a light-induced absorption difference spectroscopic measurement was executed. Either a 530 nm light-emitting diode (LED) or 532 nm neodymium-doped yttrium aluminum garnet (Nd:YAG) continuous wave laser (2 mJ/cm^2) was used to collect the light-induced difference absorption spectrum of the sample. Under continuous illumination using a strong light source like a LED or laser, the maximal number of bR molecules should be excited continuously to accumulate the intermediates N and M, which have longer life times compared to other states. In contrast, the ground state is dominated at darkness. The measurement was processed as follows:

1. Background spectrum with 1024 scans with subsequent background subtraction (i.e. zero-line as starting point for the measurement)
2. Exposure of the sample approximately 1 min to darkness with subsequent 1024 scan measurement under darkness (= dark-state favored spectrum)
3. Exposure of the sample approximately 1 min to light with subsequent 1024 scan measurement under light (= light-state favored spectrum)
4. Repeat 1–3 10 to 20 times

The dark-state spectrum was subtracted from the light-state spectrum, resulting in the light-dark difference absorption spectrum, followed by averaging all of the 10 to 20 difference spectra to reduce the noise level. A difference spectrum, that can be expected for functional bR, is depicted in figure 4.4. The figure depicts an light-induced ATR-FTIR difference spectrum of bR in purple membrane, measured using a comparable light source as done for the difference SEIRAS experiments. Because of the lower signal intensities in SEIRA spectra compared to a ATR-FTIR spectra, much lower signals and a smaller S/N ratio are expected for the resulting difference spectrum. Hence, only bands are assigned in figure 4.4, which are supposed to be visible even under the

4. Methods

described signal quality. The significant spectral region in FTIR light–dark difference spectra for retinal proteins is usually 1800 to 1000 cm^{-1} . However, here the spectral region $< 1200 \text{ cm}^{-1}$ is omitted due to the spectral limitations of the expected SEIRA spectra. The difference spectrum in figure 4.4 shows features of the M–intermediate and the N–intermediate of bR. Significant bands are the C=C stretching vibration of all–*trans* retinal in the unphotolysed state at 1527 cm^{-1} [120] and 13–*cis* retinal of the M–intermediate at 1554 and 1565 cm^{-1} [27]. The bands at 1302 and 1402 cm^{-1} were assigned to the C-H in-plane bending and N-H in-plane bending vibration, respectively, of the Schiff base for the N–intermediate [120]. The band at 1761 cm^{-1} is representative for the M–intermediate’s combination mode of C=O stretching and in-plane O-H bending of the protonated carboxylic acid of aspartate 85 [120]. The amide I mode is represented by the bands at 1692, 1670 and 1649 cm^{-1} for the N–intermediate and 1658 for the M–intermediate [27]. These bands represent changes of bR and the retinal backbone, which can be solely observed for functional bR. Further information regarding the band assignment can be found in [27, 120, 121].

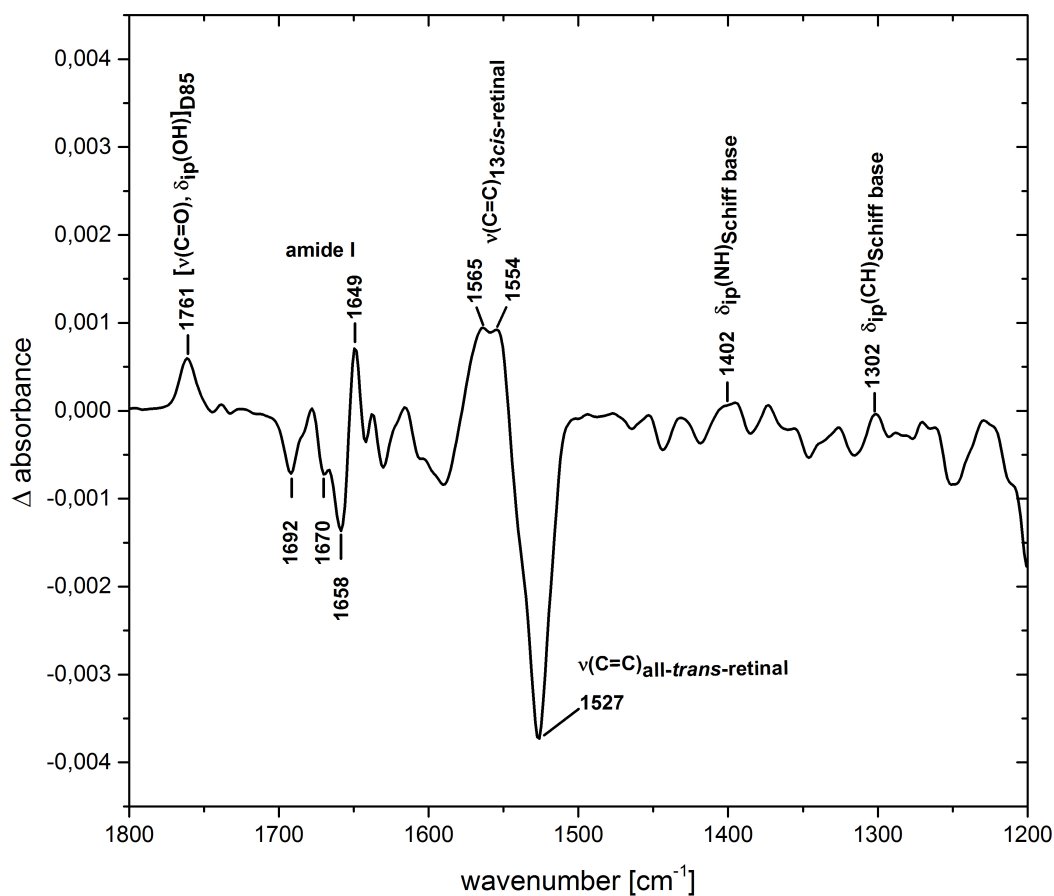


Figure 4.4: Light-induced FTIR difference spectrum of bR in purple membrane when dried onto a Silicon crystal and measured in ATR configuration. The light-induced spectra were recorded under illumination at 530 nm by an LED (data by courtesy of Dr. Sven T. Stripp, FU Berlin, Germany). For the band assignment see [27, 120].

Several different approaches were performed to improve the described SEIRA difference spectroscopic measurement in order to identify the photocycle activity of bR after expression and folding. Therefore, the described measurement was repeated several times, each time, with one of the following modifications. First, to increase the transient population of bR's N-intermediate state, its photocycle was slowed down by exposing the sample to a buffer with basic pH. In detail, immediately after the IR absorption kinetics of the bR folding experiment reached steady state, the supernatant above the sample was exchanged by 50 mM NaPi, pH 7.4, to check the stability of the IR absorption signal. Subsequently, this buffer was exchanged by 50 mM MES, 4 M NaCl at pH 10. The second approach was intended to reduce the signal intensities of the water bands, which can hide signals of interest. Therefore, after the IR absorption kinetics were saturated, the supernatant above the sample

4. Methods

was removed and the remaining sample film dried out at room temperature. Third, the bR variant bRD96N was expressed instead of bR. The mutation D96N leads to an increased transient population of bR's M-intermediate state resulting in a slower photocycle as compared to bR. Fourth, the third approach was repeated. But additionally, after the expression took place, the pH was raised by successively replacing the supernatant atop the sample by

1. 100 mM NaPi, pH 7.4,
2. 40 mM TrisHCl, 100 mM NaCl, pH 8.0,
3. 40 mM TrisHCl, 100 mM NaCl, pH 8.2,
4. 40 mM TrisHCl, 100 mM NaCl, pH 8.4,
5. 40 mM TrisHCl, 100 mM NaCl, pH 8.6.

Thereafter, for a Resonance Raman spectroscopy [122] measurement, the SEIRA silicon crystal was transferred into the Horiba LABRAM spectrometer using the Krypton ion laser INNOVA90c (568 nm, 10 mW) including the software LabSpec.

Laser flash photolysis of bR, cell-free expressed into nanodiscs in batch

The functionality of cell-free expressed bR or bRD96N in batch mode can be approved by measuring their photocycles, which can be measured by flash photolysis [122] as the concentration of the protein and volume of the sample are both high enough for this method. Here, a self-constructed setup of an LKS.80 Laser Flash Photolysis Spectrometer including the LKS software were used. First, bR or bRD96N were expressed into nanodiscs (InvitrogenTM) by the MembraneMaxTM *HN* protein expression kit. Subsequently, the sample was centrifuged at 22000 x g for 1 min at 4 °C and the photocycle of the supernatant was measured by laser flash photolysis at representative wavelengths in the UV/Vis range. The sample was excited by a short pulse from a solid-state laser (Nd:YAG, 10 ns laser pulse at 532 nm, energy density of 3 mJ/cm², one pulse every 10 s). The flash photolysis experiments were performed on two time scales, with the faster time range (< 300 μs) recorded with the light source (xenon arc (Xe arc) lamp) in pulsed mode and the slower time scale (> 30 μs) recorded with the light source in continuous operation. Data were averaged on a quasi-logarithmic time-scale and merged to yield time traces

covering the time range from 500 ns to 10 s. Ten kinetic traces were averaged at each selected wavelength.

SEIRA difference spectroscopy on bR within nanodiscs, which was cell-free expressed in batch

After the bR sample was probed by laser flash photolysis (section 4.5.4), a SEIRA difference spectroscopy measurement was performed on that sample. In detail, a prepared Ni-NTA SAM (section 4.5.2.1) was covered by 50 mM NaPi, pH 7.4 for the background measurement. Thereafter, the sample was added with a final dilution of 1 : 5. After the SEIRA kinetics reached steady state, the SEIRA difference spectroscopic experiment was performed as described in section 4.5.4.

The SEIRA difference spectroscopy measurement was repeated several times, but with the following changes to prolong the photocycle of bR. Cell-free expressed bR in batch mode was measured at basic pH. Therefore, after immobilization to the surface, the buffer was exchanged by 50 mM MES, 4 M NaCl, pH 10. In a further measurement, batch cell-free expressed bRD96N was probed, which is a slower variant of the prior measured bR. Finally, the measurement for bRD96N was repeated, but additionally after immobilization of the sample, the buffer was exchanged by 40 mM TrisHCl, 100 mM NaCl, pH 8. Subsequently, the sample monolayer was probed by the 532 nm Nd:YAG continuous wave laser. Thereafter the buffer was exchanged by 10 mM Fe(III)Cl₃ * 6 H₂O in 40 mM TrisHCl, 100 mM NaCl, pH 5.8 [123] and the measurement was repeated.

Light-induced IR difference absorption spectroscopy on bR within nanodiscs by ATR FTIR

BR was expressed into nanodiscs using the MembraneMaxTM HN kit according to the standard protocol (section 4.4.1) with a final volume of 500 μ L. Thereafter the sample was centrifuged at 22000 x g at 4 °C for 1 min. The supernatant was analyzed on photocycle activity by laser flash photolysis as described before. Subsequently, 200 μ L were maximal concentrated (20 μ L) using a Amicon[®] Ultra-0.5 Centrifugal Filter Devices (10 kDa MWCO) centrifuging in several steps at 14000 x g at 4 °C.

For the ATR-FTIR measurement, a Vertex 80v FTIR spectrometer including a DuraSamplIRIITM ATR optic was employed. The spectrometer uses the software OPUS for data treatment. First, 3 μ L of the not concentrated

4. Methods

sample were dried onto the ATR–Si–crystal and the light–induced absorption difference spectrum monitored using a 530 nm LED to detect the photocycle. Secondly, the dried film was hydrated by 3 μL of not concentrated sample and measured again. Third, both measurements were repeated but for the concentrated sample.

4.5.5 BR folding experiment without immobilized nanodiscs

As a control, the bR folding experiment of section 4.5.3 was repeated under identical conditions but without nanodisc monolayer immobilized to the SEIRA prism surface.

4.5.6 Impact of the co–factor retinal on the bR folding process

To probe the impact of the co–factor retinal on the bR folding process, two different approaches were performed. The first one was performed under identical conditions as described in section 4.5.3, but without addition of all–*trans* retinal. This experiment was repeated but with an immediate retinal supply when the IR absorption kinetics started to saturate.

In the second approach, the experiment in section 4.5.3 was modified as follows. The immobilized nanodiscs were incubated with 20 μM final concentration all–*trans* retinal (in 40 mM TrisHCl, 100 mM NaCl, pH 8). After the IR absorption kinetics were saturated, the surface was washed three times with 200 μL of the same buffer. Subsequently, the cell–free bR expression was performed, but without any additional retinal supply.

4.5.7 Cell–free expression of EmGFP

The SEIRA sample surface and the nanodisc immobilization were performed analogous to section 4.5.2. For cell–free EmGFP expression, the PURExpress[®] *In Vitro* Protein Synthesis Kit E6800S was employed (section 4.4.2). The surface with immobilized nanodiscs was covered with 150 μL 100 mM NaPi, pH 7.4. Thereafter, master mix solution was added, here composed of 20 μL solution A and 14.5 μL solution B. After 1 h incubation, transcription and translation was induced by adding 10 μL pRSET–EmGFP (in 10 mM Tris–Cl, pH 8.5). The sample was probed by SEIRAS as described in section 4.5.3 over night. The next day, the supernatant was removed from the surface and analyzed by the spectrofluorometer FluoroMax-3[®] including the software LabSpec at 470 nm excitation. For data representation Origin9.0 was used.

4.5.8 Initial experiments on folding of other microbial rhodopsins

In initial experiments on folding of other α -helical membrane proteins, *HsSRI*, *HsSRII* and *CrChR2* were expressed in the same manner as done for bR (section 4.5.3) using the respective templates. To ensure comparability, the identical experimental conditions were used except for the following changes. The nanodiscs were incubated with approximately 50 μM all-*trans* retinal final concentration in 50 mM NaPi, pH 7.3. After the IR absorption kinetics were saturated, the surface was washed three times with 200 μL of the same buffer and the procedure started by adding the reaction mix.

4.5.9 SEIRA spectra processing

The broad detection range and sensitivity of the used photodetector benefits from the semiconducting properties of mercury cadmium telluride (HgCdTe). However, the signal output of such photodetectors is rather small when it competes with thermal excitation of current carriers within the material [124,125]. To reduce these thermal effects and to operate the detector, the system must be cooled down to ≈ 100 K [125], which was realized by liquid nitrogen before the measurement started. But, during the duration of the measurement the liquid nitrogen evaporated and the detector heated up again. This led to non-linear baseline shifts between the IR absorption spectra due to inhomogeneous detectivity for different frequencies caused by the thermal effects mentioned above [125]. This shift was more significant for measurements lasting several hours. Additionally, the complex nature of the SEIRA sample film (see paragraph about the SEIRAS EM mechanism in section 2.3.4) is considered to influence the baseline shift. Thus, after background subtraction, the observed SEIRA spectra had to be baseline corrected.

Due to the nature of the sample film, for some regions of the spectra, hardly no IR absorption bands were expected as compared to finger print regions. Hence, these regions were considered to represent the approximate baseline of each spectrum. Changes in that regions originate almost exclusively from the baseline shift mentioned before. These regions were located at around 2450, 1900 and 1475 cm^{-1} . The exact spectral region is described at each individual spectrum within the results section. They were used as reference points. Between these points (approximately 2450 and 1475 cm^{-1}) the shift is considered to behave almost linear.

The baseline correction had to be applied individually for each spectrum because of the non-reproducible character of the shift. Therefore, the data

4. Methods

points of at least two of the mentioned regions were linearly fitted. The resulting line fit was subtracted from the respective spectrum. It has to be noted, that this approximation was limited to the applied region because of the overall non-linearity of the baseline shift.

Because of water and water vapor interference, the second derivatives of the spectra were used for secondary structure analysis of bands like the amide I vibrational band. Instead of band fitting by for example Voigt profiles, comparing second derivatives of the spectra was supposed to resolve overlapping features of the band in a more distinct way but also face the difficulty of evaluating the interference of water vapor bands [126]. The second derivatives were returned by employing a Savitzky–Golay filter with polynomial order two and five data points window size, if not stated otherwise. For calculations and representation the software Origin9.0 was employed.

Chapter 5

Results and Discussion

5.1 Cell-free bR expression into nanodiscs

Two cell-free protein expression systems and different types of nanodiscs (section 4.4.3 and 4.4.4) were used. The following results are exemplary and representative for all bR variants described in this thesis.

5.1.1 Commercial nanodiscs

For cell-free bR expression, the MembraneMaxTM *HN* system including the provided nanodiscs [109] was preferentially used because of the documented excellent performance for bR synthesis, as the system is designed to express various membrane proteins but is optimized for bR expression. Under optimal conditions (e.g. the maximum vitality of the expression system, a sufficient amount of intact nanodiscs, optimal temperature, mixing etc.) it is supposed to result in nanodiscs of which approximately 80 to 90 % are filled with functional bR [72]. For all SEIRAS experiments on folding, which are documented in this thesis, the commercial nanodiscs delivered by this protein expression kit were used. These nanodiscs were also utilized for the cell-free bR synthesis by the PURExpress[®] *In Vitro* Protein Synthesis kit E6800S.

To illustrate the expression results for both systems, bR was cell-free expressed as described in section 4.4.3. The UV/Vis absorption of the expression products were monitored (Fig. 5.1). The expression success of bR is indicated by the appearance of an absorption peak at 553 to 568 nm due to the co-factor binding by functional bR, which further indicates the successful incorporation of correctly folded bR into the offered nanodiscs. Both systems show the expected absorption, although the PURExpress[®] system showed frequently almost 10-fold lower expression than the MembraneMaxTM *HN* system (see Fig. 5.1). For comparison, both systems were used synchronously.

According to Katzen *et al.* [72], the oligomerization state of bR results in

5. Results and Discussion

a shift of the UV/Vis absorption range. A monomer absorbs at 546 nm (dark adapted state) and 553 nm (light adapted state), whereas a trimer absorbs at 558 nm (dark adapted state) and 568 nm (light adapted state). The latter is demonstrated by the spectrum of purple membranes from *H.salinarum* in figure 5.1 A, which contain predominantly a 2D lattice of trimeric bR [127]. The sample was prepared under light adaption and thus shows an absorption at 568 nm (Fig. 5.1). Although the absorption range is rather broad, cell-free expressed bR samples show an absorption at approximately 553 nm, which suggests that the majority of bR molecules are monomeric. This assumption agrees with the literature [72].

The SEIRAS experiments are intended to monitor folding when the membrane protein is leaving the ribosomal tunnel. Hence, it is mandatory, that bR folds co-translationally. Dale *et al.* [53] assume, that the N-terminus of bacterioopsin (BO) inserts co-translationally into a bilayer. This is also indicated by the cell-free expression of bR using the PURExpress[®] *In Vitro* Protein Synthesis kit E6800S. According to correspondence with the manufacturer, the kit contains just the minimum components necessary for cell-free protein expression without any chaperones or additional molecules which can assist during post-translational folding. Additionally, the used nanodiscs (MembraneMax[™] *HN* protein expression kit) did not contain translocons. Thus, the successful bR expression implicates, that BO inserts co-translationally. Furthermore, the knowledge about all components of the PURExpress[®] system represents an opportunity to investigate the folding pathway of bR including potential helper proteins in more detail when probed by SEIRAS.

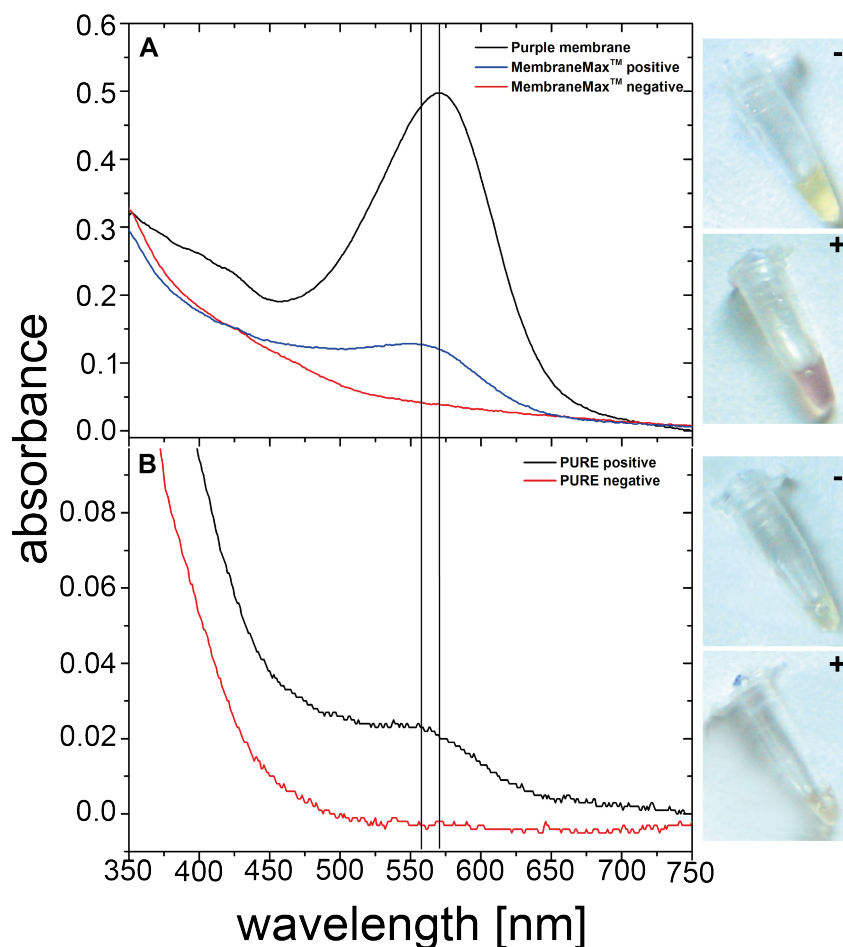


Figure 5.1: UV/Vis absorption spectra of cell-free expressed bR from pEXP5-CT/bR into commercial nanodiscs (MembraneMaxTM HN protein expression kit), which are 10 nm in diameter, 5 nm in height and containing DMPC. Cell-free protein expression had been performed by A) the MembraneMaxTM HN protein expression kit and B) the PURExpress[®] *In Vitro* Protein Synthesis kit E6800S. A) contains the UV/Vis spectrum of purple membrane from *H.salinarum* for comparison. A positive sample represents the cell-free expression mixture with template DNA whereas the negative sample represents the identical mix without template. The pictures depict the respective expression products in the test tube. The figure was prepared using Origin9.0 and Adobe Illustrator CS5.

Complementary to the UV/Vis spectra in figure 5.1 A, the bR expression samples were purified by Ni-NTA affinity chromatography and subsequently analyzed by SDS-PAGE (section 4.4.3). As a negative control, an identical expression reaction without template DNA was used. The SDS-PAGE in figure 5.2 shows the expression results for both samples. The sample with DNA was expected to show two bands, one for the MSP and one for bR, whereas the sample without DNA should solely show the band for the MSP. Since bR did

5. Results and Discussion

not possess an histidine-tag, it could not bind to the Ni-NTA affinity resin. Thus, only bR incorporated in nanodisc was purified by that method. The MSP was not specifically described by the manufacturer, but should migrate at 28 kDa [109]. According to the online tool ProtParam the bR construct has a molecular weight of 26.9 kDa but migrates around 21 kDa [109].

The SDS-PAGE in figure 5.2 a) verified the co-elution of bR with the MSP in agreement with the literature [109], whereas for the negative control just the MSP band was observed (Fig. 5.2 b). These results in combination with the UV/Vis data in figure 5.1 confirmed the successful incorporation of functional bR into nanodiscs when using the MembraneMaxTM *HN* protein expression kit.

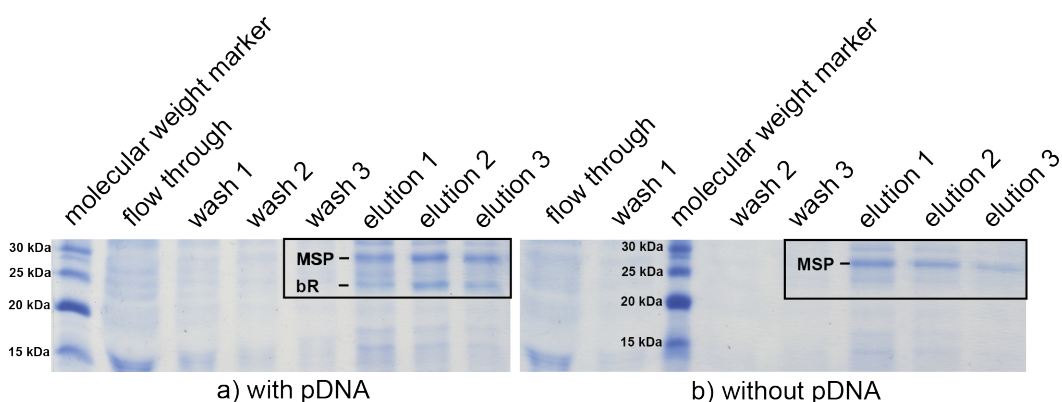


Figure 5.2: SDS-PAGEs, showing the results of two identically processed cell-free membrane protein expression experiments using the MembraneMaxTM *HN* protein expression kit a) with template (pEXP5-CT/bR) and b) without template. Both samples were purified by standard histidine-tag Ni-NTA affinity chromatography. The figure was prepared using Adobe Illustrator CS5.

As further verification of functional bR, the photocycle activity was approved by Laser flash photolysis (section 5.3.4).

5.1.2 Nanodisc assembled by MSP1D1 and DMPC

To expand the toolbox for functional expression of different membrane proteins, nanodiscs can be customized with regard to the needs of the membrane protein. As a first approach in order to modulate the size, nanodiscs assembled by an alternative scaffold protein (i.e. MSP1D1) and DMPC were prepared. This nanodisc type was chosen initially, because the dimension and chemical environment were comparable to the commercial nanodiscs, which were used for the SEIRAS experiments on bR folding in section 5.3 [101, 109]. Based on this results, future improvements can be executed, for example by adjusting a more favorable lipid composition or MSP.

Nanodiscs assembled from MSP1D1 and DMPC were prepared as described in section 4.3.2. Initially, MSP1D1 was heterologously expressed, purified and analyzed by SDS-PAGE, which is depicted in figure 5.3. The rectangular frame marks the bands of interest. As calculated by the ExPASy ProtParam online tool, MSP1D1 had a molecular weight of 24.6 kDa (see appendix B, Tab. B.1), which correlated with the prominent bands in figure 5.3 in the rectangular frame.

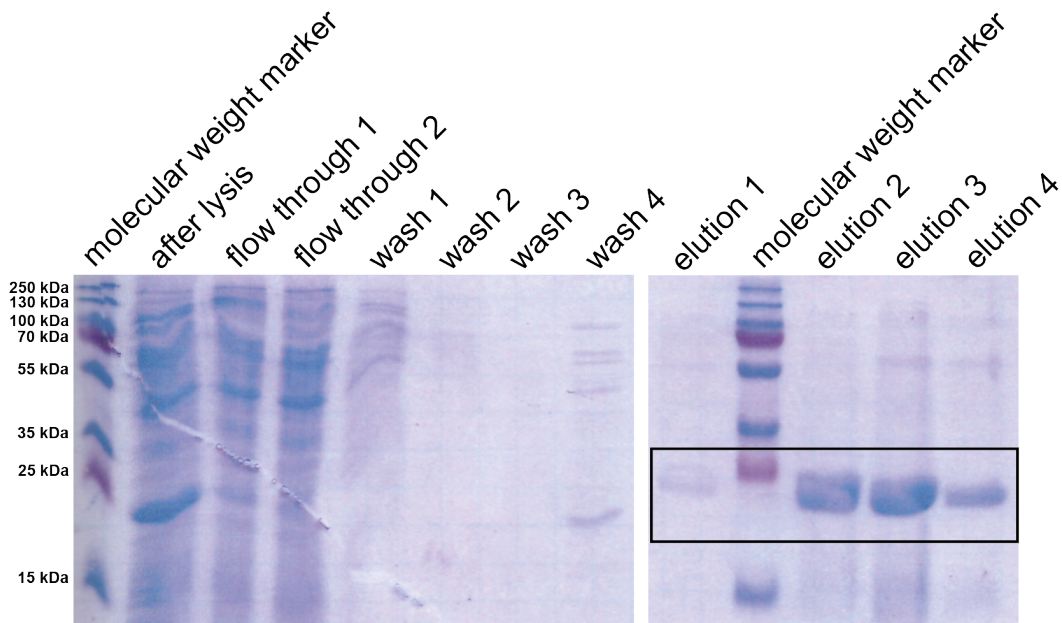


Figure 5.3: SDS-PAGE monitoring the purification of MSP1D1. The black rectangular frame marks the fractions containing purified MSP1D1 with 24.6 kDa. The figure was prepared using Adobe Illustrator CS5.

The successfully purified MSP1D1 was used to assemble the nanodisc with DMPC. A portion of the assembly product was analyzed by SEC (see Fig. 5.4). Using a Superdex 200 10/300 GL column, nanodiscs elute at approximately 12 mL, which was visible by a prominent peak. The smaller peak at around 8 mL represented the void volume. The shoulder around 10 mL was assigned to nanodiscs, which probably stick together by their His-tag. As removal of the His-tag leads to one peak in the chromatogram without this shoulder (personal communication with Luis Möckel and Sameer Singh, ICS-6, Research Centre Juelich GmbH, Germany). The results were in agreement with the literature [57, 101] and represented successfully assembled nanodiscs.

5. Results and Discussion

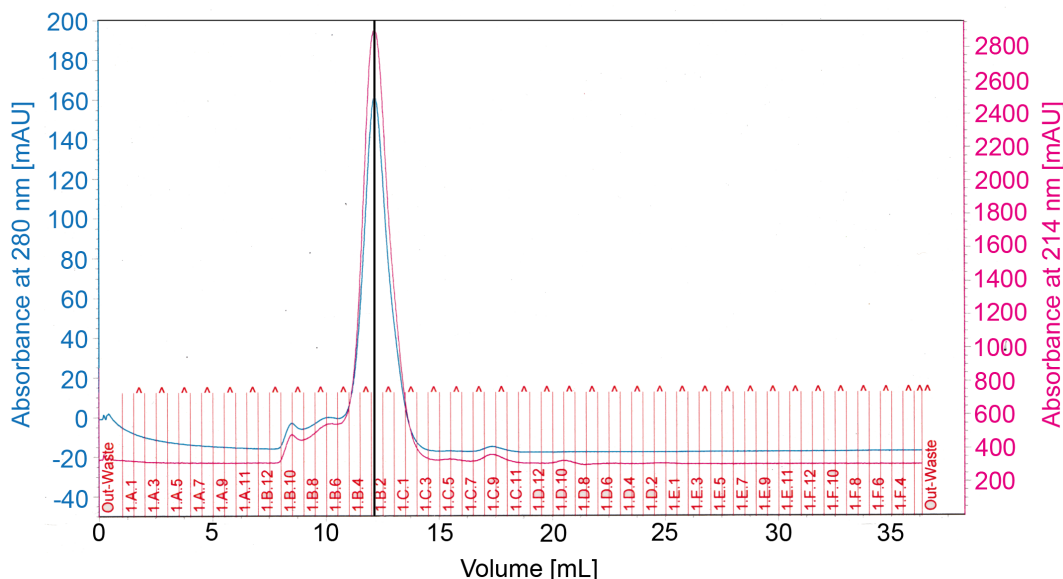


Figure 5.4: SEC of nanodiscs assembled from MSP1D1 and DMPC. Elution of nanodiscs was observable at approximately 12 mL (labeled by the black line). The figure was prepared using the software UNICORNTM 6.1.

These nanodiscs were used for the cell-free expression of bR in combination with the MembraneMaxTM *HN* protein expression kit (section 4.4.4). After purification of the sample by Ni-NTA affinity chromatography, the reddish eluate was analyzed by SEC (section 4.4.4). During elution, the absorption at 560 nm representing functional bR [128–130], and 280 nm, representing the total protein content (i.e. MSP1D1, bR etc.) were recorded (Fig. 5.5). The bR regions, which were not buried in the nanodisc bilayer, were negligible small in order to change the elution properties significantly. Thus, the fraction of interest was also expected at approximately 12 mL as for empty nanodiscs (Fig. 5.4) and was supposed to show additionally absorption at 560 nm. Figure 5.5 shows a bR containing fraction at 7.91 mL, which was the void volume of the applied SEC column and represents for example big aggregates of bR within nanodiscs. The elution of fractions 10, 11 and 12 were comparable to the SEC of empty nanodiscs in figure 5.4. Furthermore, the absorption at 560 nm strongly indicates functional bR for these fractions. Hence, analogously to the assignment of figure 5.4, the peak at 11.13 mL contained predominantly nanodiscs with and without incorporated bR, which were adhesive to each other. Fraction 12 represented predominantly the expected nanodisc/bR complexes and empty nanodiscs. Peaks eluting later than 13 mL were assigned to impurities.

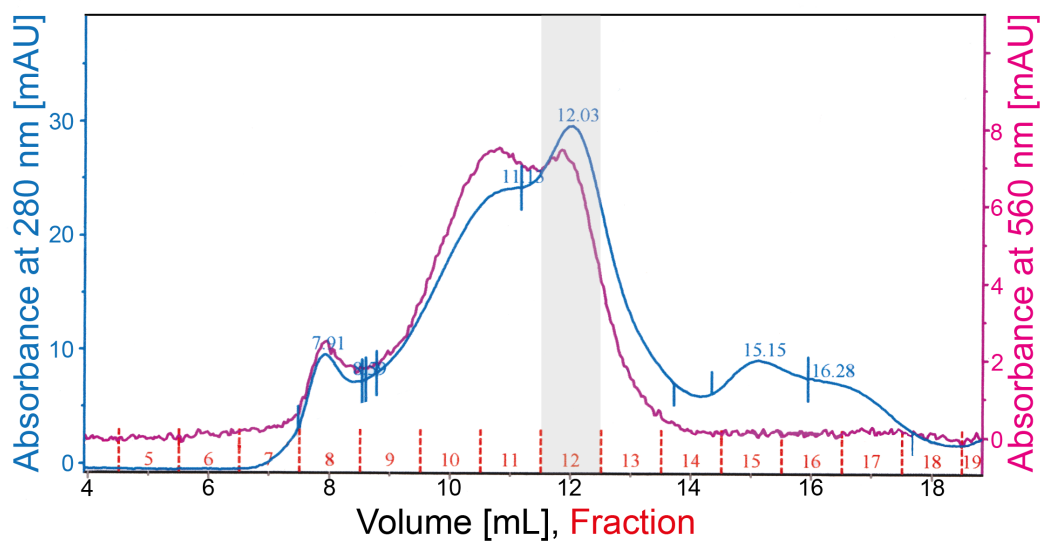


Figure 5.5: SEC of nanodiscs assembled by MSP1D1 and DMPC containing cell-free expressed bR. The complexes of nanodiscs with incorporated bR were pre-purified by histidine-tag Ni-NTA affinity chromatography. The figure was prepared using the software UNICORN™ 6.1.

Fractions 8 to 15 were further analyzed by SDS-PAGE (Fig. 5.6). The region of interest in figure 5.6 is highlighted by a black rectangular frame. The upper band was assigned to MSP1D1 whereas the lower band was assigned to bR.

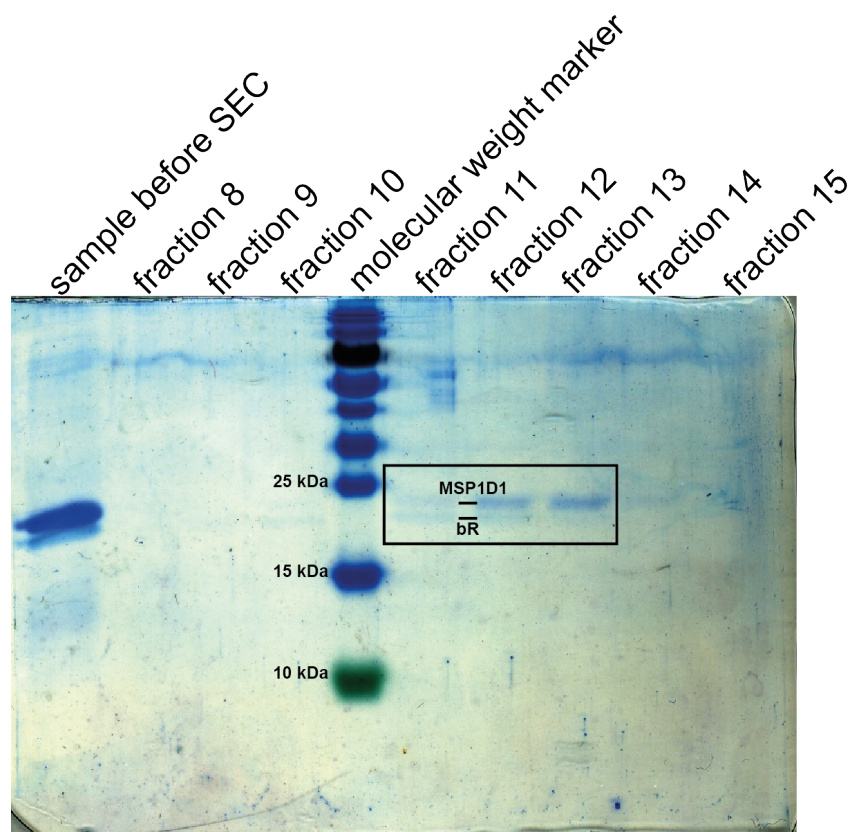


Figure 5.6: SDS-PAGE of SEC fractions depicted in figure 5.5 representing purified nanodiscs assembled by MSP1D1 and DMPC containing cell-free expressed bR. The black rectangular frame highlights the region of interest in which MSP1D1 and bR are expected to be located. The figure was prepared using Adobe Illustrator CS5.

Fraction 12 was analyzed by negative staining and electron microscopy, executed by Prof. Holger Stark (Max Planck Institute for Biophysical Chemistry Göttingen, Germany), which is depicted in figure 5.7. The image shows disc-shaped species with a uniform size of approximately 10 nm in diameter, which was expected for the used nanodiscs. Subsequent experiments with this sample in order to image nanodisc/bR complexes by 3D-cryo-TEM could not visualize bR within the nanodiscs due to resolution limitations of the technique. Nevertheless, the image approved the presence of nanodiscs in fraction 12 depicted in figure 5.5.

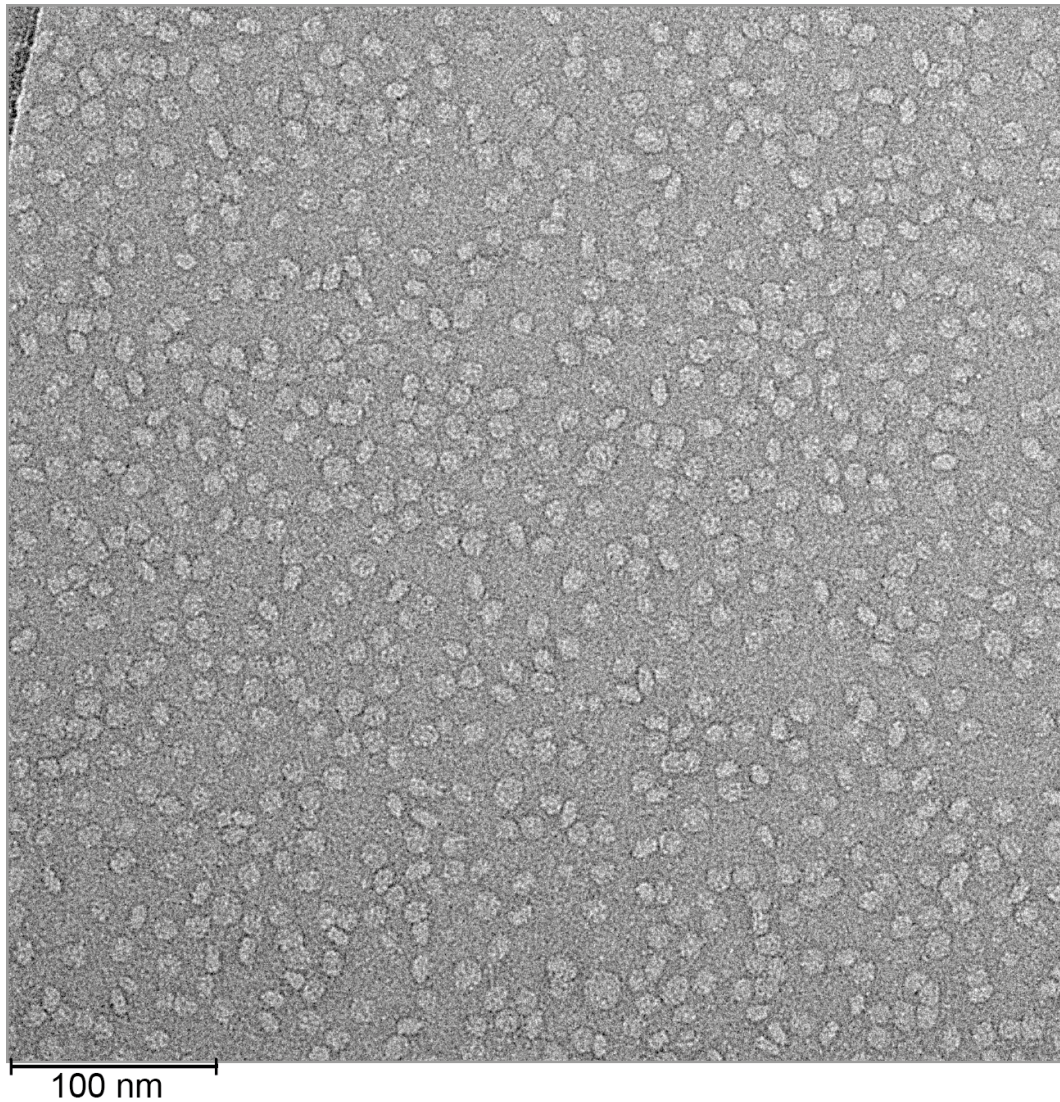


Figure 5.7: Electron microscopic image of negative stained fraction 12 from the SEC experiment depicted in figure 5.5 with 88.000 fold magnification. In collaboration with Prof. Holger Stark, Max-Planck-Institute of Biophysical Chemistry Goettingen, Germany.

In conclusion, these results indicated the presence of nanodiscs and purple bR within the same SEC fractions (i.e. predominantly 11 and 12), suggesting that the protein was successfully incorporated and folded into nanodiscs as well as retinal binding when expressed in a cell-free approach.

5.2 Cell-free expression of other microbial rhodopsins into nanodiscs

The three α -helical membrane proteins *HsSRI*, *HsSRII* and *CrChR2* were cell-free expressed as described in section 4.4.5. After incubation at 37 °C no color

change of the samples was observed. The purification via histidine-tag Ni-NTA affinity chromatography and analysis by standard 15 % SDS-PAGE could not verify the cell-free expression of either one of the proteins.

5.3 SEIRAS experiments on membrane protein folding *in situ*

5.3.1 Spectral examination of the Ni-NTA SAM surface preparation

The gold surface of the Si-prism was functionalized by a Ni-NTA SAM, which is described in section 4.5.2.1. The assembly was performed in three steps *in situ* and monitored by SEIRAS (Fig. 5.8). The background subtracted SEIRA spectra after saturation of the absorption signal in figure 5.8 are examples, that were expected after each reaction (A-C) is finished. At first, a TSP SAM was formed by breaking the disulfide bond of the homobifunctional DTSP (reaction equation on the right next to SEIRA spectrum A). The SEIRA spectrum represents surface bound TSP after saturation of the IR absorption, with vibrations at 1810 cm^{-1} for the C=O stretching mode of the ester group and at 1780 and 1739 cm^{-1} for the asymmetric and symmetric stretching of the carbonyl groups of the succinimidyl ring. During the second step, this layer was activated with ANTA by a nucleophilic substitution of the amino group of ANTA with the ester carbonyl group of TSP (reaction equation B). The SEIRA spectrum B of the nitrilotriacetic acid (NTA) monolayer shows negative vibrations at 1810 , 1780 and 1736 cm^{-1} for the leaving succinimidyl ester ring and positive peaks at 1657 cm^{-1} for C=O stretching of the peptide bond and 1405 cm^{-1} for symmetric stretching of the three deprotonated carboxylate groups. The absorption band at 1583 cm^{-1} was assigned to C-N stretching and N-H bending of the peptide bond. Finally, reaction equation C shows the Nickel ion chelation. The SEIRA spectrum of the NTA monolayer changed by the Nickel chelation. A negative signal appeared at 1657 cm^{-1} and in the regime around 3400 cm^{-1} (see the gray shaded area in appendix Fig. A.1) assigned to desorption of water caused by Nickel ion adsorption (i.e. binding). The bands at 1570 cm^{-1} were assigned to asymmetric and at 1432 and 1415 cm^{-1} to symmetric stretching vibrations of the carboxylate groups. Regions below 1400 cm^{-1} remain non-significant caused by high signal to noise ratio due to the high absorption of the silicon prism (see appendix Fig.A.2)

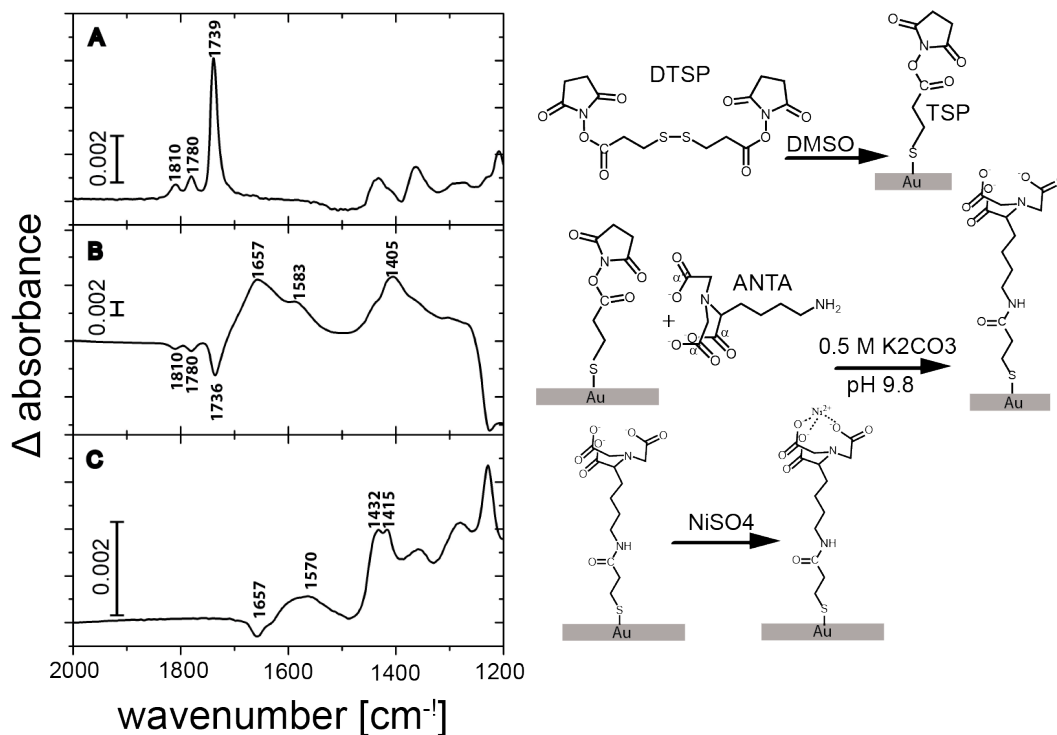


Figure 5.8: Formation of the Ni-NTA SAM on the nanostructured gold film in three steps (A–C) with the reaction equation on the right next to the respective background subtracted SEIRA spectrum after saturation of the absorption signal. (A) TSP SAM formation. (B) NTA monolayer formation. (C) Nickel ion chelation. The figure was prepared using Origin9.0, Adobe Illustrator CS5 and ChemSketch.

5.3.2 Nanodisc immobilization to the Ni-NTA SAM

Commercial nanodiscs

Nanodiscs (MembraneMaxTM *HN* protein expression kit) binding to the Ni-NTA SAM was monitored by SEIRAS. The binding process completed after about 44 min, indicated by characteristic bands (see Fig. 5.9).

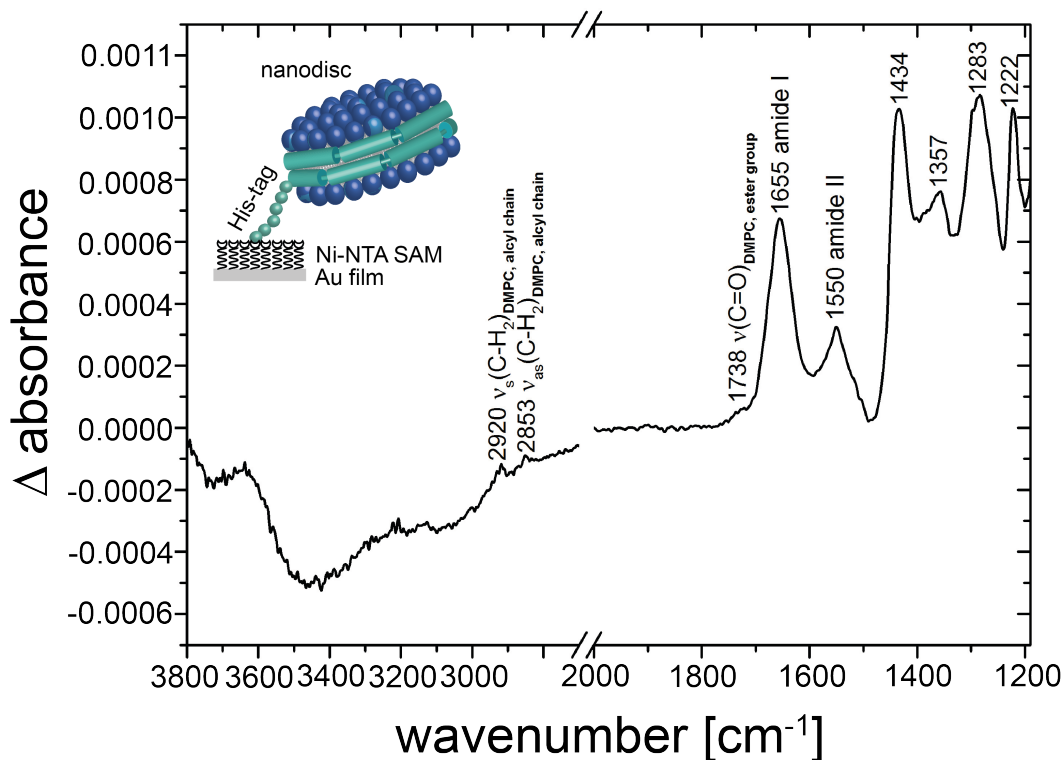


Figure 5.9: Illustration and background subtracted SEIRA spectrum of the nanodisc immobilization process after 44 min incubation time. Here, $1\ \mu\text{M}$ final concentration of nanodiscs (MembraneMaxTM *HN* protein expression kit) in 50 mM NaPi, pH 7.4 were incubated at room temperature overnight. The figure was prepared using Origin9.0 and Adobe Illustrator CS5.

The absorption bands at 1655 and $1550\ \text{cm}^{-1}$ emerged synchronously during the incubation time and were assigned to amide I and II respectively. The amide modes belonged to the nanodiscs MSPs. These band positions were representative for α -helical structures [80]. Parallel to the adsorption process a broad desorption band appeared around $3500\ \text{cm}^{-1}$ and was interpreted as water desorption due to the replacement by the nanodiscs. Water desorption superimposes with the amide A band of the nanodiscs adsorption process, visible by the broad band at around $3200\ \text{cm}^{-1}$. The bands below $1490\ \text{cm}^{-1}$ were characteristic for His-tagged protein adsorption to the Ni-NTA SAM and were observed regardless of which protein binds. The shoulder around $1738\ \text{cm}^{-1}$ was assigned to the C=O stretching mode of the DMPC ester group, which was the lipid component of the nanodiscs. Furthermore, the band at $2853\ \text{cm}^{-1}$ was assigned to asymmetric CH_2 stretching and at $2920\ \text{cm}^{-1}$ to symmetric CH_2 stretching vibrations of the lipids acyl chains.

It appeared, that the band for the C=O stretching vibration of the DMPC lipids was significantly lower in intensity as compared to the amide I band that

was mainly C=O stretching of the peptide bond. This was due to the surface selection rule applying in SEIRAS. The vibrations with a dipole moment perpendicular to the surface were more enhanced by the electromagnetic field and therefore appeared in the spectra with higher intensities (Fig. 5.10). In a nanodisc the dipole moment of the C=O vibration of the DMPC ester group and the one of the α -helical MSP were roughly perpendicular to each other (for details see Fig. 5.10). Thus, information about the orientation of the nanodisc towards the gold surface was obtained. Given the correct band positions of the amide I and II mode for an α -helical protein conformation, the average orientation of the nanodiscs was estimated from the amide I/II ratio and from the $\nu_{as}(\text{CH}_2)$ and $\nu_s(\text{CH}_2)$ at around 2900 cm^{-1} , as done by Zaitseva *et al.* [131]. They calculated an angle of roughly 24° ($\pm 10^\circ$) between the adjacent gold film and the surface tethered nanodiscs. Here, this angle was assumed to be higher with regard to a higher amide I/II ratio compared to the reported one. However, the obtained angle only reflected an average of all nanodiscs on the surface and overlapping water signals made a quantitative analysis impossible.

5. Results and Discussion

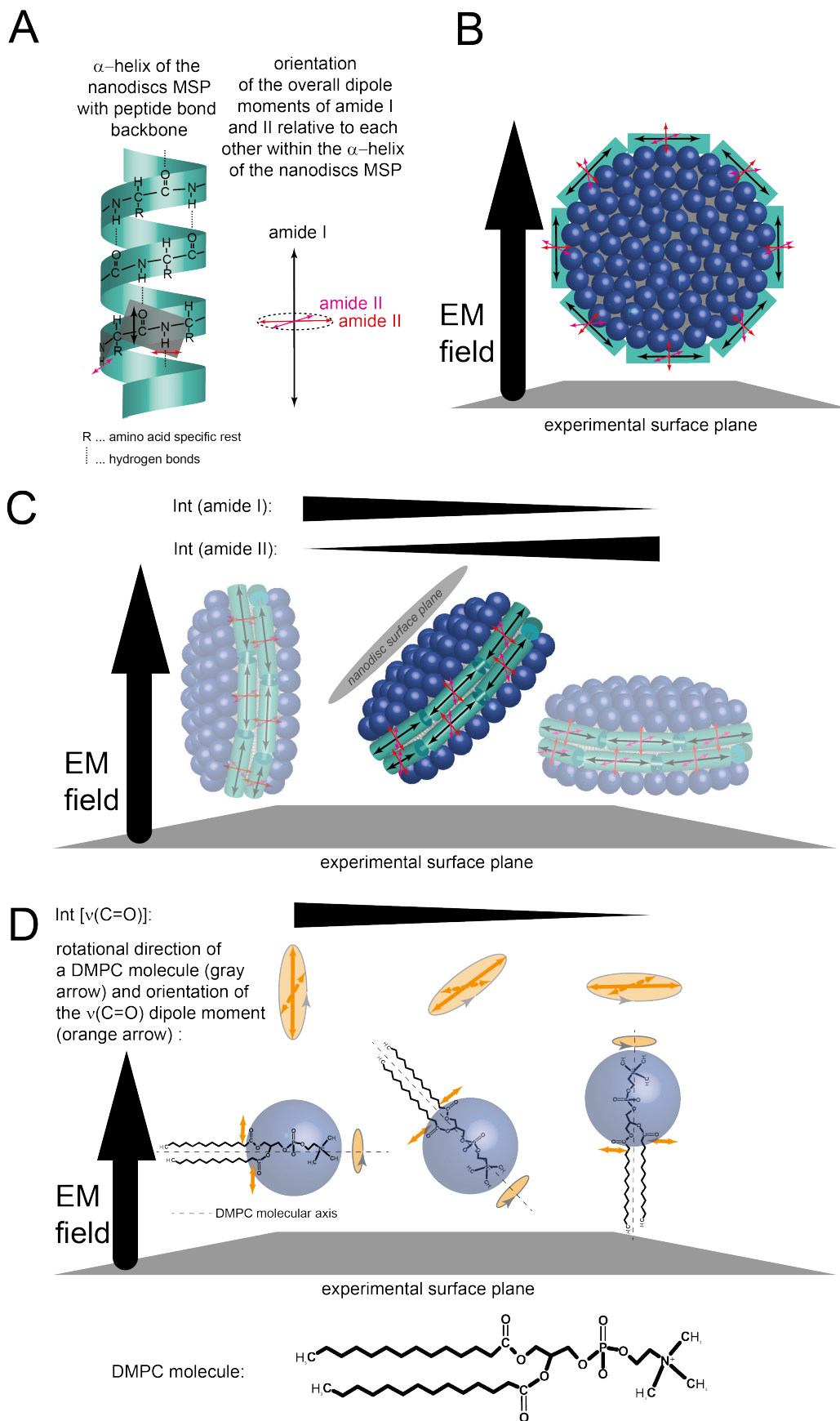


Figure 5.10 (*preceding page*): Orientation of the surface tethered nanodiscs, the orientation of their characteristic vibrational modes (i.e. amide I, II and $\nu(\text{C}=\text{O})$ of the lipids ester group) and the corresponding impact on the relative SEIRA signal intensities. A) left: Schematic drawing of an MSP's α -helix (green) with its peptide bond backbone. The peptide bond plane is highlighted by the gray shaded rectangle (touching all participating atoms) and is shown in front view and indicated in site view. The vibrational direction of the amide I mode is depicted as black double arrow. The amide II modes depend on the position of the amide group within the α -helix. They vibrate parallel to a plane, which is perpendicular to the amide I mode direction. Exemplary, the two amide II modes and their directions are highlighted by a red (peptide bond plane seen in front view) and pink (peptide bond plane seen from site view) double arrows. This relative orientation of the overall amide I and II dipole moments to each other is additionally depicted in A) right. The plane to which amide II parallelly vibrates is indicated by a black dashed lined ellipse. B) Cartoon of a nanodisc in on-plane view, which is oriented with its surface plane perpendicular towards the experimental sample plane (green: MSP, blue: lipids polar heads). Amide I and II modes are indicated as described for A). The direction of the surface enhanced EM field is illustrated by the fat black arrow. C) Cartoon of a nanodisc in site-plane view with different tilt angles towards the surface (green: MSP, blue: lipids polar heads). Amide I and II modes are indicated as described for A). The direction of the surface enhanced EM field is illustrated by the fat black arrow. With regard to the surface selection rule, the impact of the orientation of the amide mode vibration on the respective SEIRA intensities is described by the v-shaped form above the nanodiscs cartoon. The higher the intensity the thicker the form. D) Orientation of a DMPC molecule relative to the nanodiscs and the experimental surface plane. The orientation of one lipid molecule represents the orientation for all lipid molecules, since they are parallelly aligned to each other. The orientation of the lipid molecule corresponds to the respective overlying picture of the nanodisc cartoon in C). The impact of the orientation on the respective SEIRA intensities is described by the v-shaped form. The possible directions of the vibrational mode is highlighted by the orange shaded ellipse-shaped plane and orange arrows. The rotation of the molecule is indicated by the circular arrow, which encircles the orange shaded ellipse. The figure was prepared using Adobe Illustrator CS5 and ChemSketch.

5. Results and Discussion

Figure 5.11 depicts the absorption kinetics for amide I at 1655 cm^{-1} and amide II at 1550 cm^{-1} , respectively. The data were fitted with a bi-exponential function, giving the time constants of $t_{1,amideI}$ of 9.8 ± 0.4 min and $t_{2,amideI} = 220 \pm 9$ min for the amide I band and $t_{1,amideII} = 8.2 \pm 0.6$ min and $t_{2,amideII} = 307 \pm 14$ min for amide II, respectively. These time constants were assigned to two different processes. While the fast ones represented the binding of the nanodiscs to the Ni-NTA SAM, the second one reflected predominantly changes in orientation of the bound nanodiscs. The orientation process was completed after around 100 min.

The stability of the nanodiscs on the surface after overnight binding was confirmed by SEIRAS, thus, represented a stable background for the following folding experiments.

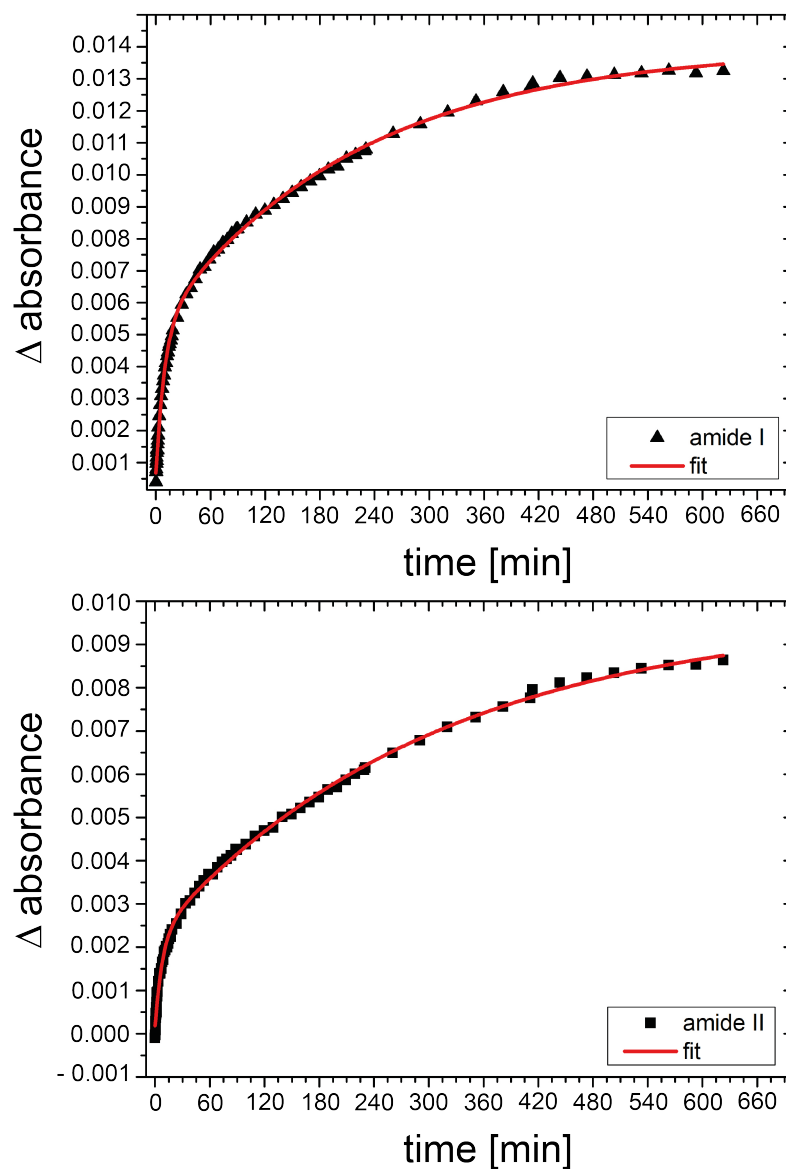


Figure 5.11: SEIRA measurement of nanodisc binding: absorption kinetics of the amide I (1655 cm^{-1}) and II (1550 cm^{-1}) bands. The absorption intensities were based on background subtracted SEIRA spectra, which were additionally baseline corrected. The baseline was returned by a linear fit of the data points in the regions 2450 to 2410 cm^{-1} and 1900 to 1850 cm^{-1} . Fitting was performed and depicted by the software OriginPro 9.0.0G, furthermore Adobe Illustrator CS5 was used.

5. Results and Discussion

MSP1D1/DMPC nanodiscs

Self-made MSP1D1/DMPC nanodiscs (see section 4.3.2) were bound to the SEIRAS sample surface following the protocol, described in section 4.5.2.2. Figure 5.12 shows a representative background subtracted SEIRA spectrum after approximately 45 min.

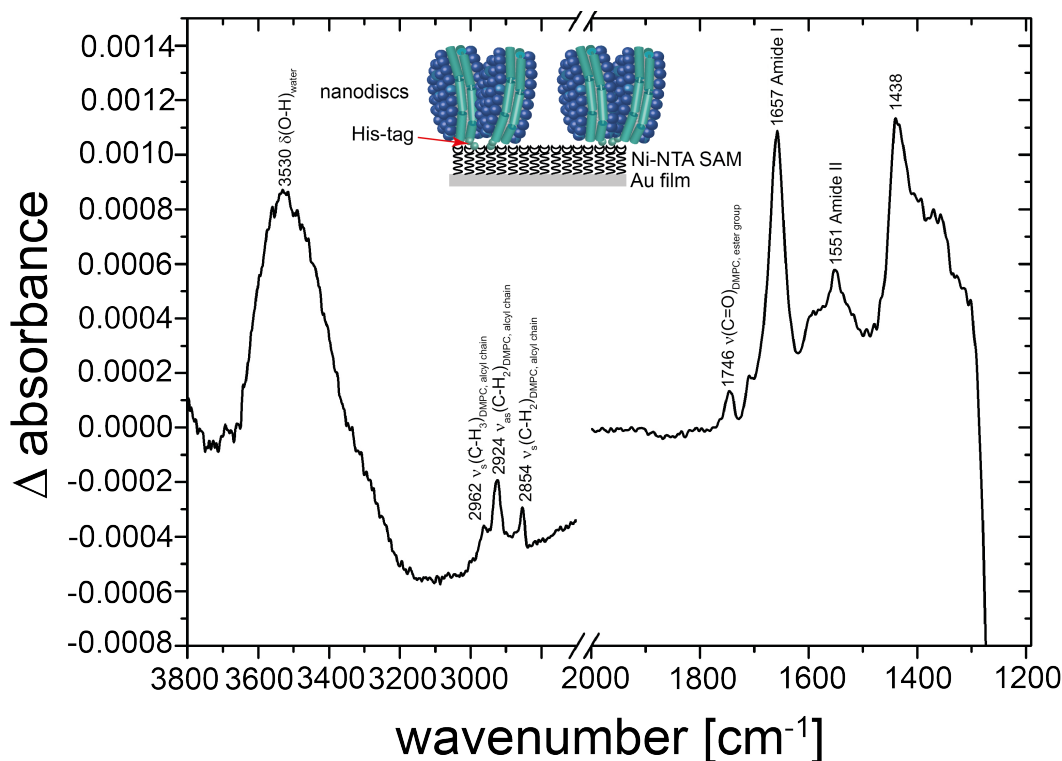


Figure 5.12: Illustration and background subtracted SEIRA spectrum of the MSP1D1/DMPC nanodisc immobilization process after 45 min incubation time. Here, 1 μM final concentration of nanodiscs in 50 mM NaPi, pH 7.4 were incubated at room temperature overnight. The figure was prepared using Origin9.0.0G and Adobe Illustrator CS5.

The spectrum revealed vibrational bands similar to the commercial nanodiscs from the MembraneMaxTM HN protein expression kit. The asymmetric, symmetric CH_2 and symmetric CH_3 stretching vibrations of the fatty acids of the DMPC lipids occurred at 2854, 2924, and 2962 cm^{-1} , respectively. Furthermore, amide I and amide II bands of the scaffold protein were visible at 1657 and 1551 cm^{-1} . However, the amide I band was overlapping with the O-H bending vibration of adsorbing water to the surface which was also indicated by the broad positive band at 3530 cm^{-1} . In contrast to the commercial nanodiscs the C=O stretching vibration of the lipid ester groups appeared with 1746 cm^{-1} at slightly higher frequencies (see Fig. 5.9). Also the bands as-

signed to the Ni-NTA and His-tagged protein interactions that occurred below 1490 cm^{-1} did not show the normal pattern as observed for the commercial nanodiscs, only the band at 1438 cm^{-1} was visible for binding self-made nanodiscs. Taken these observation into account, it appeared that the self-made nanodiscs did not form a uniform layer on top of the Ni-NTA SAM as observed for the commercial ones.

The strong lipid peaks in comparison to the amide peak might suggest a disassembling of the nanodiscs due to their interaction with the surface. Another explanation for this behavior might be the shorter linker between the His-Tag and the scaffold protein. Thus, the missing flexibility of the nanodiscs when bound to the surface might have led to aggregation on the surface or to the assembly of other morphologies by sticking to each other. Due to this observation the commercial nanodiscs were chosen as biomimetic membrane for all following folding experiments.

5.3.3 Folding of bR

After the surface preparation and the immobilization of the commercial nanodiscs, the following folding experiment was performed for bR. For recombinant protein expression, the cell-free protein synthesis system MembraneMaxTM HN was applied [109].

In the experiment shown here, the surface was covered by $200\text{ }\mu\text{L}$ 0.25X IVPS reaction buffer and a background spectrum was recorded. Subsequently, $50\text{ }\mu\text{L}$ of the reaction mix was added to the surface, including 0.02 mM all-*trans* retinal final concentration but without template DNA. In subsequent experiments, this step was simplified (following the protocol in section 4.5.3), which reproduces data without significant changes. In the simplified protocol, the surface was covered by 50 mM NaPi buffer (pH 7.4) instead IVPS buffer. Immediately after adding the reaction mix to the surface, successive SEIRA spectra were recorded. Representative absorption spectra are depicted in figure 5.13 (colored lines). Absorption bands at 1657 and 1548 cm^{-1} were observed and assigned to amide I and II from protein components of the system. A control experiment under identical conditions but without nanodisc monolayer was executed and is exemplary represented by the dashed SEIRA spectrum in figure 5.13. It shows comparable band positions for amide I and II.

As the bound nanodiscs on the surface occupy most of the space of the enhanced EM field (approximately 10 nm from the experimental surface plane), the water desorption band at around 3500 cm^{-1} , was weaker as compared to the control experiment (Fig. 5.13 A). Furthermore, for both experiments, no

5. Results and Discussion

typical absorption patterns were expected for the spectral range $< 1490 \text{ cm}^{-1}$ as described for nanodisc binding in the previous section, because no further histidine Ni-NTA interactions were assumed (compare the spectra of Fig. 5.13 with Fig. 5.9). The observed differences between the ratios of amide I and II of both experiments originate from different water desorption processes (see Fig. 5.13). The water bending mode overlapped with the amide I mode and therefore influenced the ratios between amide I and II differently.

After approximately 1 h, no further significant changes were expected for the absorption intensities. To preserve the vitality of the systems cytosolic components, the measurement was stopped and the experiment was continued (see next section).

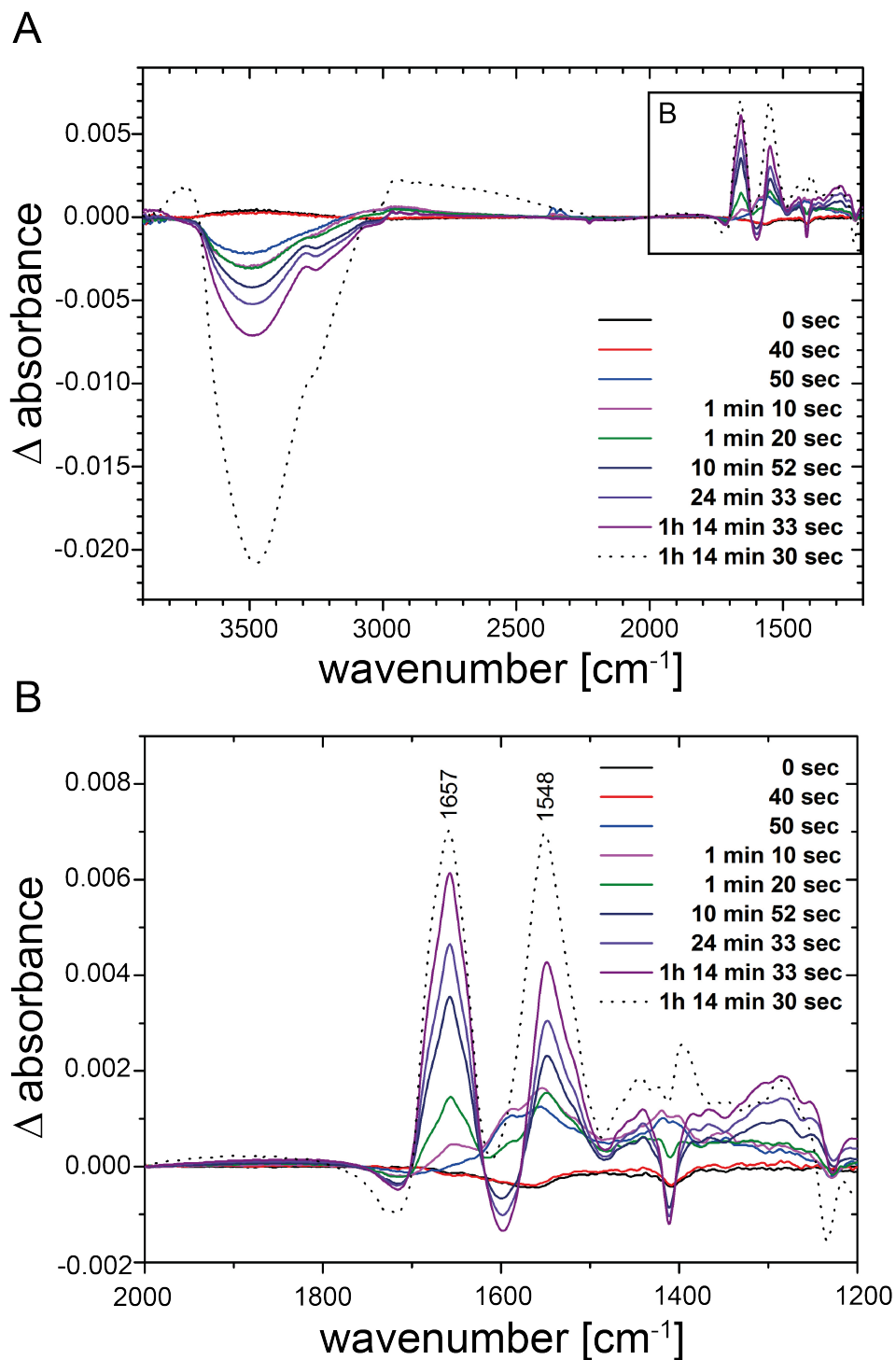


Figure 5.13: A) Selected background subtracted SEIRA spectra of the protein synthesis reaction mix without DNA template after indicated time periods (colored solid lines), starting at zero seconds when adding the mix to the surface. The dashed spectrum belongs to a control experiment without nanodisc monolayer but otherwise identical conditions. The spectral range in the rectangular frame is magnified in B). The figures were prepared using Origin9.0.0G and Adobe Illustrator CS5.

5. Results and Discussion

Induction of bR transcription and translation by adding the DNA template

After subtracting the saturated absorption spectrum of the reaction mix, the cell-free transcription and translation of bR was initiated by adding 1 μg template DNA (pEXP5-CT/bR) diluted in 50 μL feeding mix. The feeding mix containing ingredients to maintain the vitality of the system did not lead to additional signals in the SEIRA spectra (data not shown). Figure 5.14 depicts the complete SEIRA data set, which was recorded after starting the reaction by adding the DNA. Shown are the spectral range of the amide I and II signals on the x-axis, the time course on the y-axis, the absorbance on the z-axis and an illustration of the amide I and II vibrations within a peptide bond.

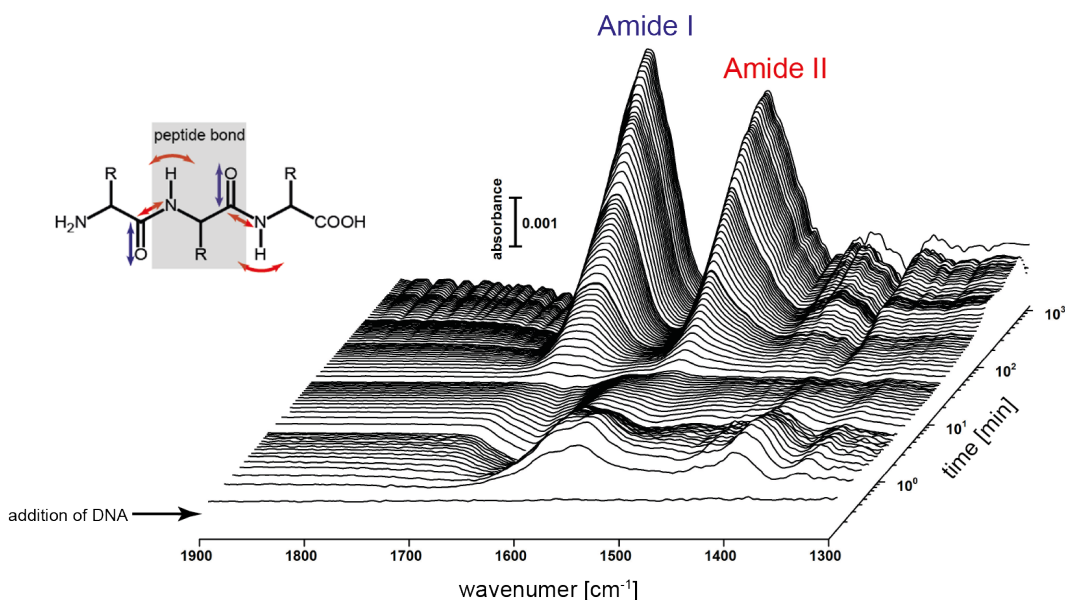


Figure 5.14: SEIRA spectra after initialization of transcription and translation of bR by the template DNA. The figure was prepared using Origin9.0.0G and Adobe Illustrator CS5.

From the waterfall diagram in figure 5.14 representative spectra were selected and described in detail in the following paragraphs.

Pre-conditioning period prior to protein insertion (0–8 min)

The SEIRA spectra (solid lines) in figure 5.15 visualize events during the first minutes after induction, whereas the dashed spectra relate to an identical experiment but without nanodisc monolayer. Within the first minutes an adsorption process was observed, revealed by appearance of positive bands at 1348,

1411, 1489, 1561 and 1595 cm^{-1} . After 5 min, these bands started to disappear due to desorption processes. Simultaneously, a desorption/adsorption process at 1229 and 1660 cm^{-1} took place.

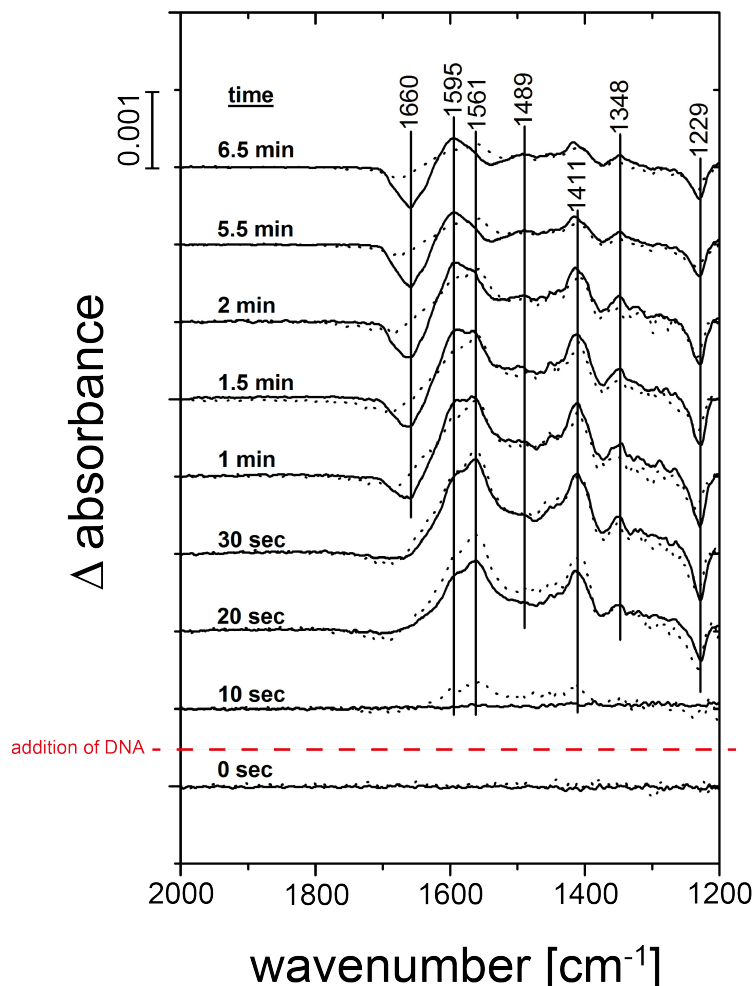


Figure 5.15: Early SEIRA spectra (time range 0 – 6.5 min) after initialization of the cell-free bR expression into nanodiscs by adding the template DNA (solid lines) and spectra of a control experiment without nanodisc monolayer but otherwise identical conditions (dashed lines). The figure was prepared using Origin9.0.0G and Adobe Illustrator CS5.

Except for the negative band at 1660 cm^{-1} , these bands were not significant for amide mode vibrations. The assignment of the bands was difficult, because of the component complexity of the sample solution and the superposition of divers vibrational bands. The region $< 1500 \text{ cm}^{-1}$ is sensitive to the amide III mode, the Ni-NTA SAM as well as the IR finger print region, the latter including lipids and carbohydrates. The spectra of the control experiment without nanodiscs (Fig. 5.15, dashed spectra) showed similar bands below 1500 cm^{-1} . However, the band at 1660 cm^{-1} was not that strong in the

5. Results and Discussion

control experiment and also the positive band at 1595 cm^{-1} did not increase as compared to the experiment with nanodiscs. By comparison with experiments on the Ni-NTA SAM under various pH conditions [132], the bands at 1595 , 1489 and 1411 cm^{-1} in figure 5.15 were assigned to the partial deprotonation of the asymmetric and symmetric COO^- stretching modes of Ni-NTA molecules. The signal at 1229 cm^{-1} might be assigned to asymmetric P=O stretching vibrations of the used NaPi buffer rather than the lipid of the tethered nanodiscs, since the signal also appears in the control experiment without nanodiscs. In summary, these bands were supposed to relate to components of the protein expression system rather than events associated with the translational, transcriptional or any other processes due to protein biosynthesis.

The band at 1660 cm^{-1} was assigned to amide I. However, this band superimposed with water bending vibrations at approximately 1645 cm^{-1} . The absorption kinetics for the water combination mode at 2120 cm^{-1} (Fig. 5.16) show that water molecules leave the surface during the first minute.

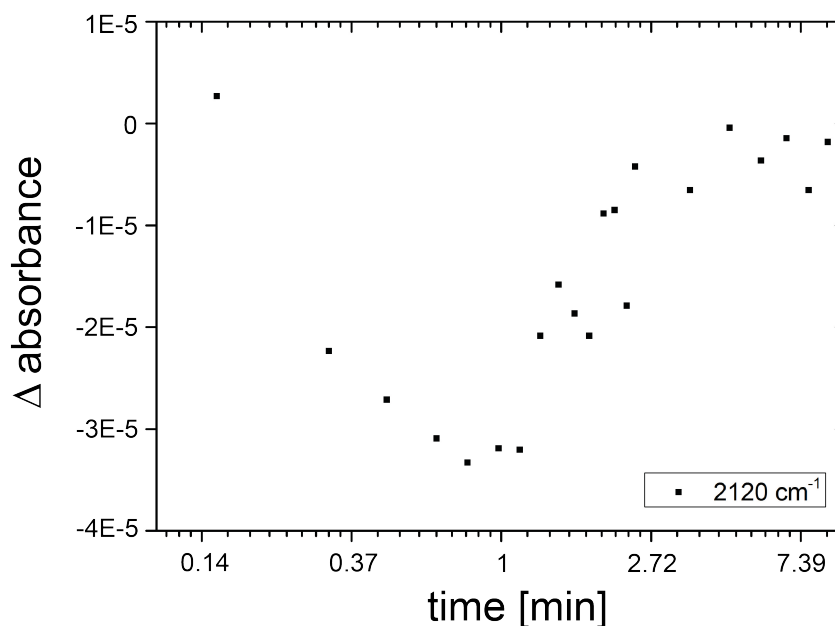


Figure 5.16: Absorption kinetics of the water combination mode at 2120 cm^{-1} after adding the feeding mix solution (with DNA). The absorption intensities were based on background subtracted SEIRA spectra, which were additionally baseline corrected. The baseline was obtained by linear fit of the data points in the regions 2450 to 2410 cm^{-1} and 1900 to 1850 cm^{-1} . The figure was prepared using Origin9.0.0G and Adobe Illustrator CS5.

Bacteriorhodopsin insertion into the nanodiscs and formation of secondary structures (8–60 min)

After about six to eight minutes (Fig. 5.17) the negative band at 1659 cm^{-1} (amide I) decreased. New bands appeared at 1678 and 1651 cm^{-1} , which are representative for amide I mode vibrations of turns and random structures, respectively [80]. During 17 minutes to one hour, these bands grew and shifted their maxima towards a broad band centered at 1661 cm^{-1} , at which the amide I mode of an α -helical polypeptide backbone can be typically expected. Synchronously, a band at 1551 cm^{-1} started to rise, which was assigned to amide II of an α -helical protein structure [80, 133].

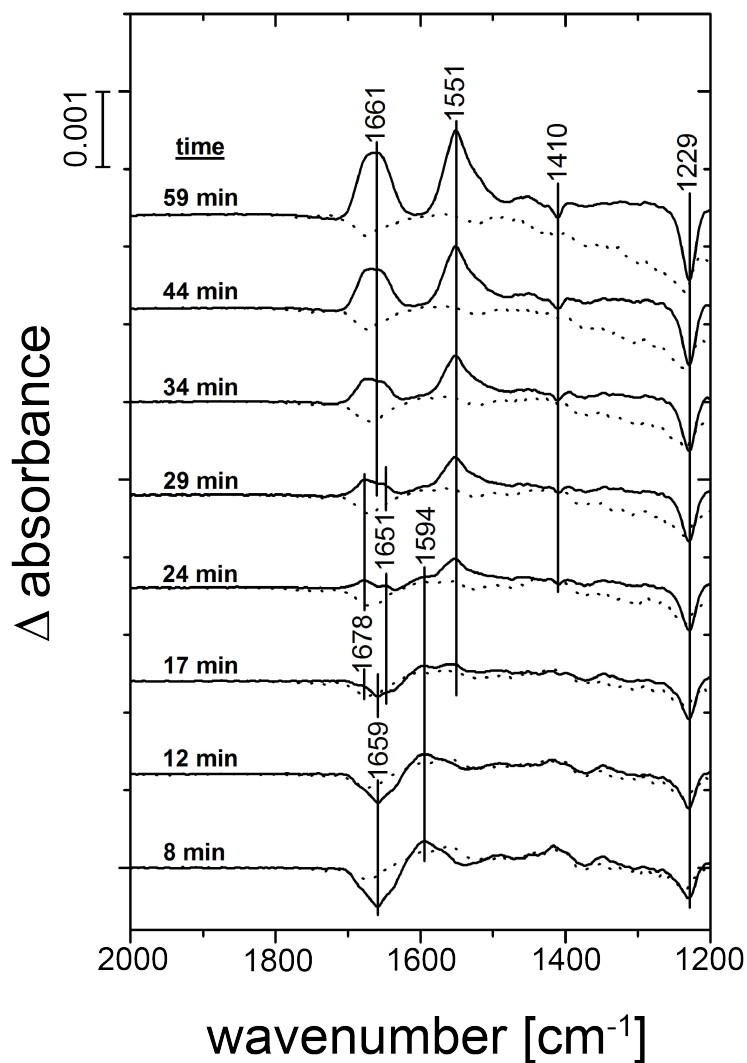


Figure 5.17: Selected SEIRA spectra (time range 8 – 59 min) visualizing membrane insertion of the polypeptide chain and formation of secondary structure (solid lines) and spectra of a control experiment without nanodisc monolayer but otherwise identical conditions (dashed lines). The figure was prepared using Origin9.0.0G and Adobe Illustrator CS5.

Because of the SEIRAS selection rule, the random adsorption of proteins to the surface is supposed to show almost constant signal ratios of amide I to amide II over time. The increase of the ratio (Fig. 5.18) during the first hour indicates a secondary structure formation or/and an orientation change.

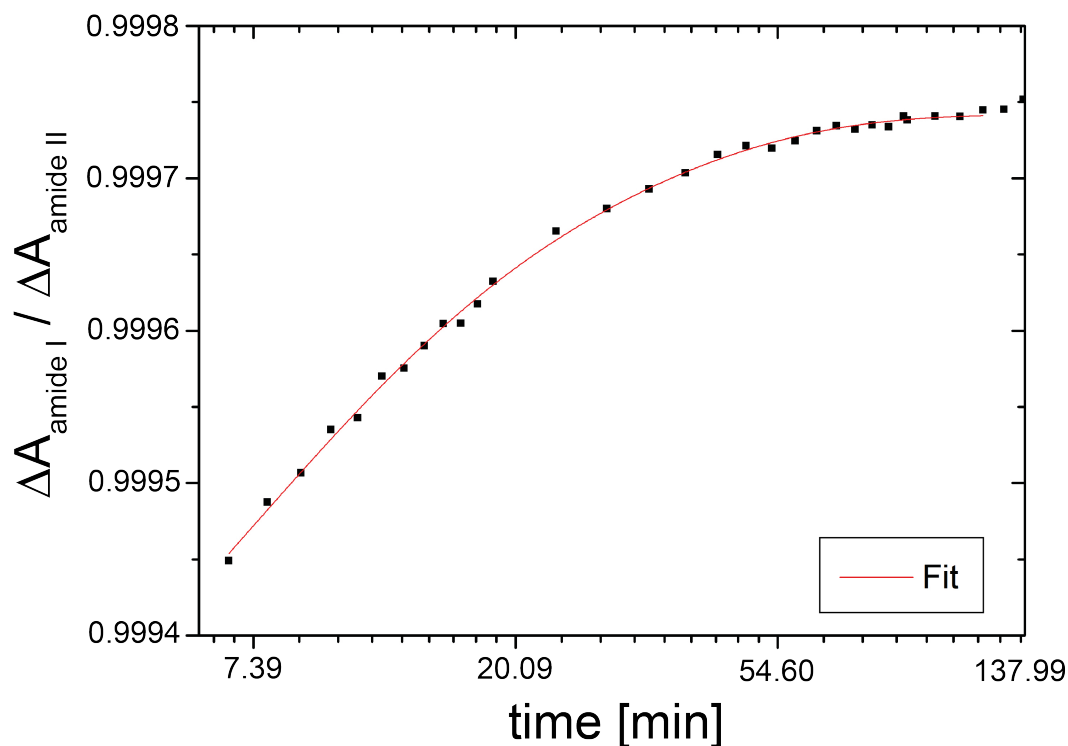


Figure 5.18: Absorption kinetics ratio of the amide I (at 1660 cm^{-1}) and II (at 1550 cm^{-1}) mode in the time period of 6.5 min and approximately 2 h. The data were fitted by a monoexponential function in the depicted time range. The absorption intensities were based on background subtracted SEIRA spectra, which were additionally baseline corrected. The baseline was returned by linear fit of the data points in the regions $2450\text{ to }2410\text{ cm}^{-1}$ and $1900\text{ to }1850\text{ cm}^{-1}$. The figure was prepared using Origin9.0.0G and Adobe Illustrator CS5.

During this time period, the SEIRA spectra of the control experiment (Fig. 5.17 dashed lines) did not show positive bands in the amide regions. As compared with figure 5.15, it was observed, that the band at 1594 cm^{-1} faded away, the negative band at 1410 cm^{-1} continued to increase and the negative band at 1229 cm^{-1} started to increase again.

In summary, it was concluded, that protein adsorbed within 10 nm distance to the surface. This region was entirely occupied by a nanodisc monolayer. Since the control experiment without nanodiscs did not show comparable spectra, the appearing amide signals were associated with the addition of the bR encoding DNA template in combination with the lipidic milieu of the nanodiscs. On that basis, the appearance of an α -helical secondary structure shows, that the membrane protein bR was translated and folded into the surface tethered nanodiscs.

Formation of tertiary structure (> 1 h)

In the time range from 1 – 9 h, the adsorption maxima at 1661 and 1549 cm^{-1} increased in their intensities (Fig. 5.19), whereas changes with respect to band shape and position were hardly visible. Simultaneously, the negative bands at 1410 and 1229 cm^{-1} continued to increase. The control experiment without nanodiscs on the surface did not show any increasing or decreasing bands in the amide regions.

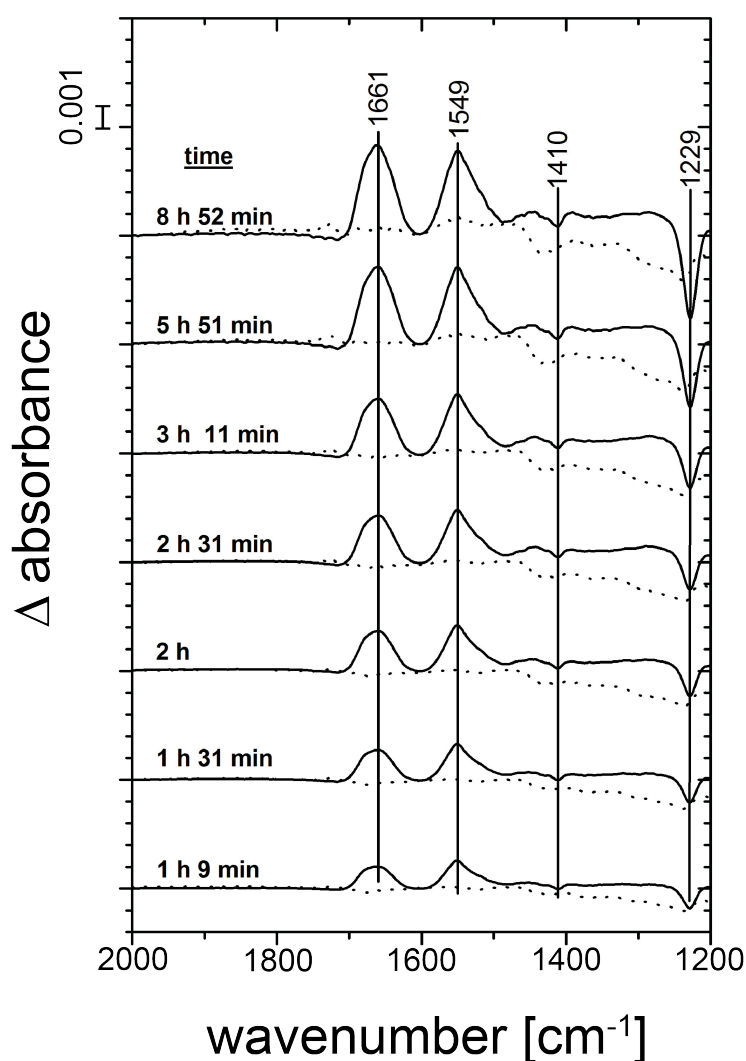


Figure 5.19: SEIRA spectra in the time range 1 – 9 h, visualizing tertiary structure formation (solid lines), which were depicted continuative to figure 5.17. The dashed lines represent the spectra at same time points of a control experiment without nanodisc monolayer but otherwise identical conditions. The figure was prepared using Origin9.0.0G and Adobe Illustrator CS5.

The time course of the bR incorporation process was followed by the absorption kinetics of the amide I and II mode as well as the water combination

mode at 2120 cm^{-1} (Fig. 5.20). The absorption intensities of amide I and II constantly increased until approximately two to three hours along with an unchanged amideI/amideII ratio (Fig. 5.20, red triangles) showing a protein adsorption process. Thereafter, the slope of amide I and amide II started to decrease (Fig. 5.20, black symbols), due to saturation of the protein adsorption. The difference between the slopes after two to three hours was caused by the overlapping bending band of the displaced water. The kinetics of the water combination mode at 2120 cm^{-1} (Fig. 5.20, blue symbols) indicated an almost linear water desorption process, which significantly slowed down after approximately three hours. This process coincided with the kinetics of amide I and II, showing that water molecules were repelled from the surface by inserting protein. After five hours, the band change slowed down, thus the folding and insertion process of bR into the surface tethered nanodiscs was mostly completed.

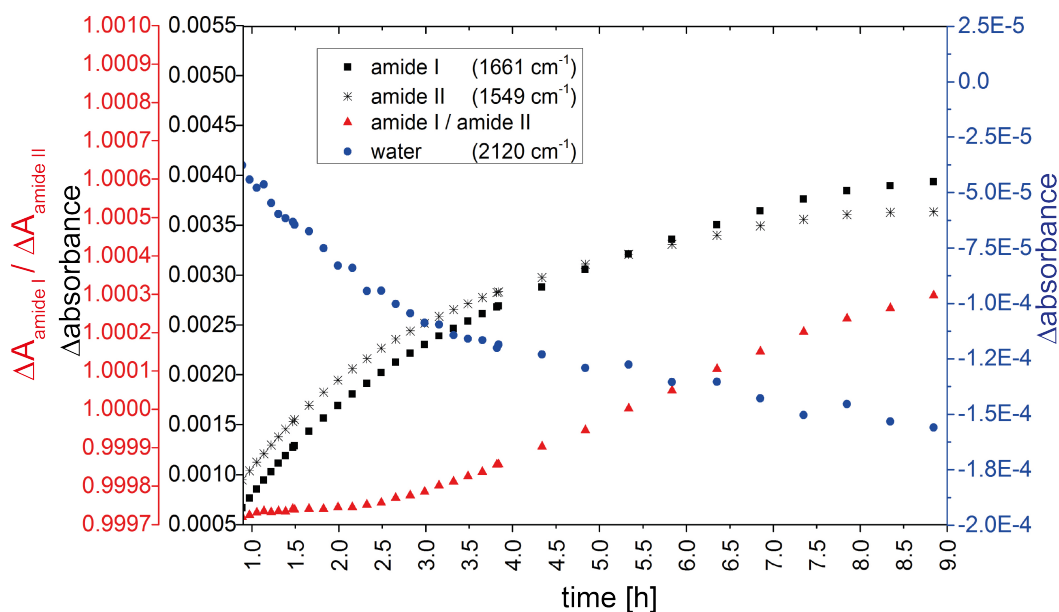


Figure 5.20: SEIRA measurement after adding the feeding mix solution (with DNA): Absorption kinetics of the amide I (at 1660 cm^{-1} ; black squares), amide II (at 1550 cm^{-1} ; black stars), water combination mode (at 2120 cm^{-1} ; blue dots) and amideI/amideII ratio (red triangles). The absorption intensities were based on background subtracted SEIRA spectra, which were additionally baseline corrected. The baseline was obtained by linear fit of the data points in the regions $2450\text{ to }2410\text{ cm}^{-1}$ and $1900\text{ to }1850\text{ cm}^{-1}$. The figure was prepared using Origin9.0.0G and Adobe Illustrator CS5.

To analyze the folding process more detailed the secondary structure evaluations had been expanded by comparing the second derivatives of the selected

5. Results and Discussion

spectra (Fig. 5.21). The SEIRA absorption spectra are depicted side by side to their second derivatives. Additionally, a spectrum of early processes after approximately 30 min (see also Fig. 5.17) was chosen. The second derivatives revealed a signal development of an α -helical secondary structure starting from random and turn-structures. The representative bands are highlighted by the red dashed lines in figure 5.21. The prominent signals of the amide I band after 30 min were observed at 1678 and 1651 cm^{-1} and assigned to turn- and random protein structures [80]. After one hour, a third peak development was observed at 1656 cm^{-1} , which is representative for single α -helices. At five hours, the peak shifted towards 1658 cm^{-1} , which is typical for α -helical bundles. Furthermore, the signal became much stronger over time and started to dominate the other peaks, which influenced the shape and position of the overall amide I band (see SEIRA spectra in Fig. 5.21, left) and led to the band shift towards 1661 cm^{-1} (see red dashed lines in Fig. 5.21, SEIRA spectra on the left). A comparable behavior of the amide II band was not observed. The positions of the prominent peak in the second derivatives remained unaltered at 1553 cm^{-1} and in the SEIRA spectra at 1550 cm^{-1} .

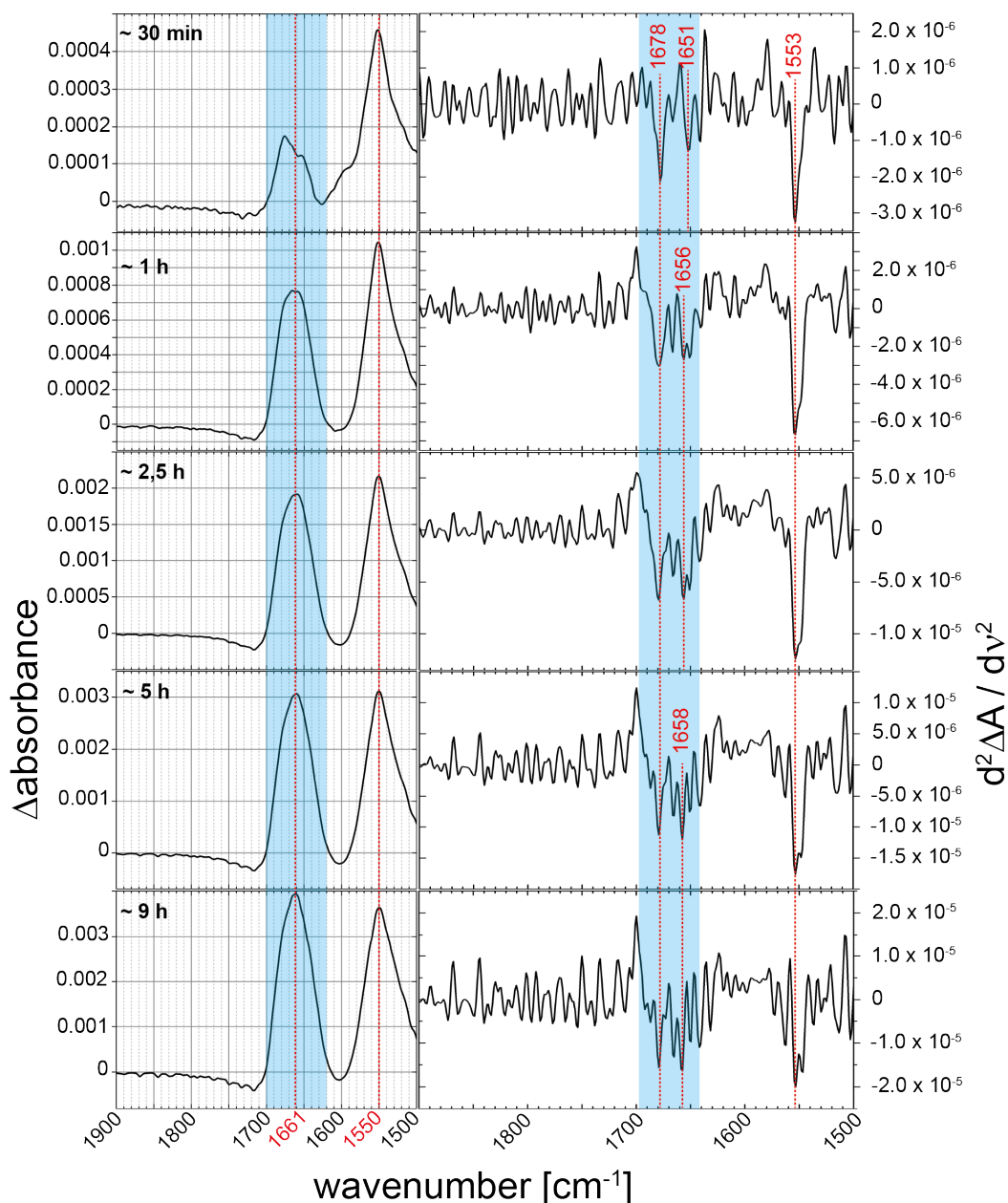


Figure 5.21: Baseline corrected SEIRA spectra after adding the DNA (left) and the respective second derivative (right). The time points were selected according to figure 5.20. The blue shading highlights the area of the amide I signal. Note: The region between 1900 cm^{-1} and the amide I band was chosen to represent the noise level of the second derivatives. Its amplitude was used to evaluate prominent peaks qualitatively in the region of interest. Maxima in the range of background fluctuations were neglected. Another challenge was liquid water and water vapor (see section 4.5.9). Other peaks than the prominent ones were not considered. The second derivative evaluation and the described kinetics have to be considered purely qualitatively and with special attention on noise signals from the background and water. The second derivative were obtained by employing a Savitzky–Golay filter with polynomial order two and five data points window size. The figure was prepared using Origin9.0.0G and Adobe Illustrator CS5.

5. Results and Discussion

Simultaneously with increased absolute intensities and the band shift of the amide I band towards a typical α -helical bundle protein, a band narrowing of the amide I mode was observed (Fig. 5.22). This can be explained by the alignment of the amide I mode vibrations with the surface enhanced IR field, which leads to a pronounced absorption signal. Moreover, the helix packing process during tertiary structure formation can lead to coupling of the amide I dipole moments of neighboring α -helices, which results in a dominant, sharpened absorption profile at approximately 1660 cm^{-1} [76,80,134].

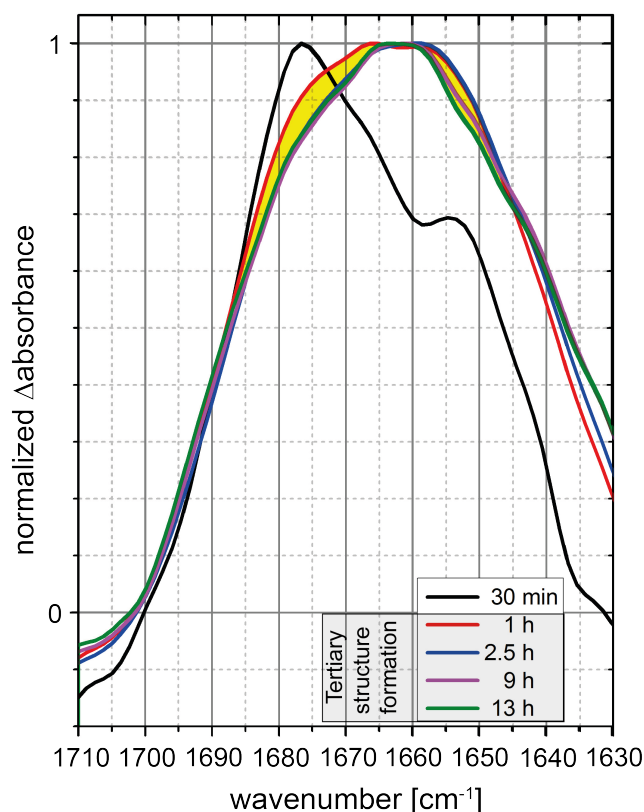


Figure 5.22: Baseline corrected and normalized SEIRA spectra at different time points of the reaction in figure 5.21. The band narrowing over time during tertiary structure formation as indicated by the yellow shaded area. The figure was prepared using Origin9.0.0G and Adobe Illustrator CS5.

In summary, > 1 h after transcription and translation of bR was initialized, the observations revealed:

1. an increased arrangement and packing of the transmembrane α -helices perpendicular to the surface which led to the enhanced resonance of the amide I mode vibrations of the α -helices with the enhanced electromagnetic field (surface selection rule, see section 2.3.4).

2. an increase in α -helical content upon tertiary structure formation which leads to vibrational coupling between single helices resulting in a stronger transition dipole strength of the amide I mode.

The relative intensity increase of the amide I versus the amide II band representing an increase in α -helical content during tertiary structure formation can be explained by the model of Hunt et al. [135] in which the last helices F and G of bR are formed only if stabilized by the interaction with the first five helices A to E [45, 135]. Atomic force microscopy (AFM) and SMFS studies by Kessler et al. support and refine this model even for bR in purple membrane [136, 137].

In conclusion, the first hour reflects insertion and folding of helices A to E (Fig. 5.23 (A)). The amide I dipole components of the individual α -helix (red arrows Fig. 5.23) are poorly aligned to each other and to the enhanced electromagnetic field. The coupling with the enhanced electromagnetic field (black arrows at left) is small. After 1 hour, as the protein forms tertiary structure, the helices F and G were inserted into the membrane layer and form α -helical structure (Fig. 5.23 (B)). Thus, the total amount of α -helices got enlarged leading to an increase in the intensity of the amide bands. At the same time, the dipoles of each transmembrane α -helical component coupled in one direction. The directional dipoles coupled strongly with the enhanced EM field, which led to additional narrowing of the amide I band. Hence, the events > 1 h represent predominantly subsequent insertion and folding of helices F and G concomitant with tertiary structure formation.

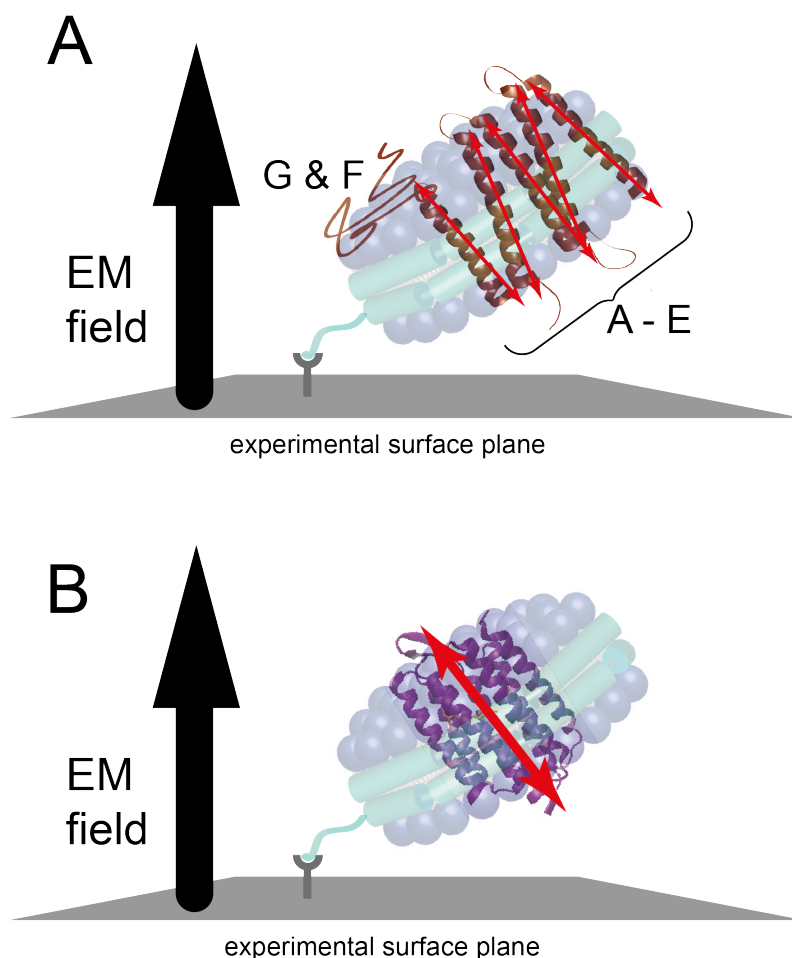


Figure 5.23: Models interpreted from the observed SEIRA spectra during the folding experiment according to the surface selection rule of SEIRAS: (A) 8 min to 1 h; (B) > 1 h. Narrow red arrows represent dipole components in the α -helices. Thick black arrows illustrate the enhanced electromagnetic field. The figure was prepared by means of Adobe Illustrator CS5.

5.3.4 Functionality of bR in the SEIRAS folding experiment

SEIRA difference spectroscopy to probe the functionality of cell-free expressed bR after folding into surface tethered nanodiscs

To verify the correct folding of bR into the surface tethered nanodiscs, the functionality of bR was analyzed by probing the photocycle activity using light-induced SEIRA difference spectroscopy described in section 4.5.4. As the activity test immediately after the folding experiment (described in the previous section) did not work out, several different modifications had been performed to improve the experiment (see Tab. 5.1). However, all approaches to collect a representative difference spectrum gave no result.

Challenges to detect the light-induced absorption difference spectrum of

functional bR could result from too short life times of its photocycle intermediates M and N, respectively. Furthermore, since the absolute intensities of the SEIRA spectra were very low, the superposition of water bands can decrease the signal to noise ratio, which significantly impacts the resulting difference spectra.

Table 5.1: Modifications of the folding experiment (section 5.3.3) to collect a light-induced SEIRA difference spectrum of bR, which was cell-free expressed into surface tethered nanodiscs.

	Used protein construct	Modification	Description
A	bR	pH 10	Lower proton concentration hampers the proton uptake reaction leading to elongation of the N-intermediate state.
B	bR	Dried sample film	Lower background signal due to less vibrational modes of water molecules.
C	bRD96N	Mutation D96N as indicated in the construct name	Because of the missing aspartic acid 96, there is no protonation reaction of the deprotonated retinal, which leads to an elongated M-intermediate state.
D	bRD96N	Mutation D96N; increasing basic pH	See B and C.

In addition to the experimental modifications (Tab. 5.1), sample D was probed by Resonance Raman Spectroscopy after the SEIRA difference spectroscopy measurement. However, also here a spectrum could not be collected. Thus, either the photocycle was still too fast, cell-free expressed bR or bRD96N into nanodisc at the SEIRAS surface was not functional, the concentration of the target protein was too low or the instrumentation was the limiting factor. The following sections investigate these questions.

Laser flash photolysis of bR, cell-free expressed into nanodiscs in batch

To approve the function of cell-free expressed bR and bRD96N within nanodiscs respectively, the photocycle of samples prepared in a test tube outside the SEIRAS setup were probed by laser flash photolysis and are depicted in 5.24. For comparison, the flash photolysis kinetics of wild type (wt) bR from purple membrane (prepared from *H. salinarum* and subsequently reconstituted in DMPC liposomes) are shown.

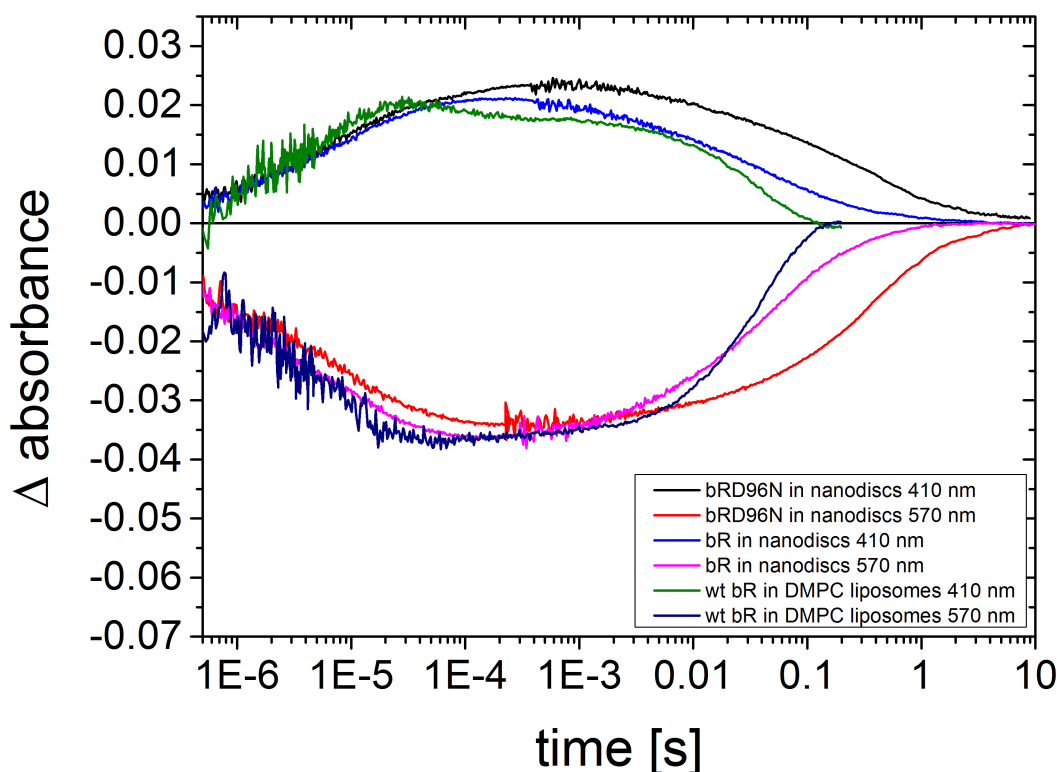


Figure 5.24: Laser flash photolysis data of functional bR and the slower functional variant bRD96N, which were both incorporated in commercial nanodiscs after cell-free expression. As a control, flash photolysis data of wt bR in purple membrane reconstituted in DMPC liposomes was plotted (data by courtesy of Mattia Saita, FU Berlin, Germany). The figure was prepared using Origin9.0.0G.

The absorbance kinetics at 410 and 570 nm indicated the fraction of the M intermediate and ground state, respectively. When compared to wt bR in DMPC vesicles, cell-free expressed bR within nanodiscs showed 5 times slower kinetics. The cell-free expressed variant bRD96N within nanodiscs decayed 3 times slower than bR in nanodiscs. Based on this observation, it was assumed, that successfully expressed bR or bRD96N into surface teth-

ered nanodiscs, revealed the same activity and functionality as in the batch experiments.

SEIRA difference spectroscopy on bR within nanodiscs, which was cell-free expressed in batch

A low sample concentration, which causes a too low signal-to-noise ratio, can challenge the detection of the light-induced absorption difference spectrum of functional bR. Therefore, samples from a batch experiment, which showed photocycle activity, were adsorbed to the SEIRAS sample surface and analysed by light-induced SEIRA difference spectroscopy. Table 5.2 lists the protein constructs, which were analyzed by this method as well as modifications to improve the measurement.

Table 5.2: Experiments to collect a light-induced SEIRA difference spectrum from batch samples of cell-free expressed bR and bRD96N within nanodiscs, including specifications to improve the measurements

	Protein construct	Specifications
A	bR	None.
B	bR	pH 10 to slow down the photocycle.
C	bRD96N	Mutation D96N to slow down the photocycle.
D	bRD96N	Fe(III)Cl ₃ * 6 H ₂ O to slow down the photocycle.

All four approaches could not deliver the expected difference spectra. As light-induced absorption difference spectra were measured successfully from SRII reconstituted in a surface tethered bilayer of polar lipids from *H. salinarum* by the described technique [138], the instrumentation should be sensitive enough to record a difference spectrum from a monolayer of a retinal protein.

Light-induced IR difference absorption spectroscopy on bR within nanodiscs by ATR FTIR

BR was cell-free expressed into nanodiscs in batch and analyzed by laser flash photolysis (data not shown) as described for figure 5.24, which approved the photocycle activity of bR. Subsequently, a fraction of the sample was concentrated 10 times (section 4.5.4).

5. Results and Discussion

Both samples were analyzed by a conventional ATR FTIR spectroscopy measurement (see section 4.5.4). A LED difference spectrum could not be collected for the not concentrated sample, whereas the analysis of the concentrated sample did result in a typical spectrum, which is depicted in figure 5.25. The difference signals were comparable to bR in purple membrane from *H. salinarum* in figure 4.4 and showed typical bands of the M- and N-intermediate state of the bR photocycle.

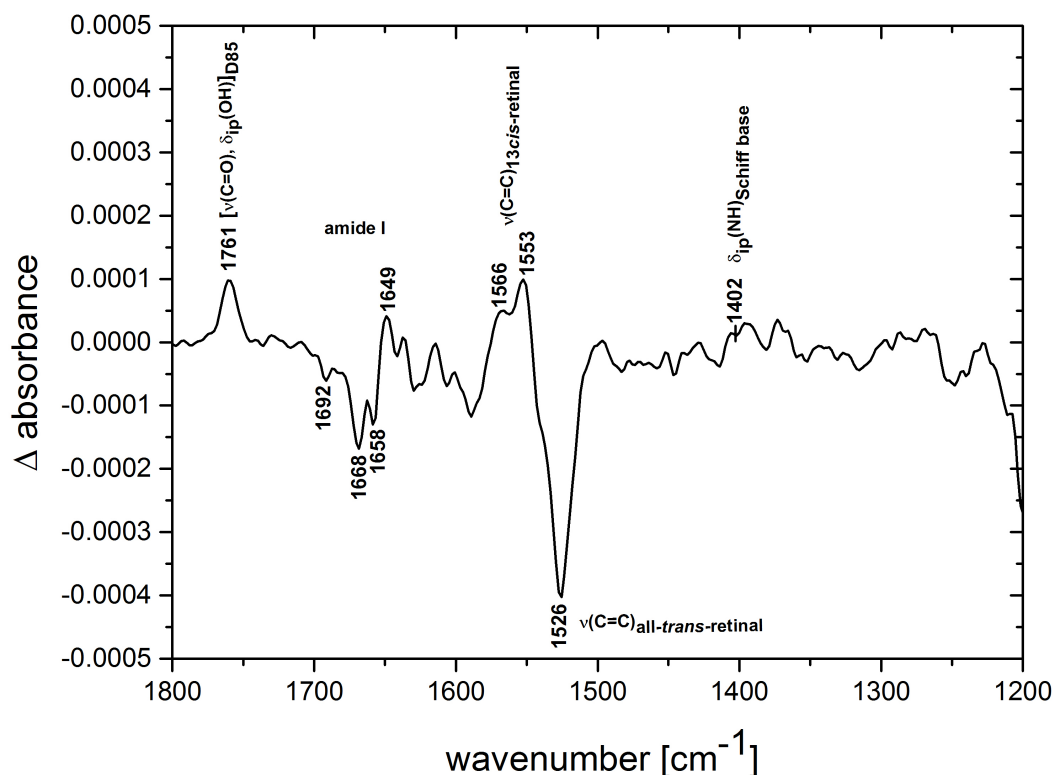


Figure 5.25: Light-induced FTIR difference spectrum of cell-free expressed bR in nanodiscs when dried onto a Silicon crystal and measured in ATR configuration. The spectrum is the average of 2000 spectra with a spectral resolution of 2 cm^{-1} . The light-induced spectra were recorded under illumination at 530 nm by an LED. For the band assignment see [27, 120]. The figure was prepared using Origin9.0.0G.

Note, the illumination procedure to collect the here described LED difference spectrum was similar to the procedure performed in the SEIRAS experiments on bR, which was expressed into surface tethered nanodiscs and on bR within nanodiscs, which was produced before in a test tube (see previous paragraphs).

Summary

The functionality of cell-free expressed bR, which was produced in batch, was approved by laser flash photolysis and by light-induced ATR FTIR difference absorption spectroscopy. However, a SEIRA difference spectrum of bR within nanodiscs, which was expressed on the SEIRAS sample surface, could not be collected. The applied modifications to elongate the photocycle and the SEIRA difference spectroscopy measurement of bR within nanodiscs from cell-free expression in a test tube, did not lead to a positive result either.

5.3.5 Impact of the co-factor retinal on the bR folding process

To investigate the co-factor impact on folding, the folding experiment was repeated under identical conditions but varying the retinal supply (section 4.5.6). In one approach no retinal was added in any step of the protein expression. The other approach used nanodiscs pre-treated with retinal. The corresponding SEIRA spectra are depicted in figure 5.26 together with spectra of the previous bR folding experiment at similar time points.

5. Results and Discussion

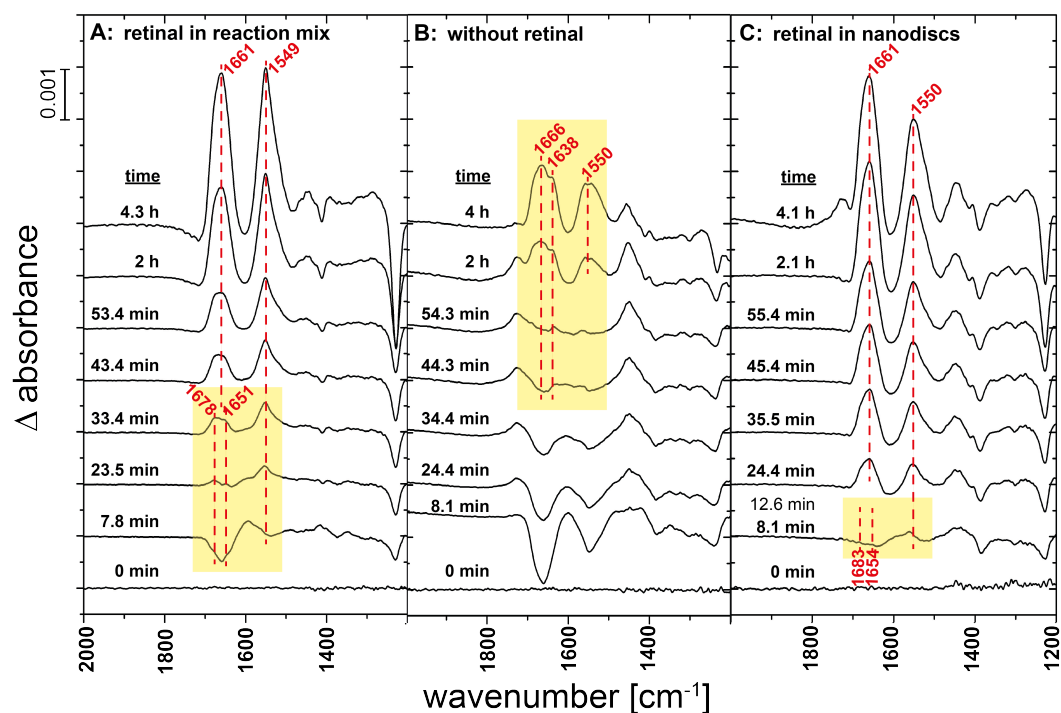


Figure 5.26: Selected background subtracted SEIRA spectra of the bR expression experiments: **A)** folding experiment described in section 5.3.3 with retinal present in the reaction mix. The time window, in which the development of the α -helices was suspected, is color-coded by the yellow shaded areas. It highlights the bandshape change in the amide I and II region; **B)** Folding experiment without retinal supply; **C)** Folding experiment with retinal pre-treated nanodiscs and no retinal in the reaction and feeding mix. The absorption intensities of B) and C) were additionally baseline corrected. The baseline was returned by linear interpolation of the data points in the regions 2000 to 1800 cm^{-1} and 1490 to 1475 cm^{-1} for B) and 2500 to 2400 cm^{-1} and 2000 to 1800 cm^{-1} for C). The figure was prepared using Origin9.0.0G and Adobe Illustrator CS5.

After the cell-free expression was initialized by adding the template DNA, the spectra showed comparable bandshapes and position of the amide I and II signals, but different time courses (Fig. 5.26). The folding experiments A (retinal in the reaction mix) and B (folding without retinal) in figure 5.26 showed a synchronous development of random (A: 1651 cm^{-1} ; B: 1638 cm^{-1}) and turn structures (A: 1678 cm^{-1} ; B: 1666 cm^{-1}) in the amide I region. However, in experiment C (retinal within nanodiscs), the appearance of turn structures (1683 cm^{-1}) was observed along with a signal typical for an α -helical structure (1654 cm^{-1}). Whereas no further band development or band shifts were detected for experiment B, the observed amide I bands in A and C shifted towards a peak at 1661 cm^{-1} , which is typical for an α -helical bundle protein.

For all three experiments an amide II band was detected at approximately 1550 cm^{-1} .

The observations revealed different folding kinetics due to the different co-factor supply. Without retinal the development of the amide mode signals was strongly slowed down and even stopped at the level of random (1638 cm^{-1}) and turn structures (1666 cm^{-1}), which is shown in figure 5.26, B. In comparison with the spectra of the folding experiment with retinal in the reaction mix (Fig. 5.26 A), the appearance of the signals, which were assigned to random and turn structures, were retarded of about 45 min to 1.5 hours. The shift of these bands towards a typical α -helical signal is not visible. Thus, formation of α -helices or a tertiary structure was nonexistent. Adding retinal to the experiment, immediately after the signal started to saturate, did not affect the signal at all (data not shown). This suggests, that retinal needs to be present in a very early state of BO secondary structure formation to end up in functional bR.

In denature/refolding experiments, bR was recovered from an unfolded state by retinal supply. These experiments start from unfolding of functional bR. It has been reported, that bR unfolding by strong detergents like SDS remains incomplete, even under retinal removal. Only by organic solvents a complete unfolding was achieved from which refolding was partially possible [22]. This led to the hypothesis, that bR might possess a stable core structure [139], which can not be easily denatured and from which renaturation by retinal supply is possible. As bR is not able to recover by post-addition of retinal during cell-free synthesis of BO, this proposed structure might not be established without retinal. Taken together, *in situ* folding and retinal binding under the conditions used here seem to be closely coupled processes.

In contrast, the pre-treatment of the lipid support with retinal accelerated the folding process (Fig. 5.26 C). Here, no further retinal addition was executed. Due to the hydrophobic nature of retinal, it resides within the nanodiscs. The appearance of the signals at 1683 and 1654 cm^{-1} as well as the shift towards 1661 cm^{-1} was completed after about 15 to 20 min. The following band-narrowing was completed after two to three hours. It is evident that the nascent polypeptide could interact unhampered with pre-adsorbed retinal during membrane insertion. In the case of retinal supply by the reaction mix (Fig. 5.26 A), the folding process might be slower due to its diffusion to the membrane or the blockage of the membrane by other components of the reaction mix. Evidently, under the conditions used here, open access to

5. Results and Discussion

retinal during polypeptide synthesis is essential for helix formation and folding of functional bR.

The experiments on folding were performed at approximately 20 °C, which was beneath the phase transition temperature of the used DMPC lipids (24 °C). Performing the folding experiment at 37 °C, where DMPC resides in the more fluid liquid crystalline phase, showed a comparable fast folding process [140] as for the experiment with retinal pre-treated nanodiscs in figure 5.26 C. Therefore, the fast folding process in figure 5.26 C might also be explained by a better accessibility of the nanodiscs due to an increase in fluidity of their lipid bilayers.

5.3.6 Cell-free expression of EmGFP

To exclude that cell-free expressed proteins, which were not associated with surface tethered nanodiscs (because they were soluble or precipitated) adsorb to the surface and cause false positive IR absorption signals, the water soluble β -barrel protein EmGFP was expressed on the SEIRAS sample surface covered with nanodiscs (section 4.5.7). No SEIRA spectra during expression were observed (Fig. 5.27) which were comparable to the bR folding experiment (Fig. 5.14).

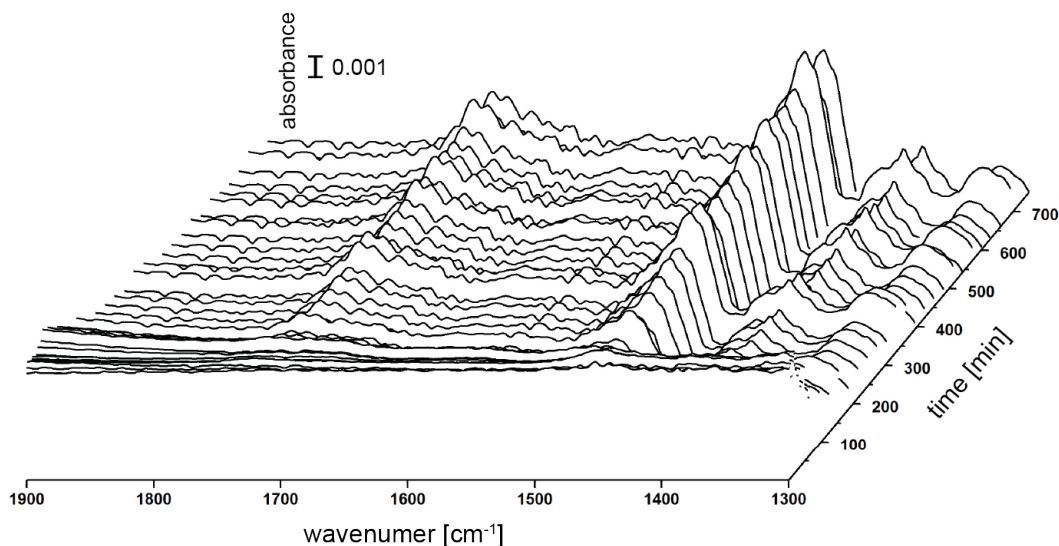


Figure 5.27: SEIRA spectra after initialization of transcription and translation of EmGFP by the template DNA. The figure was prepared using Origin9.0.0G and Adobe Illustrator CS5.

After 12 h, the supernatant was removed from the surface and measured by a conventional spectrofluorometer. The emission spectrum at 470 nm excitation is depicted in figure 5.28 showing a fluorescence peak at 515 nm verifying

EmGFP presence in the sample. The emission profile is comparable with the emission profile of EmGFP provided on the manufacturer's homepage employing their online tool Fluorescence SpectraViewer.

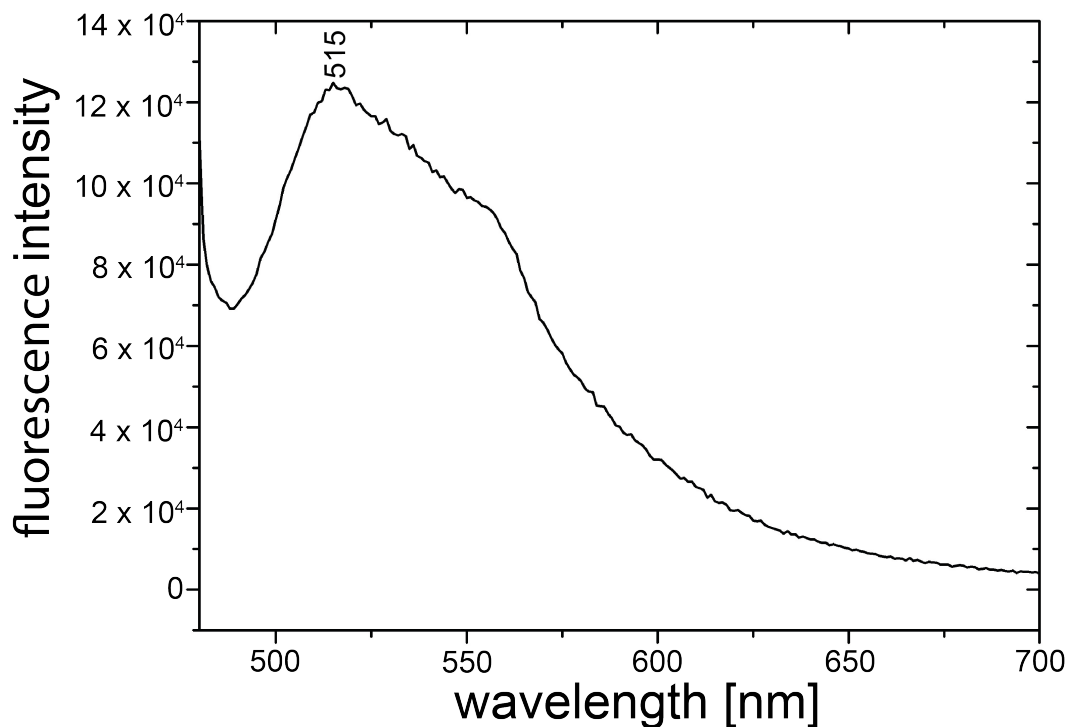


Figure 5.28: Emission spectrum of cell-free expressed EmGFP at 470 nm excitation. The figure was prepared using Origin9.0.0G.

Thus, this experiment shows, that the protein bands observed in the bR folding experiment were newly synthesized proteins localized at the surface. It supports the conclusion, that the bR signals were associated with insertion and folding into bound nanodiscs.

5.3.7 Folding of other microbial rhodopsins

To examine the transferability of the results from the bR folding experiment on other membrane proteins, initially three α -helical retinal membrane proteins were investigated, which are structurally similar to bR. These proteins were *HsSRI*, *HsSRII* and the transmembrane region of *CrChR2*. It should be mentioned here that before executing the SEIRAS experiments, all three proteins were tested for cell-free protein expression in a batch experiment (see section 5.2). A protein expression could not be detected by color change of the reaction mix or SDS-PAGE analysis. It seems to be a general challenge to functionally express other retinal proteins than bR by cell-free transcription and translation (personal communication with other groups). This raised the

5. Results and Discussion

question if this new methodology (SEIRAS and cell-free protein expression) can be employed to examine the occurring processes on a molecular level. The SEIRAS experiments were executed as described for bR with retinal (addition to the reaction mix and retinal treated nanodiscs). This should assure that all-*trans*-retinal is not a limiting factor. The SEIRAS experiments revealed at early time points similar results compared to each other as well as to bR. Figure 5.29 is a juxtaposition of the spectra's first minutes after adding the feeding mix and DNA to the reaction mix (in the time range of the pre-conditioning period of the bR folding experiment).

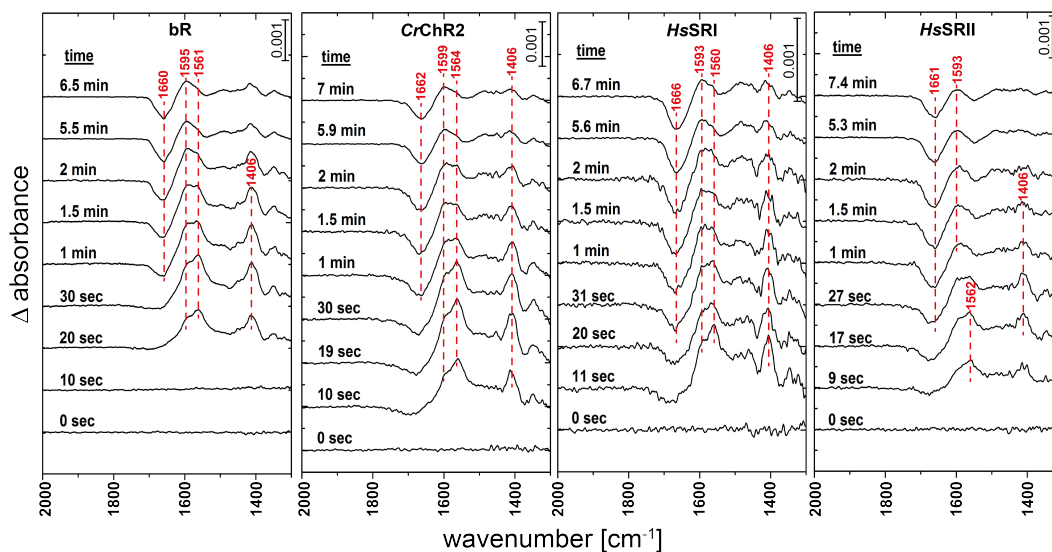


Figure 5.29: Background subtracted SEIRA spectra within the first eight minutes of the experiments (pre-conditioning period). Depicted are the spectra of **bR** folding described in section 5.3.3, the folding of **CrChR2**, **HsSRI** and **HsSRII**. Representative frequencies are highlighted by red dashed lines and labeled with red letters. The absorption intensities were additionally baseline corrected. The baseline was returned by linear interpolation of the data points in the regions 2500 to 2400 cm^{-1} and 2000 to 1800 cm^{-1} . The data were analyzed and depicted using Origin9.0.0G and Adobe Illustrator CS5.

Table 5.3 summarizes the band positions and assignment of the spectra in figure 5.29. As in the bR folding experiment (see also section 5.3.3), in all three proteins first a desorption process in the amide I region was observed. Furthermore, the pH effect on protonation and deprotonation of the Ni-NTA was visible too (bands of the COO^- stretching vibrations). Overall, the band positions and shapes were more or less similar.

Table 5.3: Assignment of the bands indicated in figure 5.29: Pre-phase.

Assignment	bR [cm ⁻¹]	<i>CrChR2</i> [cm ⁻¹]	<i>HsSRI</i> [cm ⁻¹]	<i>HsSRII</i> [cm ⁻¹]
Amide I	1660	1662	1666	1661
$\nu(\text{COO}^-)$	1595	1599	1593	1593
	1411	1406	1406	1406
unknown	1561	1564	1560	1562

After the first seven to eight minutes, signals in the amide I and II regions appeared. Representative spectra until the first hour are depicted in figure 5.30.

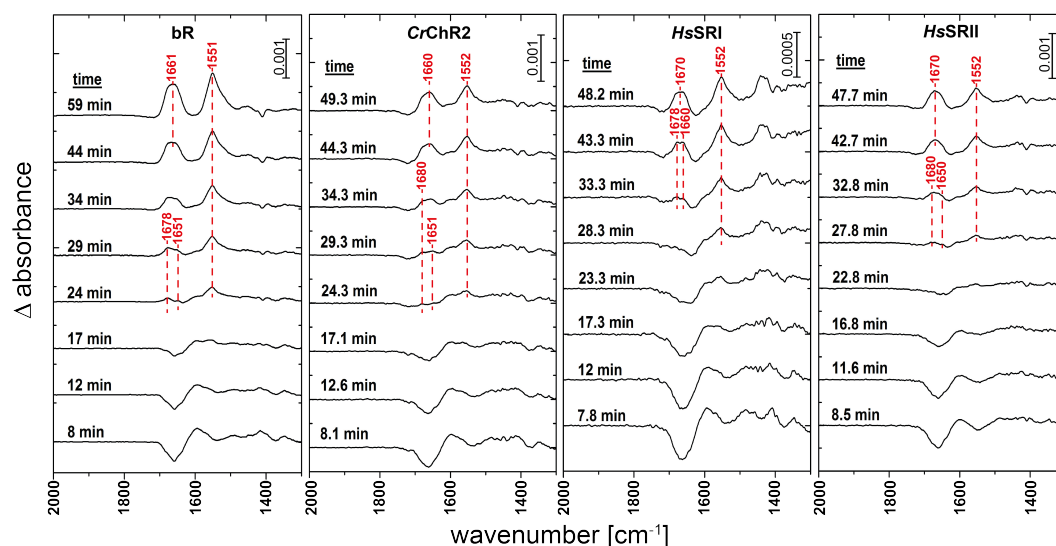


Figure 5.30: Background subtracted SEIRA spectra in the time range of the first eight minutes and approximately one hour from **bR**, ***CrChR2***, ***HsSRI*** and ***HsSRII*** folding. Representative frequencies are highlighted by red dashed lines and labeled with red letters. The data were treated as described in figure 5.29.

The band assignment of the spectra in figure 5.30 is presented in table 5.4. *CrChR2* showed a similar band development as bR, i.e. a band shift from turn (1680 cm⁻¹) and random (1651 cm⁻¹) protein structures towards an α -helical signal (1660 cm⁻¹). This indicated a comparable secondary structure formation as identified for bR. A comparable but slightly different band development was observed for *HsSRI* and *HsSRII*. *HsSRII* did show the bands for turn (1680 cm⁻¹) and random (1650 cm⁻¹) structures too, but not a shift towards an α -helical signal, instead it shifted into the lower frequency range of

5. Results and Discussion

turn structures (1670 cm^{-1}). Although, *HsSRI* showed a band for turn structures (1678 cm^{-1}) in the same regime as bR, *CrChR2* and *HsSRII*, the signal for the random protein structure was not observed. Here, a band, interpreted as an α -helical structure (1660 cm^{-1}), increased in intensity synchronously with turn structure appearance. For amide II all of the proteins showed an increase of the corresponding band at $1551\text{--}1552\text{ cm}^{-1}$.

Table 5.4: Assignment of the bands indicated in figure 5.30: First hour.

Assignment	bR [cm^{-1}]	<i>CrChR2</i> [cm^{-1}]	<i>HsSRI</i> [cm^{-1}]	<i>HsSRII</i> [cm^{-1}]
Amide I:				
Turn	1678	1680	1678	1680 shift to 1670
Random	1651	1651	–	1650
α -helical	shift to 1661	shift to 1660	1660	
Amide II	1551	1552	1552	1552

In the late phase after one hour to ca. eight hours, an increase of the band intensities was observed (Fig. 5.31). Whereas amide II continued to increase, the amide I signal behaved differently for the different rhodopsins as compared to bR. For all three proteins the amide I signal did not shift to a prominent peak at approximately 1660 cm^{-1} , instead the peak maxima shifted towards lower frequencies of turn structures, apparently with multiple components interpreted from several shoulders at each peak. For the band assignment of the peak maxima see table 5.5. From these band shapes and much lower band intensities as compared to the bR folding process, an unfinished secondary structure formation was concluded.

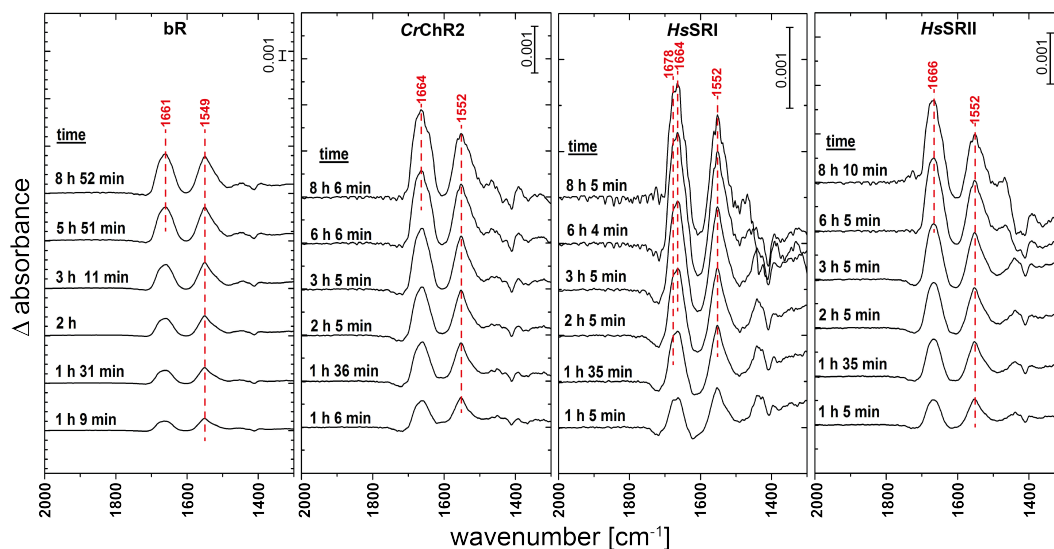


Figure 5.31: Background subtracted SEIRA spectra > 1 h after initialization of the folding experiments from **bR**, **CrChR2**, **HsSRI** and **HsSRII** folding. Representative frequencies are highlighted by red dashed lines and labeled with red letters. The data were treated as described in figure 5.29.

Table 5.5: Assignment of the bands indicated in figure 5.31: > 1 hour.

Assignment	bR [cm ⁻¹]	CrChR2 [cm ⁻¹]	HsSRI [cm ⁻¹]	HsSRII [cm ⁻¹]
Amide I:				
Turn	–	–	1678	–
	–	1664	1664	1666
α -helical	1661	–	–	–
Amide II	1549	1552	1552	1552

These preliminary data showed, that SEIRAS can be also used to investigate the folding process of other α -helical retinal transmembrane proteins and represent a further positive control for the bR folding experiment, since they showed comparable results for α -helical structure formation.

Chapter 6

Conclusion and Outlook

In this work membrane protein folding *in situ* under native conditions was investigated. Therefore, two rather novel methodologies were combined: nanodiscs technology in combination with cell-free protein expression and SEIRAS. Briefly, the nanodiscs were immobilized to a gold surface and overlaid with a cell-free protein expression system. By adding the coding DNA for a selected membrane protein, its transcription, translation and incorporation into the lipid support was initialized. The insertion and folding processes were investigated by the spectroscopic method SEIRAS.

Here, it could be shown, that it is possible to monitor the insertion and folding of the model protein bR, a seven α -helical transmembrane retinal protein into nanodiscs (illustrated in Fig. 6.1). During the first minutes after adding the DNA to the cell-free protein expression mix, adsorbed protein from the reaction mix was displaced from the surface bound nanodiscs (Fig. 6.1 pre-conditioning phase). Thereafter, the observations revealed a process in which turn and random protein structures converted into α -helices (Fig. 6.1 A) with subsequent condensation towards an α -helical bundle protein (Fig. 6.1 B). Control experiments verified, that the observed signals were associated with bR insertion and folding and not with protein adsorption from the protein expression mix or from bR which was nonspecifically associated with the nanodiscs. Because no translocons were used in this study, a co-translational insertion and folding pathway was assumed, which is also supported by other studies [53, 141].

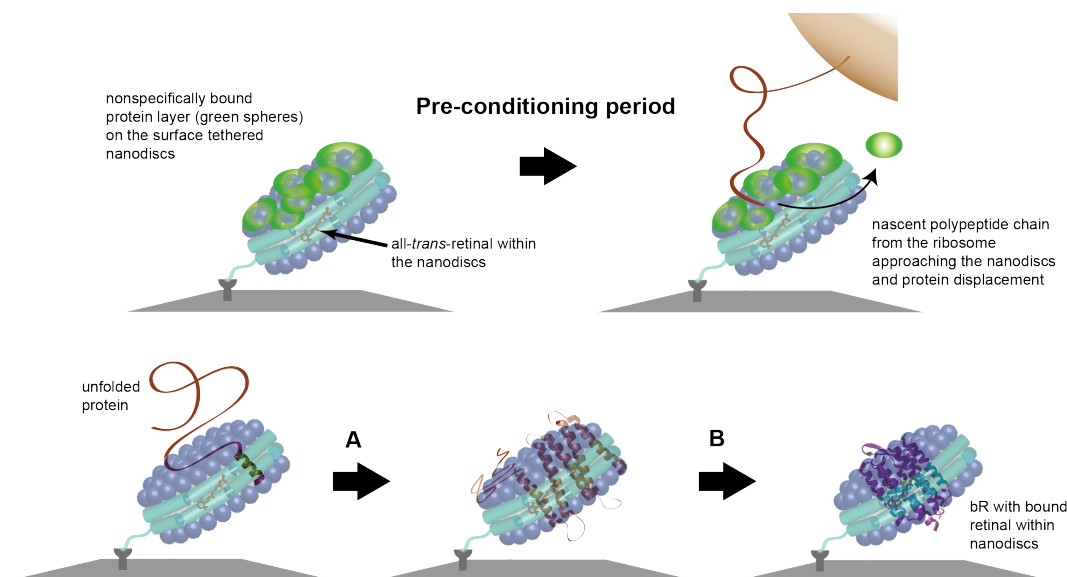


Figure 6.1: Folding model of bR deduced from the SEIRAS folding experiment described in this thesis. The figure was prepared using Adobe Illustrator CS5.

These results coincide with earlier reported observations from unfolding/refolding studies, which are outlined in the following. The general consensus of folding α -helical transmembrane proteins was based on experiments on bR and proposed by Engelman *et al.* [44], who described three folding stages. The first stage comprises the formation of α -helical transmembrane structures, the second, the interaction of these α -helices with each other and finally the third, possible partitioning of additional polypeptide regions, e.g. loops or turns, and co-factor binding. Additionally, Hunt *et al.* [135] suggested, that only if helix A to E are formed completely, the C-terminal peptide chain folds into the two helices F and G, which leads to the formation of the tertiary structure. The findings by Engelman and Hunt were supported by the groups of Müller and Gaub [136, 137], who extensively investigated the unfolding and refolding behavior of bR by atomic force microscopy (AFM) and SMFS. However, these studies did not probe folding in context of a native protein biosynthesis. This is different to the results reported here, which represent the first observation of incorporation and folding of a nascent polypeptide chain, i.e. part of a co-translational folding pathway.

However, although the function of cell-free expressed bR within nanodiscs was verified in batch experiments, a multitude of approaches to measure steady-state differences on the SEIRAS gold surface did not succeed. In the experiments executed here, most probably the sample concentration was too low. But on the other hand, also for purple membranes with much higher concentration

6. Conclusion and Outlook

of bR in the same set-up no steady-state differences could be observed. The same is true for halorhodopsin and channelrhodopsin 2 (personal communication with Dr. Kenichi Ataka, FU Berlin, Germany). According to Dr. Kenichi Ataka, one reason for the difficulties to record a steady-state difference spectrum might be an energy transfer from an very early light-activated retinal state to the plasmonic surface, which leads to the immediate relaxation back to the ground state without photocycle. This task remains most challenging and might be circumvented by changing the target protein to a protein, which can be easier tested after expression on the surface, e.g. enzymes.

In first experiments, the impact of the cofactor retinal on bR folding was investigated. It was shown, that the unhampered access to retinal is crucial for the final structure formation. In the absence of retinal, the folding process stopped, leaving the polypeptide in predominantly random and turn configuration instead of converting into mainly α -helices. This disagrees with the hypothesis, that the complete tertiary structure of bR is formed first before binding the co-factor [44]. Our experiments showed, that even if retinal was added during structure development, the folding process did not complete. In contrast, X-Ray crystallography experiments on retinal depleted membranes containing BO from *H. halobium* and a retinal free mutant of *H. halobium* (strain JW5) have shown, that it is possible to recover fully functional bR from BO by post-addition of retinal to the membranes [142]. Hence, the observed failure in recovering bR by late retinal addition in this thesis, might be explained by steric blockage of the components of the cell-free expression system which hinder the retinal reaching the BO inside the nanodiscs or the lipid composition in *H. salinarum* might be more favorable.

The pretreatment of nanodiscs with retinal, led to a much faster structure formation. However, it is not clear if this was a result of the more accessible retinal which is likely to accumulate in the lipid bilayer or of an increase in fluidity of the membrane due to the retinal, because experiments were executed at room temperature, which is beneath the phase transition temperature for the lipid DMPC. The same effect, faster insertion and folding of bR, has been observed when the temperature was increased to 37 °C probably leading to the transition towards liquid crystalline phase [140].

To clarify if retinal indeed influences the folding process by improving the fluidity of the membrane, in further experiments non-retinal proteins could be tested in the presence and in the absence of retinal. If there is an impact, significant differences in incorporation rates should be observable. To round up

the understanding of the retinal impact on bR, experiments should be repeated at 37 °C. If BO folding without retinal at 37 °C can be completed, the impact of retinal on folding due to a bilayer effect would be strongly indicated.

In preliminary folding experiments on *HsSRI*, *HsSRII* and the transmembrane region of *CrChR2* the extraordinary potential of SEIRAS even for the analysis of cell-free membrane protein expression was pointed out. For all three proteins no cell-free protein expression in batch was observed, leading to the question at which point the synthesis failed. By SEIRAS it was clarified, that all three proteins started to express and incorporate into (or approach) the nanodiscs, but at some point the folding process stopped.

Future approaches will address the optimization and improvement of the folding experiments that were started in this thesis. In this respect, the influence of different lipid compositions on the folding process should be tested as well as different biomimetic membrane systems, e.g. lipodiscs or solid supported bilayers (SLBs). Lipodiscs are disc-like lipid bilayers similar to nanodiscs but are stabilized by short polymers instead of scaffold proteins. Hence, the influence of amide I and II signals from the scaffold proteins could be completely eliminated. The same applies for a SLB which is a planar lipid bilayer sitting on a supporting surface. With SLBs all newly synthesized membrane proteins would orient equally to the surface plane. This would considerably ease secondary structure analysis. Furthermore, planar membranes are more suitable to include bigger target proteins or to provide space for protein complexes as nanodiscs cannot be enlarged unlimited. The bigger the discs the more instable they become [143,144]. However, SLB as well as lipodisc preparation are much more difficult and are not as reproducible as the assembly of nanodiscs. Another advantage of nanodiscs is that the expression and folding can be parallel carried out in batch under identical conditions, which acts as a control experiment for the SEIRAS one.

Another important task is the synchronization of the protein translation and folding process on the SEIRAS sample surface. The described methodology monitors events from an ensemble of molecules, however, it is favored to track single folding states as pure as possible. Optimally, all ribosomes should start and stop translation at the same time excluding retarded, asynchronous events. Synchronization could be achieved by starting the expression by the addition of methionine after all ribosomes had time to form complexes with mRNA. Another approach could be the usage of unnatural amino acids that are encoded in the beginning of the mRNA. Thereby, the ribosomes would

6. Conclusion and Outlook

start the expression but stop as soon the codon for the unnatural amino acids enter, leading to a hold of expression in all ribosomes. The addition of the corresponding tRNA to the cell-free expression mixture would continue the synthesis at the same time. A too early release of the mRNA from stalled ribosomes due to tmRNA might be a problem but could be circumvented by blocking it using anti-sense tmRNA. Unnatural amino acids can also be used to stop the protein synthesis at the C-terminal end of the protein. Additionally, polysome formation in the cell-free expression system is possible whose effect on the synchronization is hard to predict. However, addition of substances for the synchronization can simultaneously also disturb the reaction on the surface or at least the recording of the data. An optical switch for controlling the translation would be ideal, e.g. releasing caged compounds by light. However, corresponding techniques could not be found in the literature.

Besides the synchronization of the reaction process, protein engineering has proven to be of great importance in IR spectroscopic techniques [74]. For example Stark probes, which act as IR markers, could be introduced into to the nascent polypeptide chain. Thus, a specific change in the signal would be observed when this probe, e.g. is incorporated into the lipid bilayer, giving the opportunity to pinpoint folding events. Such markers normally contain bonds that absorb in an IR region where no protein bands occur, e.g C=N stretching vibrations.

A completely different way to assign folding events to specific polypeptide regions would be the use of truncated gene versions coding just for selected protein parts. We can even go further and allocate the importance of exclusive amino acids for defined folding events by introducing point mutations. In this context, AFM studies or hydrophobicity scale plots [145] can help identifying such potentially important amino acids.

Up to now our new approach was only used to study folding of α -helical proteins. It would be of great interest to observe also folding of a β -barrel membrane protein. Here, a huge translocational machinery is needed [146] as many of them are outer membrane proteins and are brought post-translationally into their destination membrane *in vivo*. As helper proteins play an important role, these molecules need to be included in the folding experiment, but will unfortunately give undesired signals, which might interfere with those from the folding process.

The here presented results on membrane protein folding are the first experiments, that show incorporation and folding events *in situ* during complete

protein biosynthesis in a non-invasive manner. These observations demonstrate the great potential of this methodology in membrane protein research.

Chapter 7

Summary

The correct folding and assembly of membrane proteins in biological membranes are preconditions for correct protein function and thus activity of a living cell. Not much is known about the fundamental principles of membrane protein folding under native conditions due to the difficulties to study such complex systems *in vivo* and *in operando*. Most existing studies investigate folding by unfolding/refolding a functional protein *in vitro*.

In this thesis, for the first time insertion and folding of a nascent membrane protein into a lipid bilayer was monitored during native protein biosynthesis. Therefore, SEIRAS, cell-free protein expression and nanodiscs were combined in a novel manner, which allowed the label-free and non-invasive investigation of insertion and folding of the retinal protein bR, a 7- α -helical transmembrane proton pump from *H. salinarum*. Protein synthesis was performed in an optical cell containing a prism covered with a thin gold film with nanodiscs on top, providing an biomimetic lipid bilayer for folding. Thereby, the folding was visualized by the transition of the nascent polypeptide chain from less ordered structure elements via secondary towards tertiary structure during co-translational bilayer insertion. In first experiments, the impact of the co-factor retinal on folding was probed and revealed its importance for folding speed and the structure formation process. Furthermore, by folding experiments on other α -helical proteins (*HsSRI*, *HsSRII* and the transmembrane region of *CrChR2*) the transferability of the technique was demonstrated.

Hence, the here described methodology represents a valuable approach to study membrane protein folding *in situ* and *in operando* on a molecular level to enlarge our understanding on fundamental folding principles.

Chapter 8

Zusammenfassung

Die richtige Faltung und Anordnung eines Membranproteins in seiner biologischen Membran ist Grundvoraussetzung für dessen Funktion und damit entsprechend der Zellaktivität. Das bisherige Verständnis über Membranproteinfaltung stützt sich auf Ergebnisse von Studien, die das Entfaltungs- und Rückfaltungsverhalten eines funktionalen Membranproteins untersuchen. Hingegen wenig ist bekannt über Faltung unter den natürlichen Bedingungen einer Proteinbiosynthese, maßgeblich aufgrund der außerordentlichen Schwierigkeit derartig komplexe Systeme *in vivo* und *in operando* untersuchen zu können.

Die Ergebnisse dieser Arbeit zeigen erstmalig Faltungsereignisse eines Membranproteins bei Insertion in eine Lipiddoppelschicht unter naturnahen Bedingungen. Dafür wurden oberflächenverstärkte Infrarotabsorptionsspektroskopie (SEIRAS), zellfreie Proteinexpression und Nanodiscs in einer neuartigen Weise kombiniert, sodass die Insertion und Faltung des Retinalproteins Bakteri-*rhodopsin* (bR) (eine 7- α -helikale transmembrane Protonenpumpe von *Halobacterium salinarum*), nichtinvasiv und ohne Modifikationen durch Markermoleküle, untersucht werden konnten. Die Proteinsynthese wurde dabei auf der Oberfläche einer optischen Zelle durchgeführt, die zuvor mit einem dünnen Goldfilm und einer Nanodiscmonolage beschichtet worden war. Die Nanodiscs stellten dabei die biomimetische Lipiddoppelschicht zur Faltung des Membranproteins dar. Es konnte ein Übergang von eher ungeordneten Proteinstrukturen über Sekundärstruktur- bis hin zur Tertiärstrukturbildung beobachtet werden, wodurch der Faltungsweg des Membranproteins sichtbar gemacht werden konnte, während es kotranslational in die Membran eingebaut wurde. Erste Experimente mit dem Kofaktor Retinal zeigten dessen wichtigen Einfluss auf den Faltungsprozess, Faltungsgeschwindigkeit und Strukturformation. Weitere Faltungsexperimente anderer α -helikaler Membranproteine (*HsSRI*, *HsSRII* und der Transmembranbereich von *CrChR2*) konnten die

8. Zusammenfassung

Übertragbarkeit der Technik demonstrieren.

Die hier beschriebene Methodik stellt einen wertvollen Untersuchungsansatz zur Membranproteinfaltung *in situ* und *in operando* auf molekularer Ebene dar und birgt großes Potential das bisherige Verständnis über fundamentale Faltungsprinzipien zu bereichern.

Bibliography

- [1] D. Nelson and M. Cox, Lehninger Biochemie, vol. 4. Springer-Verlag, 2009.
- [2] S. W. Englander and L. Mayne, “The nature of protein folding pathways,” Proceedings of the National Academy of Sciences, vol. 111, no. 45, pp. 15873–15880, 2014.
- [3] K. A. Dill and J. L. MacCallum, “The protein-folding problem, 50 years on,” Science, vol. 338, no. 6110, pp. 1042–1046, 2012.
- [4] C. B. Anfinsen, E. Haber, M. Sela, and F. H. White Jr., “The kinetics of formation of native ribonuclease during oxidation of the reduced polypeptide chain,” Proceedings of the National Academy of Sciences, vol. 47, September 1961.
- [5] C. B. Anfinsen, “Principles that govern the folding of protein chains,” Science, vol. 181, July 1973.
- [6] “C. B. Anfinsen. Nobel prize in chemistry 1972.” https://www.nobelprize.org/nobel_prizes/chemistry/laureates/1972/anfinsen-bio.html, May 2017.
- [7] D. Baker and D. A. Agard, “Kinetics versus thermodynamics in protein folding,” Biochemistry, vol. 33, no. 24, pp. 7505–7509, 1994.
- [8] K. A. Dill and H. S. Chan, “From levinthal to pathways to funnels,” Nat Struct Mol Biol, vol. 4, pp. 10–19, Jan. 1997.
- [9] C. Levinthal, “Are there pathways for protein folding?,” Extrait du Journal de Chimie Physique, vol. 65, no. 1, p. 44, 1968.
- [10] C. Levinthal, “How to fold graciously,” in Mossbauer spectroscopy in biological systems (P. DeBrunner, J. Tsibris, and E. Munck, eds.), (Urbana, IL), University of Illinois Press, 1969.

BIBLIOGRAPHY

- [11] L. Martinez, “Introducing the Levinthal’s protein folding paradox and its solution,” Journal of Chemical Education, vol. 91, pp. 1918 –1923, 2014.
- [12] R. L. Baldwin, “Matching speed and stability,” Nature, vol. 369, May 1994.
- [13] U. Ahluwalia, N. Katyal, and S. Deep, “Models of protein folding,” Journal of proteins and proteomics, vol. 3, no. 2, pp. 85–93, 2012.
- [14] C. M. Dobson, “Principles of protein folding, misfolding and aggregation,” Seminars in Cell & Developmental Biology, vol. 15, no. 1, pp. 3 – 16, 2004.
- [15] G. Karp, Cell and Molecular Biology: Concepts and Experiments. John Wiley and Sons, 2009.
- [16] J. U. Bowie, “Solving the membrane protein folding problem,” Nature, vol. 438, pp. 581–589, Dec. 2005.
- [17] “Classification of membrane proteins.” <http://www2.warwick.ac.uk/fac/sci/chemistry/research/dixon/dixongroup/members/msrhar/research/background/mp3.png>, April 2017.
- [18] C. M. Ott and V. R. Lingappa, “Integral membrane protein biosynthesis: why topology is hard to predict,” Journal of Cell Science, vol. 115, no. 10, pp. 2003–2009, 2002.
- [19] A. G. Lee, “How lipids affect the activities of integral membrane proteins,” Biochimica et Biophysica Acta (BBA) - Biomembranes, vol. 1666, no. 1 - 2, pp. 62 – 87, 2004.
- [20] S. H. White and W. C. Wimley, “Membrane protein folding and stability: Physical principles,” Annual Reviews of Biophysics and Biomolecular Structure, vol. 28, pp. 319–365, 1999.
- [21] F. Cymer, G. von Heijne, and S. H. White, “Mechanisms of integral membrane protein insertion and folding,” Journal of Molecular Biology, vol. 427, no. 5, pp. 999 – 1022, 2015.
- [22] J.-L. Popot and D. M. Engelman, “Membranes do not tell proteins how to fold,” Biochemistry, vol. 55, no. 1, pp. 5–18, 2016.

- [23] J. Heberle, "Proton transfer reactions across bacteriorhodopsin and along the membrane," Biochimica et Biophysica Acta (BBA) - Bioenergetics, vol. 1458, no. 1, pp. 135 – 147, 2000.
- [24] C. Wickstrand, R. Dods, A. Royant, and R. Neutze, "Bacteriorhodopsin: Would the real structural intermediates please stand up?," Biochimica et Biophysica Acta (BBA) - General Subjects, vol. 1850, no. 3, pp. 536 – 553, 2015.
- [25] U. Zander, G. Bourenkov, A. N. Popov, D. de Sanctis, O. Svensson, A. A. McCarthy, E. Round, V. Gordeliy, C. Mueller-Dieckmann, and G. A. Leonard, "MeshAndCollect: an automated multi-crystal data-collection workflow for synchrotron macromolecular crystallography beamlines," Acta Crystallographica Section D, vol. 71, pp. 2328–2343, Nov 2015.
- [26] J. K. Lanyi, "Understanding structure and function in the light-driven proton pump bacteriorhodopsin," Journal of Structural Biology, vol. 124, no. 2-3, pp. 164–178, 1998.
- [27] A. Maeda, "Application of FTIR spectroscopy to the structural study on the function of bacterioopsin," Israel Journal of Chemistry, vol. 35, pp. 387–400, 1995.
- [28] U. Haupts, J. Tittor, and D. Oesterhelt, "Closing in on bacterioopsin: Progress in understanding the molecule," Annual Review of Biophysics and Biomolecular Structure, vol. 28, pp. 367–99, 1999.
- [29] "Bacteriorhodopsin." <http://microbiochem.weebly.com/bacteriorhodopsin.html>, Mai 2016.
- [30] "The photocycle of bacteriorhodopsin." <https://www.psi.ch/swissfel/the-photocycle-of-bacteriorhodopsin>, Mai 2016.
- [31] K. Edman, P. Nollert, A. Royant, H. Belrhali, E. Pebay-Peyroula, J. Hajdu, R. Neutze, and E. M. Landau, "High-resolution x-ray structure of an early intermediate in the bacteriorhodopsin photocycle," Nature, vol. 401, pp. 822–826, Oct. 1999.
- [32] M. Andersson, E. Malmerberg, S. Westenhoff, G. Katona, M. Cammarata, A. B. Wöhri, L. C. Johansson, F. Ewald, M. Eklund, M. Wulff, J. Davidsson, and R. Neutze, "Structural dynamics of light-driven proton pumps," Structure, vol. 17, no. 9, pp. 1265 – 1275, 2009.

BIBLIOGRAPHY

- [33] J. K. Lanyi, "Bacterioopsin," *Biochimica et Biophysica Acta*, vol. 1460, pp. 1 – 3, 2000.
- [34] "Bacteriorhodopsin." https://www.biochem.mpg.de/523002/Protein_BR, April 2017.
- [35] J. L. Spudich, D. N. Zacks, and R. A. Bogomolni, "Microbial sensory rhodopsins: Photochemistry and function," *Israel Journal of Chemistry*, vol. 35, pp. 495 –513, 1995.
- [36] O. S. Mironova, I. L. Budyak, G. Bueldt, R. Schlesinger, and J. Heberle, "FT-IR difference spectroscopy elucidates crucial interactions of sensory rhodopsin i with the cognate transducer Htr I," *Biochemistry*, vol. 46, pp. 9399–9405, 2007.
- [37] O. S. Mironova, R. G. Efremov, B. Person, J. Heberle, I. L. Budyak, G. Bueldt, and R. Schlesinger, "Functional characterization of sensory rhodopsin II from *Halobacterium salinarum* expressed in *Escherichia coli*," *FEBS Letters*, vol. 579, pp. 3147–3151, 2005.
- [38] F. Schneider, C. Grimm, and P. Hegemann, "Biophysics of channel-rhodopsin," *Annual Review of Biophysics*, vol. 44, pp. 167 – 86, 2015.
- [39] Y. Gu, H. Li, H. Dong, Y. Zeng, Z. Zhang, N. G. Paterson, P. J. Stansfeld, Z. Wang, Y. Zhang, W. Wang, and C. Dong, "Structural basis of outer membrane protein insertion by the BAM complex," *Nature*, vol. 531, pp. 64–69, Mar. 2016.
- [40] L. Han, J. Zheng, Y. Wang, X. Yang, Y. Liu, C. Sun, B. Cao, H. Zhou, D. Ni, J. Lou, Y. Zhao, and Y. Huang, "Structure of the bam complex and its implications for biogenesis of outer-membrane proteins," *Nat Struct Mol Biol*, vol. 23, pp. 192–196, Mar. 2016.
- [41] R. E. Jacobs and S. H. White, "The nature of the hydrophobic binding of small peptides at the bilayer interface: implications for the insertion of transbilayer helices," *Biochemistry*, vol. 28, no. 8, pp. 3421–3437, 1989.
- [42] J. L. Popot and D. M. Engelman, "Membrane protein folding and oligomerization: the two-stage model," *Biochemistry*, vol. 29, no. 17, pp. 4031–4037, 1990.

- [43] K.-S. Huang, H. Bayley, M.-J. Liao, E. London, and H. G. Khorana, "Refolding of an integral membrane protein. denaturation, renaturation, and reconstitution of intact bacteriorhodopsin and two proteolytic fragments," The Journal of Biological Chemistry, vol. 256, pp. 3802–3809, April 1981.
- [44] D. M. Engelman, Y. Chen, C.-N. Chin, A. Curran, A. M. Dixon, A. D. Dupuy, A. S. Lee, U. Lehnert, E. E. Matthews, Y. K. Reshetnyak, A. Senes, and J.-L. Popot, "Membrane protein folding: beyond the two stage model," FEBS Letters, vol. 555, no. 1, pp. 122–125, 2003.
- [45] P. J. Booth, "Unravelling the folding of bacteriorhodopsin," Biochimica et Biophysica Acta (BBA) - Bioenergetics, vol. 1460, no. 1, pp. 4 – 14, 2000.
- [46] R. Petrosyan, C. A. Bippes, S. Walheim, D. Harder, D. Fotiadis, T. Schimmel, D. Alsteens, and D. J. Müller, "Single-molecule force spectroscopy of membrane proteins from membranes freely spanning across nanoscopic pores," Nano Letters, vol. 15, no. 5, pp. 3624–3633, 2015.
- [47] P. G. Wolynes, "Evolution, energy landscapes and the paradoxes of protein folding," Biochimie, vol. 119, pp. 218 – 230, 2015.
- [48] E. A. Roman and F. L. González Flecha, "Kinetics and thermodynamics of membrane protein folding," Biomolecules, vol. 4, no. 1, pp. 354–373, 2014.
- [49] P. J. Booth, "The trials and tribulations of membrane protein folding in vitro," Biochimica et Biophysica Acta (BBA) - Biomembranes, vol. 1610, no. 1, pp. 51 – 56, 2003.
- [50] P. J. Booth and J. Clarke, "Membrane protein folding makes the transition," Proceedings of the National Academy of Sciences of the United States of America, vol. 107, pp. 3947–3948, Feb. 2010.
- [51] S. H. White and W. C. Wimley, "Hydrophobic interactions of peptides with membrane interfaces," Biochimica et Biophysica Acta (BBA) - Reviews on Biomembranes, vol. 1376, no. 3, pp. 339 – 352, 1998.
- [52] K. A. Dill, S. B. Ozkan, M. S. Shell, and T. R. Weikl, "The protein folding problem," Annual review of biophysics, vol. 37, pp. 289–316, June 2008.

BIBLIOGRAPHY

- [53] H. Dale and M. P. Krebs, “Membrane insertion kinetics of a protein domain in vivo: The bacterioopsin N-Terminus inserts co-translationally,” The Journal of Biological Chemistry, vol. 274, pp. 22693 – 22698, 8 1999.
- [54] T. H. Bayburt, Y. V. Grinkova, and S. G. Sligar, “Self-assembly of discoidal phospholipid bilayer nanoparticles with membrane scaffold proteins,” Nano Letters, vol. 2, no. 8, pp. 853–856, 2002.
- [55] S. G. Sligar, “Finding a single-molecule solution for membrane proteins,” Biochemical and Biophysical Research Communications, vol. 312, pp. 115–119, 2003.
- [56] A. Nath, W. M. Atkins, and S. G. Sligar, “Applications of phospholipid bilayer nanodiscs in the study of membranes and membrane proteins,” Biochemistry, vol. 46, no. 8, pp. 2059–2069, 2007.
- [57] S. G. Sligar, “Nanodisc technology.” <http://sligarlab.life.uiuc.edu/nanodisc.html>, September 2014.
- [58] “Lipoproteins and nanodiscs.” <http://www.ks.uiuc.edu/Research/Lipoproteins/>, April 2016.
- [59] S. G. Sligar, “Nanodisc technology/ sequences.” <http://sligarlab.life.uiuc.edu/nanodisc/sequences.html>, Mai 2016.
- [60] C. G. Brouillette, G. Anantharamaiah, J. A. Engler, and D. W. Borhani, “Structural models of human apolipoprotein A-I: a critical analysis and review,” Biochimica et Biophysica Acta (BBA) - Molecular and Cell Biology of Lipids, vol. 1531, no. 1 - 2, pp. 4 – 46, 2001.
- [61] T. H. Bayburt and S. G. Sligar, “Self-assembly of single integral membrane proteins into soluble nanoscale phospholipid bilayers,” Protein Science, vol. 12, no. 11, pp. 2476–2481, 2003.
- [62] J. Borch and T. Hamann, “The nanodisc: a novel tool for membrane protein studies,” Biol. Chem., vol. 390, pp. 805–814, August 2009.
- [63] A. Zemella, L. Thoring, C. Hoffmeister, and S. Kubick, “Cell-free protein synthesis: Pros and cons of prokaryotic and eukaryotic systems,” ChemBioChem, vol. 16, no. 17, pp. 2420–2431, 2015.

- [64] F. Katzen, G. Chang, and W. A. Kudlicki, "The past, present and future of cell-free protein synthesis," Trends in Biotechnology, vol. 23, pp. 150–156, March 2005.
- [65] E. D. Carlson, R. Gan, C. E. Hodgman, and M. C. Jewett, "Cell-free protein synthesis: Applications come of age," Biotechnology Advances, vol. 30, no. 5, pp. 1185 – 1194, 2012.
- [66] C. E. Hodgman and M. C. Jewett, "Cell-free synthetic biology: Thinking outside the cell," Metabolic Engineering, vol. 14, no. 3, pp. 261 – 269, 2012.
- [67] G. Rosenblum and B. S. Cooperman, "Engine out of the chassis: Cell-free protein synthesis and its uses," FEBS Letters, vol. 588, no. 2, pp. 261–268, 2014.
- [68] Y. Shimizu, A. Inoue, Y. Tomari, T. Suzuki, T. Yokogawa, K. Nishikawa, and T. Ueda, "Cell-free translation reconstituted with purified components," Nat Biotech, vol. 19, pp. 751 – 755, 2001.
- [69] R. Sachse, S. K. Dondapati, S. F. Fenz, T. Schmidt, and S. Kubick, "Membrane protein synthesis in cell-free systems: From bio-mimetic systems to bio-membranes," FEBS Letters, vol. 588, no. 17, pp. 2774–2781, 2014.
- [70] D. Schwarz, V. Dötsch, and F. Bernhard, "Production of membrane proteins using cell-free expression systems," PROTEOMICS, vol. 8, no. 19, pp. 3933–3946, 2008.
- [71] N. Shadiac, Y. Nagarajan, S. Waters, and M. Hrmova, "Close allies in membrane protein research: Cell-free synthesis and nanotechnology," MOLECULAR MEMBRANE BIOLOGY, vol. 30, pp. 229–245, MAY 2013.
- [72] F. Katzen, J. E. Fletcher, J.-P. Yang, D. Kang, T. C. Peterson, J. A. Cappuccio, C. D. Blanchette, T. Sulchek, B. A. Chromy, P. D. Hoeplich, M. A. Coleman, and W. Kudlicki, "Insertion of membrane proteins into discoidal membranes using a cell-free protein expression approach," Journal of Proteome Research, vol. 7, pp. 3535–3542, 2008.
- [73] "Horiba scientific - raman spectroscopy."
<http://www.horiba.com/scientific/products/>

BIBLIOGRAPHY

- raman-spectroscopy/raman-academy/raman-faqs/
what-laser-wavelengths-are-used-for-raman-spectroscopy/,
July 2017.
- [74] F. Siebert and P. Hildebrandt, Vibrational Spectroscopy in Life Science. Wiley-VCH Verlag GmbH, 2008.
- [75] P. R. Griffith and J. A. de Haseth, Fourier Transform Infrared Spectroscopy. Wiley-VCH Verlag GmbH, 2007.
- [76] A. Barth and C. Zscherp, "What vibrations tell us about proteins," Quarterly Reviews of Biophysics, vol. 35, pp. 369–430, 2002.
- [77] P. W. Atkins, Physikalische Chemie. WILEY-VCH Verlag, 3., korr. Aufl. ed., 2001.
- [78] Universität zu Köln, Lehrstuhl für Physikalische Chemie, "Physikalisch Chemisches Praktikum für Fortgeschrittene - IR-Spektroskopie." Praktikumsskript, 2007.
- [79] W. Göpel and C. Ziegler, Struktur der Materie: Grundlagen, Mikroskopie und Spektroskopie. B.G. Teubner Verlagsgesellschaft, 1994.
- [80] S. Krimm and J. Bandekar, Advances in protein chemistry - Vibrational spectroscopy and conformation of peptides, polypeptides and proteins. Academic Press, Inc., 1986.
- [81] S. Kerruth, "Oberflächenverstärkte FT-IR und Raman Spectroskopie am Photoactive Yellow Protein," Master's thesis, University Bielefeld, 2010.
- [82] R. F. Aroca, D. J. Ross, and C. Domingo, "Surface-enhanced infrared spectroscopy," Appl. Spectrosc., vol. 58, pp. 324A–338A, Nov 2004.
- [83] M. Osawa, Handbook of Vibrational Spectroscopy. Wiley-VCH Verlag GmbH, 2006.
- [84] M. Fleischmann, P. Hendra, and A. McQuillan, "Raman spectra of pyridine adsorbed at a silver electrode," Chemical Physics Letters, vol. 26, no. 2, pp. 163 – 166, 1974.
- [85] D. L. Jeanmaire and R. P. van Duyne, "Surface Raman Spectroelectrochemistry, Part I. Heterocyclic, aromatic, and aliphatic amines adsorbed on the anodized silver electrode," J. Electroanal. Chem., vol. 84, pp. 1–20, 1977.

- [86] M. G. Albrecht and J. A. Creighton, "Anomalously intense raman spectra of pyridine at a silver electrode," Journal of the American Chemical Society, vol. 99, no. 15, pp. 5215–5217, 1977.
- [87] A. Hartstein, J. R. Kirtley, and J. C. Tsang, "Enhancement of the infrared absorption from molecular monolayers with thin metal overlayers," Phys. Rev. Lett., vol. 45, pp. 201–204, Jul 1980.
- [88] A. Hatta, T. Ohshima, and W. Suëtaka, "Observation of the enhanced infrared absorption of p-nitrobenzoate on Ag island films with an ATR technique," Applied Physics A, vol. 29, no. 2, pp. 71–75, 1982.
- [89] M. Osawa, "Dynamic processes in electrochemical reactions studied by surface-enhanced infrared absorption spectroscopy (SEIRAS)," Bulletin of the Chemical Society of Japan, vol. 70, no. 12, pp. 2861–2880, 1997.
- [90] T. R. Jensen, R. P. V. Duyne, S. A. Johnson, and V. A. Maroni, "Surface-enhanced infrared spectroscopy: A comparison of metal island films with discrete and nondiscrete surface plasmons," Appl. Spectrosc., vol. 54, pp. 371–377, Mar 2000.
- [91] A. Hatta, Y. Suzuki, and W. Suëtaka, "Infrared absorption enhancement of monolayer species on thin evaporated Ag films by use of a Kretschmann configuration: Evidence for two types of enhanced surface electric fields," Applied Physics A, vol. 35, no. 3, pp. 135–140, 1984.
- [92] A. Hatta, Y. Chiba, and W. Suëtaka, "Infrared absorption study of adsorbed species at metal/water interface by use of the Kretschmann configuration," Surface Science, vol. 158, no. 1-3, pp. 616–623, 1985.
- [93] T. Kamata, A. Kato, J. Umemura, and T. Takenaka, "Intensity enhancement of infrared attenuated total reflection spectra of stearic acid Langmuir-Blodgett monolayers with evaporated silver island films," Langmuir, vol. 3, no. 6, pp. 1150–1154, 1987.
- [94] M. Osawa, M. Kuramitsu, A. Hatta, W. Suëtaka, and H. Seki, "Electromagnetic effect in enhanced infrared absorption of adsorbed molecules on thin metal films," Surface Science, vol. 175, no. 3, pp. L787 – L793, 1986.

BIBLIOGRAPHY

- [95] M. Osawa and W. Suëtaka, "Surface enhanced raman scattering on evaporated silver films: The importance of short-ranged electromagnetic fields in the film," Surface Science, vol. 186, no. 3, pp. 583 – 600, 1987.
- [96] M. Osawa and M. Ikeda, "Surface-enhanced infrared absorption of p-nitrobenzoic acid deposited on silver island films: contributions of electromagnetic and chemical mechanisms," The Journal of Physical Chemistry, vol. 95, no. 24, pp. 9914–9919, 1991.
- [97] M. Osawa and K. Ataka, "Electromagnetic mechanism of enhanced infrared absorption of molecules adsorbed on metal island films," Surface Science, vol. 262, no. 3, pp. L118 – L122, 1992.
- [98] M. Osawa, K.-I. Ataka, K. Yoshii, and Y. Nishikawa, "Surface-enhanced infrared spectroscopy: The origin of the absorption enhancement and band selection rule in the infrared spectra of molecules adsorbed on fine metal particles," Appl. Spectrosc., vol. 47, pp. 1497–1502, Sep 1993.
- [99] R. K. Chang and T. E. Furtak, eds., Surface Enhanced Raman Scattering. Plenum Press, New York, 1982.
- [100] R. S. Sennett and G. D. Scott, "The structure of evaporated metal films and their optical properties," Journal of the Optical Society of America, vol. 40, pp. 203–211, 1950.
- [101] I. G. Denisov, Y. V. Grinkova, A. A. Lazarides, and S. G. Sligar, "Directed self-assembly of monodisperse phospholipid bilayer nanodiscs with controlled size," Journal of the American Chemical Society, vol. 126, no. 11, pp. 3477–3487, 2004.
- [102] G. Candiano, M. Bruschi, L. Musante, L. Santucci, G. M. Ghiggeri, B. Carnemolla, P. Orecchia, L. Zardi, and P. G. Righetti, "Blue silver: A very sensitive colloidal coomassie g-250 staining for proteome analysis," ELECTROPHORESIS, vol. 25, no. 9, pp. 1327–1333, 2004.
- [103] P. Artimo, M. Jonnalagedda, K. Arnold, D. Baratin, G. Csardi, E. de Castro, S. Duvaud, V. Flegel, A. Fortier, E. Gasteiger, A. Grosdidier, C. Hernandez, V. Ioannidis, D. Kuznetsov, R. Liechti, S. Moretti, K. Mostaguir, N. Redaschi, G. Rossier, I. Xenarios, and H. Stockinger, "ExpASY: SIB bioinformatics resource portal," Nucleic Acids Research, vol. 40, no. W1, p. W597, 2012.

- [104] H. M. Berman, J. Westbrook, Z. Feng, G. Gilliland, T. N. Bhat, H. Weissig, I. N. Shindyalov, and P. E. Bourne, “The protein data bank,” Nucleic Acids Research, vol. 28, pp. 235–242, Oct. 1999.
- [105] D. Hanahan, “Studies on transformation of *E. coli* with plasmids,” J. Mol. Biol., 1983.
- [106] D. Hanahan, DNA cloning, a practical approach, vol. 1, ch. Techniques for transformation of *E. coli*, pp. 109–135. IRL Press, 1985.
- [107] H. Schaegger and G. von Jagow, “Tricine-sodium dodecyl sulfate-polyacrylamide gel electrophoresis for the separation of proteins in the range from 1 to 100 kDa,” Analytical Biochemistry, vol. 166, no. 2, pp. 368 – 379, 1987.
- [108] Agilent Technologies, USA, QuikChange Site-Directed Mutagenesis Kit, 2017. 200518-12.
- [109] Invitrogen™ | Thermo Fisher Scientific Inc., MembraneMax™ HN protein expression kit - For expression of recombinant membrane proteins in a cell-free protein synthesis system, man0000697 ed., April 2012. Publication Part Number A10604.
- [110] “Nanodisc technology.” <http://sligarlab.life.uiuc.edu/nanodisc/sequences.html>, May 2018.
- [111] M. Roos, “Expression and purification of MSP1/MSP1E3D1.” Protocol from personal communication, 2012.
- [112] M. Roos, “Nanodisc assembly.” Protocol from personal communication, 2012.
- [113] New England Biolabs GmbH, Germany, PURExpress® In Vitro Protein Synthesis kit E6800S. Version 2.1 10/12.
- [114] E. Kretschmann, “Decay of non radiative surface plasmons into light on rough silver films. Comparison of experimental and theoretical results,” Optics Communications, vol. 6, no. 2, pp. 185 – 187, 1972.
- [115] Korth Kristalle GmbH, “Silizium (Si).” <http://www.korth.de/index.php/material-detailansicht/items/32.html>, February 2015.

BIBLIOGRAPHY

- [116] Spektrum Akademischer Verlag, “Brechzahl.” <http://www.spektrum.de/lexikon/physik/brechzahl/1958>, February 2015.
- [117] K. Ataka and J. Heberle, “Biochemical applications of surface-enhanced infrared absorption spectroscopy,” Anal Bioanal Chem, vol. 388, pp. 47–54, 2007.
- [118] K. Ataka, F. Giess, W. Knoll, R. Naumann, S. Haber-Pohlmeier, B. Richter, and J. Heberle, “Oriented attachment and membrane reconstitution of his-tagged cytochrome c oxidase to a gold electrode: In situ monitoring by surface-enhanced infrared absorption spectroscopy,” Journal of the American Chemical Society, vol. 126, no. 49, pp. 16199–16206, 2004.
- [119] K. Ataka, S. T. Stripp, and J. Heberle, “Surface-enhanced infrared absorption spectroscopy (SEIRAS) to probe monolayers of membrane proteins,” Biochimica et Biophysica Acta (BBA) - Biomembranes, vol. 1828, no. 10, pp. 2283 – 2293, 2013.
- [120] J. Heberle, J. Fitter, H. J. Sass, and G. Büldt, “Bacteriorhodopsin: the functional details of a molecular machine are being resolved,” Biophysical chemistry, vol. 85, no. 2, pp. 229–248, 2000.
- [121] K. J. Rothschild, “FTIR difference spectroscopy of bacteriorhodopsin: Toward a molecular model,” Journal of Bioenergetics and Biomembranes, vol. 24, no. 1, 1992.
- [122] J. Chalmers and P. Griffiths, eds., Handbook of Vibrational Spectroscopy. Wiley, 2002.
- [123] M. Engelhard, K. D. Kohl, B. Hess, J. Heidemeier, M. Fischer, and F. Parak, “The photocycle and the structure of iron containing bacteriorhodopsin - a kinetic and Moessbauer spectroscopy investigation,” European Biophysics Journal With Biophysics Letters, vol. 19, 1990.
- [124] S. Ldr, U. Sharma, and R. No, “M. Tech Credit Seminar Report, Electronic Systems Group, EE Dept, IIT Bombay submitted Oct 04 INFRARED DETECTORS,” 2004.
- [125] A. Rogalski, “HgCdTe infrared detector material: history, status and outlook,” Reports on Progress in Physics, vol. 68, no. 10, p. 2267, 2005.

- [126] Y. Zou and G. Ma, “A New Criterion to Evaluate Water Vapor Interference in Protein Secondary Structural Analysis by FTIR Spectroscopy,” International Journal of Molecular Sciences, vol. 15, no. 6, p. 10018, 2014.
- [127] D. J. Müller, F. A. Schabert, G. Büldt, and A. Engel, “Imaging purple membranes in aqueous solutions at sub-nanometer resolution by atomic force microscopy,” Biophysical Journal, vol. 68, pp. 1681–1686, May 1995.
- [128] K. Shimono, M. Goto, T. Kikukawa, S. Miyauchi, M. Shirouzu, N. Kamo, and S. Yokoyama, “Production of functional bacteriorhodopsin by an escherichia coli cell-free protein synthesis system supplemented with steroid detergent and lipid,” Protein Science, vol. 18, no. 10, pp. 2160–2171, 2009.
- [129] N. Dencher and M. Heyn, “Formation and properties of bacteriorhodopsin monomers in the non-ionic detergents octyl-beta-D-glucoside and triton X-100,” FEBS Letters, vol. 96, no. 2, pp. 322–326, 1978.
- [130] V. I. Gordeliy, R. Schlesinger, R. Efremov, G. Büldt, and J. Heberle, Crystallization in Lipidic Cubic Phases, pp. 305–316. Totowa, NJ: Humana Press, 2003.
- [131] E. Zaitseva, M. Saavedra, S. Banerjee, T. P. Sakmar, and R. Vogel, “SEIRA spectroscopy on a membrane receptor monolayer using lipoprotein particles as carriers,” Biophysical Journal, vol. 99, no. 7, pp. 2327 – 2335, 2010.
- [132] A. Baumann, S. Kerruth, J. Fitter, G. Büldt, J. Heberle, R. Schlesinger, and K. Ataka, “In-situ observation of membrane protein folding during cell-free expression,” PLoS ONE, vol. 11, pp. 1–15, 03 2016.
- [133] “Jena library of biological macromolecules.” http://jenalib.leibniz-fli.de/ImgLibDoc/ftir/IMAGE_FTIR.html, May 2017.
- [134] E.-L. Karjalainen and A. Barth, “Vibrational coupling between helices influences the amide i infrared absorption of proteins: Application to bacteriorhodopsin and rhodopsin,” The Journal of Physical Chemistry B, vol. 116, no. 15, pp. 4448–4456, 2012.

BIBLIOGRAPHY

- [135] J. F. Hunt, T. N. Earnest, O. Bousché, K. Kalghatgi, K. Reilly, C. Horváth, K. J. Rothschild, , and D. M. Engelman, “A biophysical study of integral membrane protein folding,” Biochemistry, vol. 36, no. 49, pp. 15156–15176, 1997.
- [136] M. Kessler, K. E. Gottschalk, H. Janovjak, D. J. Muller, and H. E. Gaub, “Bacteriorhodopsin folds into the membrane against an external force,” Journal of molecular biology, vol. 357, pp. 644 – 654, March 2006.
- [137] M. Kessler and H. E. Gaub, “Unfolding barriers in bacteriorhodopsin probed from the cytoplasmic and the extracellular side by AFM,” Structure, vol. 14, no. 3, pp. 521 – 527, 2006.
- [138] X. Jiang, E. Zaitseva, M. Schmidt, F. Siebert, M. Engelhard, R. Schlesinger, K. Ataka, R. Vogel, and J. Heberle, “Resolving voltage-dependent structural changes of a membrane photoreceptor by surface-enhanced ir difference spectroscopy,” Proceedings of the National Academy of Sciences, vol. 105, no. 34, pp. 12113–12117, 2008.
- [139] P. Curnow, N. D. Di Bartolo, K. M. Moreton, O. O. Ajoje, N. P. Saggese, and P. J. Booth, “Stable folding core in the folding transition state of an alpha-helical integral membrane protein,” Proceedings of the National Academy of Sciences, vol. 108, no. 34, pp. 14133–14138, 2011.
- [140] L. Grzegorzewski, “In-situ surface enhanced IR study of membrane protein folding during cell-free expression,” Master’s thesis, Freie Universität Berlin, 2017.
- [141] R. Kalmbach, I. Chizhov, M. C. Schumacher, T. Friedrich, E. Bamberg, and M. Engelhard, “Functional cell-free synthesis of a seven helix membrane protein: In situ insertion of bacteriorhodopsin into liposomes,” Journal of Molecular Biology, vol. 371, no. 3, pp. 639 – 648, 2007.
- [142] M. Birkholz, “Untersuchung zur Bildung des zweidimensionalen Gitters in der Purpormembran des Halobakterium Halobium,” Master’s thesis, Freie Universität Berlin, 1986.
- [143] I. G. Denisov and S. G. Sligar, “Nanodiscs in membrane biochemistry and biophysics,” Chemical Reviews, vol. 117, no. 6, pp. 4669–4713, 2017.
- [144] Y. V. Grinkova, I. G. Denisov, and S. G. Sligar, “Engineering extended membrane scaffold proteins for self-assembly of soluble nanoscale lipid

- bilayers,” Protein Engineering, Design and Selection, vol. 23, no. 11, pp. 843–848, 2010.
- [145] “Hydrophobicity scale plots.” http://blanco.biomol.uci.edu/hydrophobicity_scales.html, July 2017.
- [146] X. C. Zhang and L. Han, “How does a β -barrel integral membrane protein insert into the membrane?,” Protein & Cell, vol. 7, pp. 471–477, Jul 2016.

BIBLIOGRAPHY

List of publications

Baumann A, Kerruth S, Fitter J, Büldt G, Heberle J, Schlesinger R, et al. (2016) In-Situ Observation of Membrane Protein Folding during Cell-Free Expression. PLoS ONE 11(3): e0151051. <https://doi.org/10.1371/journal.pone.0151051>

Appendix A

Supplementary IR spectra

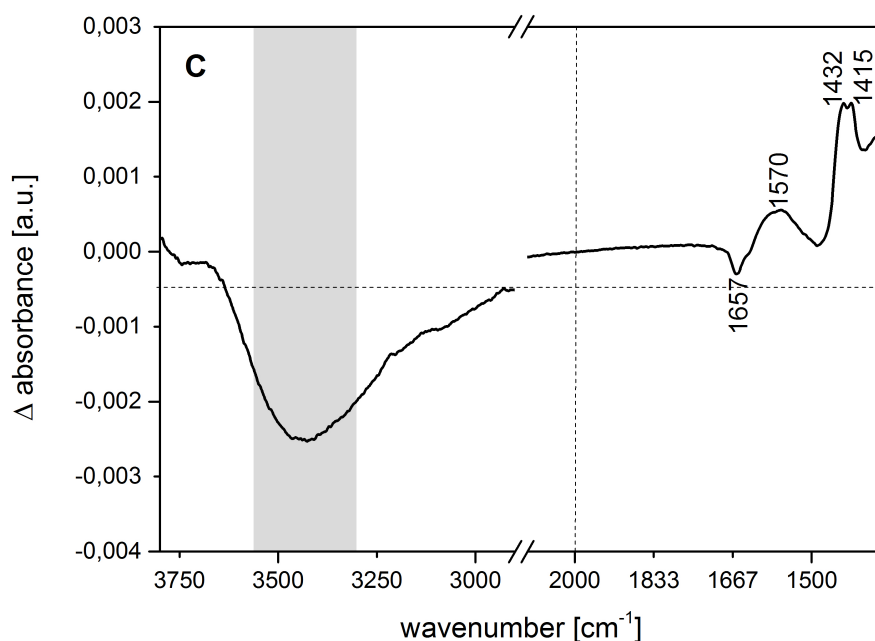


Figure A.1: Background subtracted SEIRA spectrum of the NTA monolayer changed by the nickel chelation, with a negative signal at 1657 cm^{-1} and in the regime around 3400 cm^{-1} (gray shaded area) assigned to desorption of water caused by Nickel ion adsorption (i.e. binding), at 1570 cm^{-1} for asymmetric and at 1432 and 1415 cm^{-1} for symmetric stretching vibrations of the carboxylate groups.

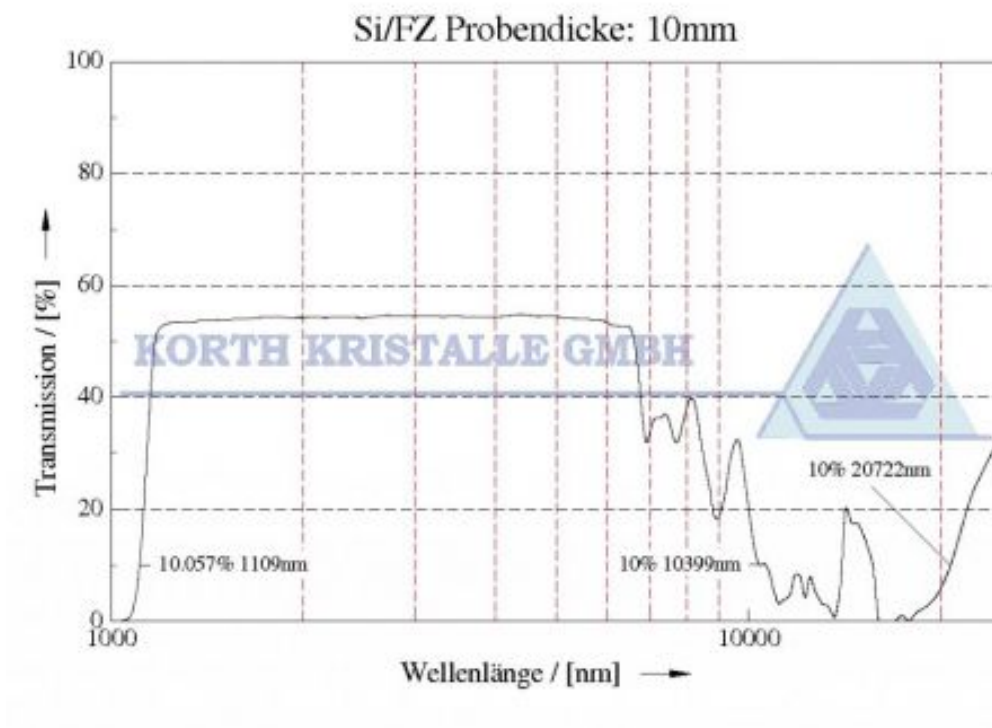


Figure A.2: Transmission spectrum of the Si-prism (property of KORTH KRISTALLE GmbH)

Appendix B

Plasmids and protein constructs

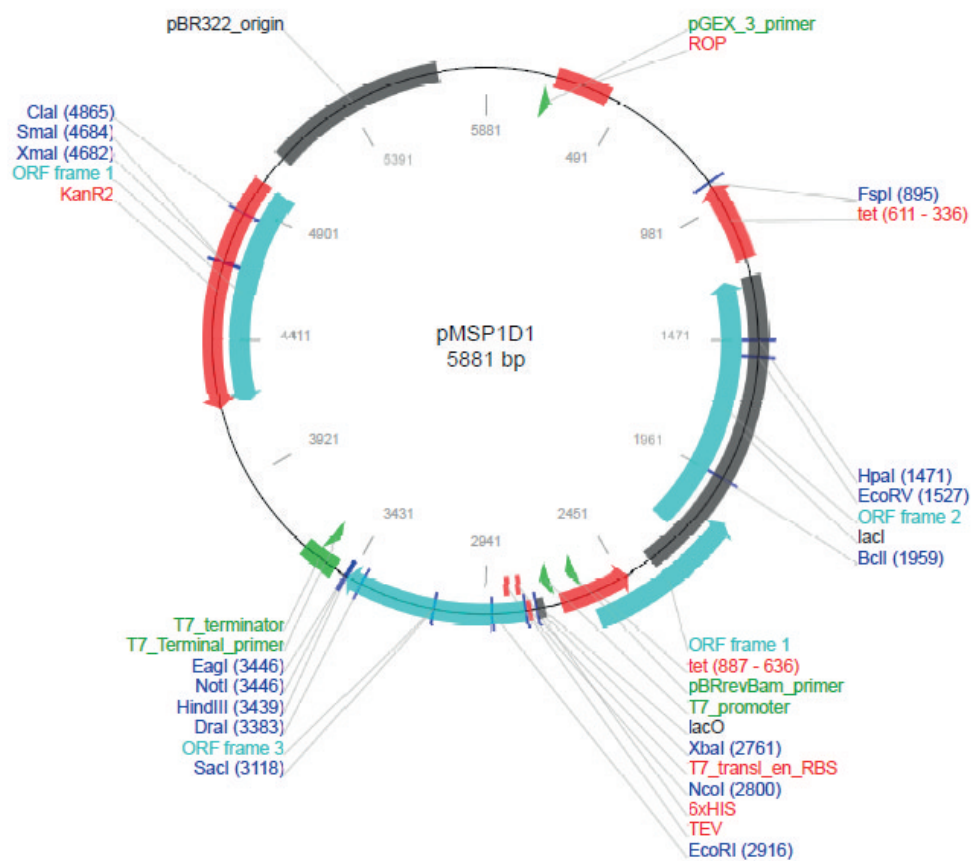


Figure B.1: Plasmid map pMSP1D1 from Addgene Inc., USA.

B. Plasmids and protein constructs

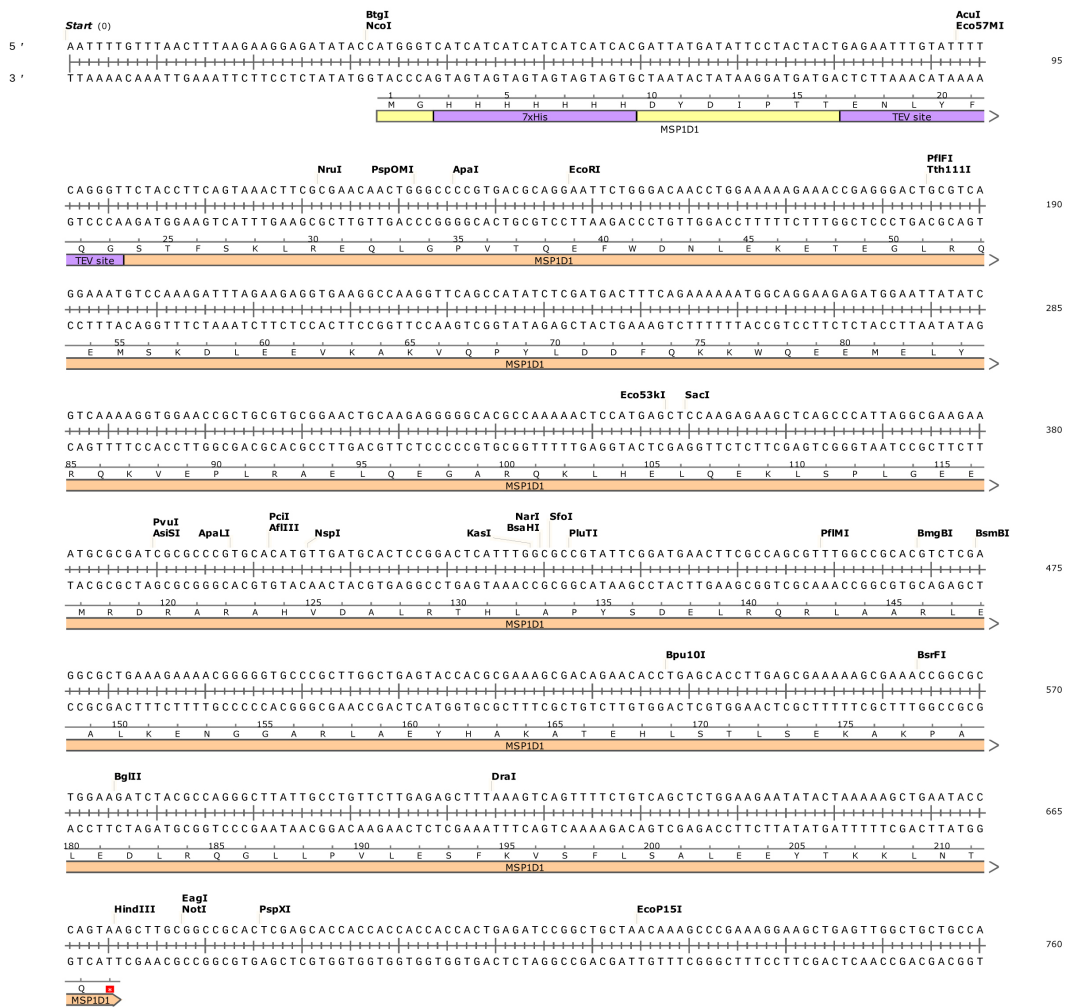


Figure B.2: Sequencing result for pMSP1D1 executed by Eurofins Genomics GmbH using primers for the T7 promoter and terminator. Shown are the nucleotide sequence, the corresponding amino acid sequence as well as the restriction sites. For representation the software SnapGene[®]3.3.3 was used.

B. Plasmids and protein constructs

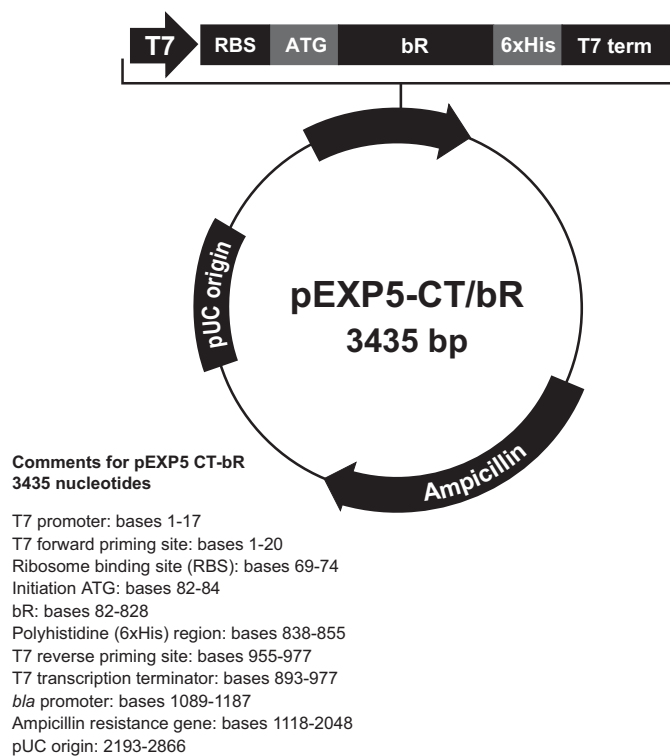


Figure B.3: Plasmid map of pEXP5–CT/bR from Invitrogen™ |Thermo Fisher Scientific Inc., USA.

B. Plasmids and protein constructs

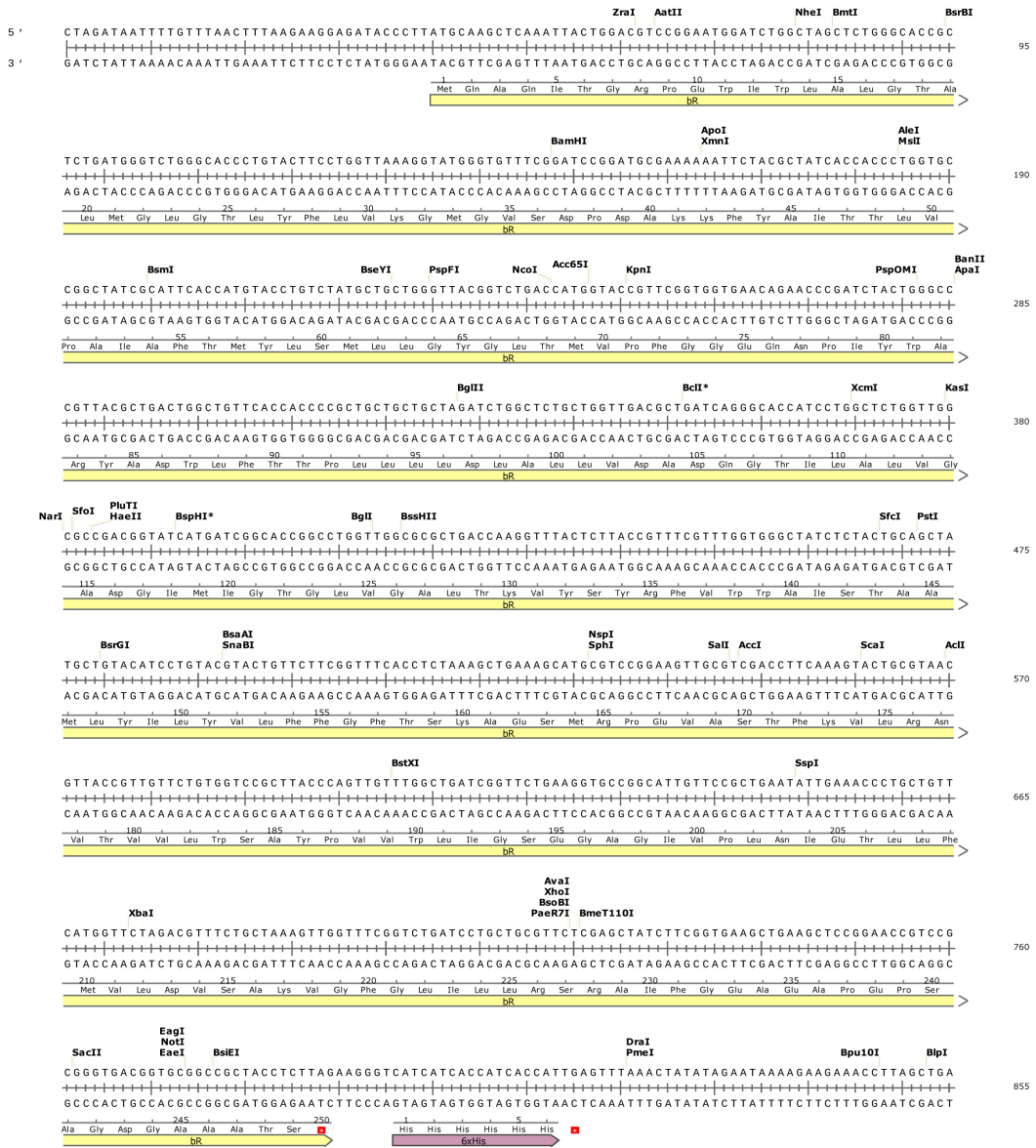


Figure B.4: Sequencing result for pEXP5-CT/bR executed by Eurofins Genomics GmbH using primers for the T7 promoter and terminator. Shown are the nucleotide sequence, the corresponding amino acid sequence as well as the restriction sites. For representation the software SnapGene[®]3.3.3 was used.

B. Plasmids and protein constructs

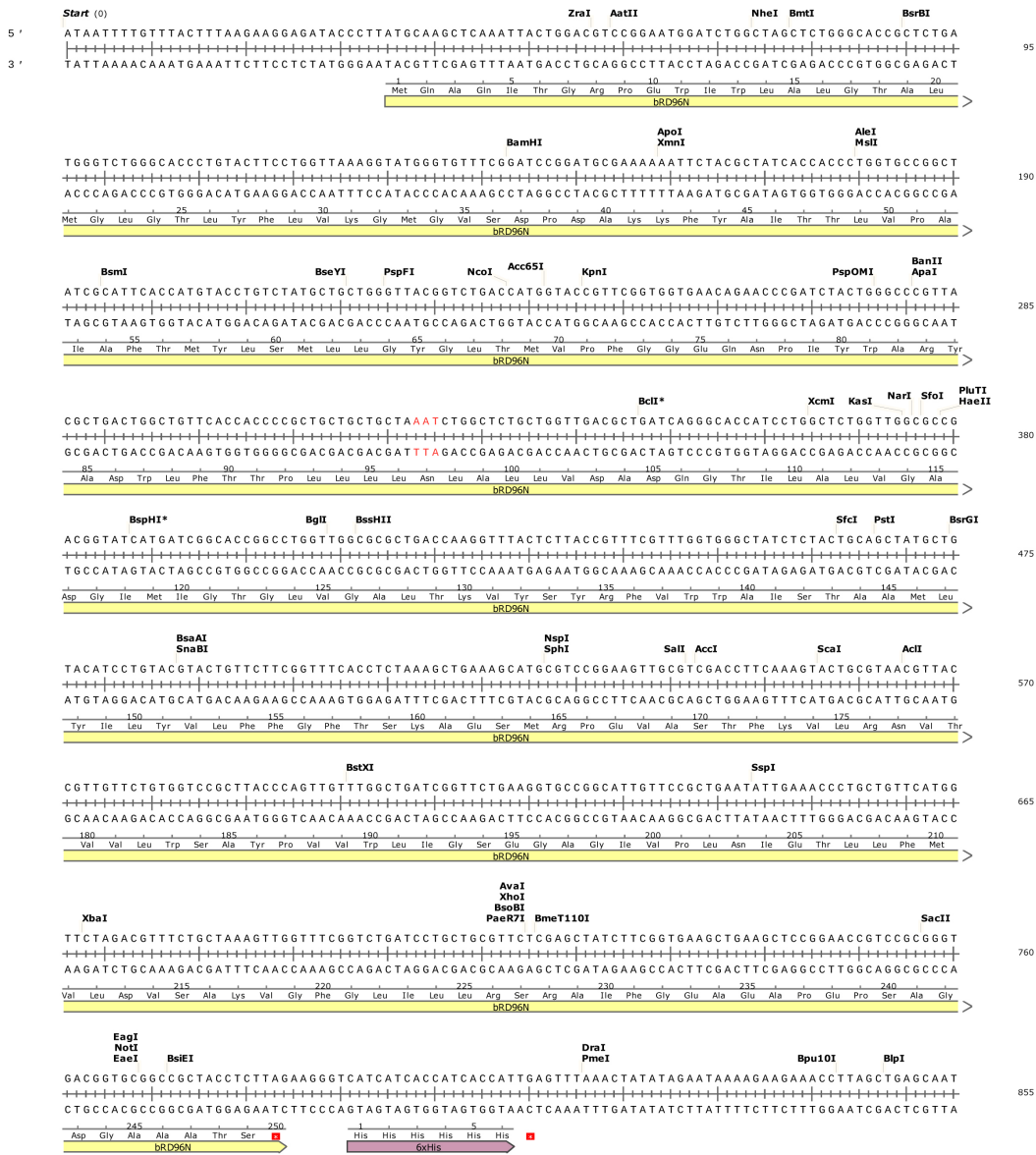


Figure B.5: Sequencing result for pEXP5-CT/bRD96N executed by Eurofins Genomics GmbH using primers for the T7 promoter and terminator. Shown are the nucleotide sequence, the corresponding amino acid sequence as well as the restriction sites. The mutation D96N is highlighted in red. For representation the software SnapGene[®]3.3.3 was used.

B. Plasmids and protein constructs

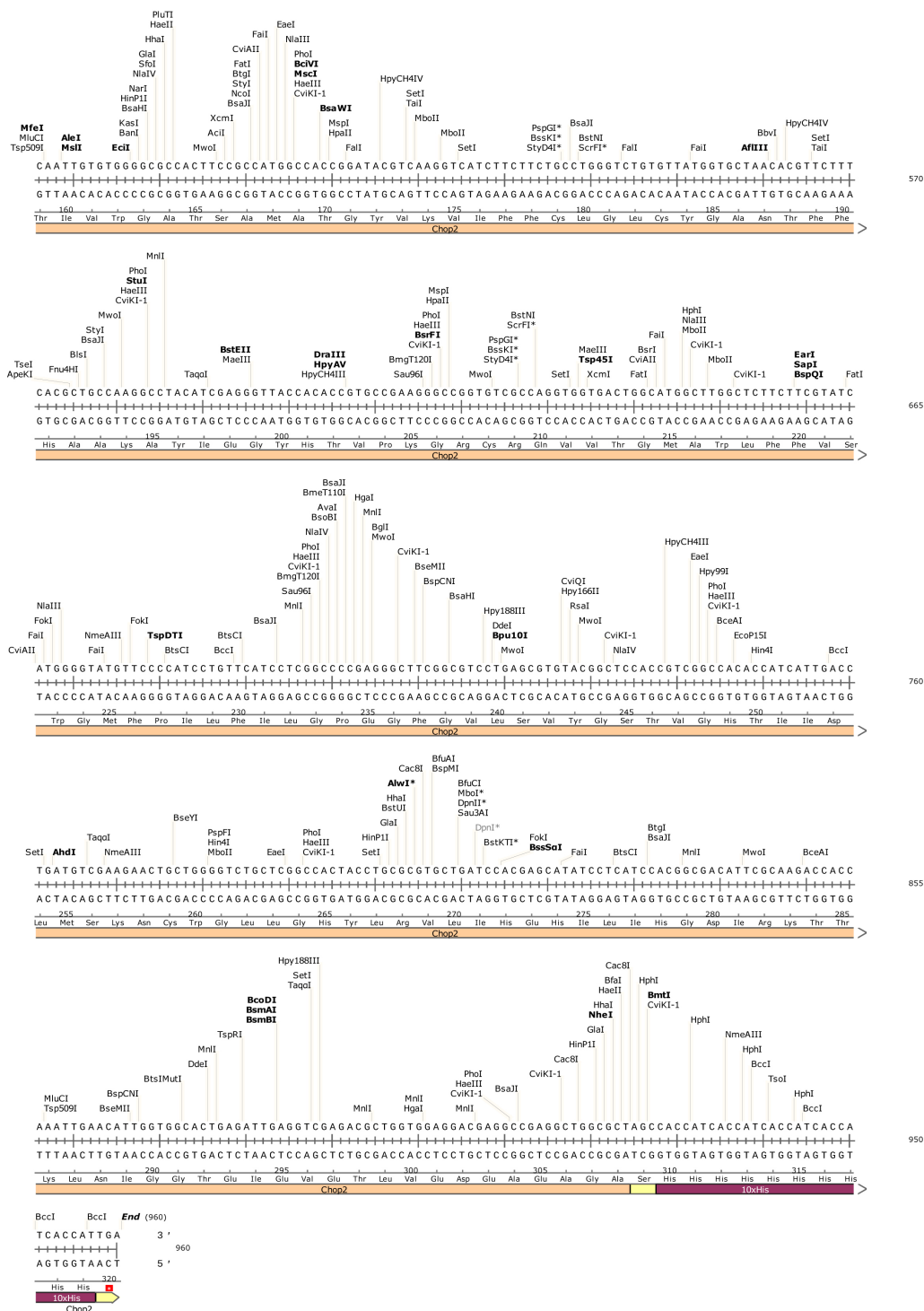
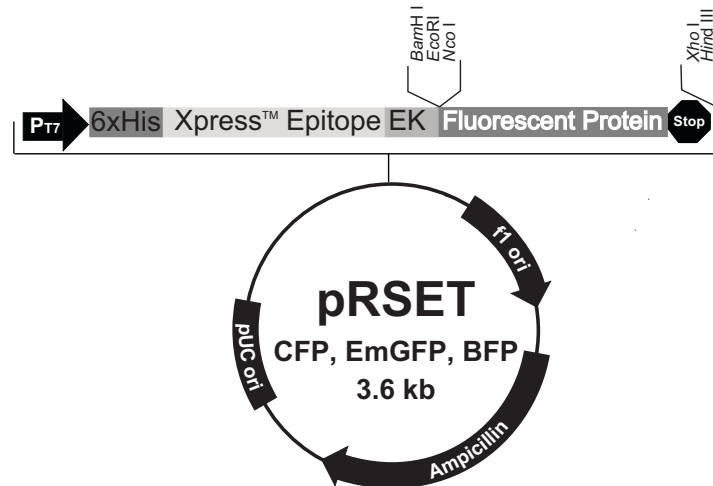


Figure B.8: Sequence of Chop2 in pET27b/Chop2. data by courtesy of Dr. Ramona Schlesinger, FU Berlin, Germany. Shown are the nucleotide sequence, the corresponding amino acid sequence as well as the restriction sites. For representation, the software SnapGene®3.3.3 was used.

B. Plasmids and protein constructs



Comments for pRSET/CFP, EmGFP and BFP
3600 nucleotides

T7 promoter/priming site: bases 9-28
6xHis tag: bases 101-118
T7 gene 10 leader: bases 122-154
Xpress™ epitope: bases 158-181
EK cleavage site: bases 167-181
Fluorescent Protein (CFP, EmGFP, BFP): bases 209-928
T7 reverse priming site: bases 987-1006
T7 transcription terminator: bases 948-1084
f1 origin: bases 1148-1603
bla promoter: bases 1635-1739
Ampicillin (bla) resistance gene: bases 1734-2594
pUC origin: bases 2739-3412

 invitrogen™

Figure B.9: Plasmid map of pRSET–EmGFP from Invitrogen™ | Thermo Fisher Scientific Inc., USA.

B. Plasmids and protein constructs

Table B.1: Protein parameters calculated by means of the online tool Prot-Param.

ORF including MSP1D1 (Fig. B.2):	
Number of amino acids:	212
Molecular weight:	24792.8 g/mol
Theoretical pI:	5.86
Extinction coefficient:	21430 M ⁻¹ cm ⁻¹ (at 280 nm measured in water)

bR (Fig. B.4):	
Number of amino acids:	249
Molecular weight:	26931.8 g/mol
Theoretical pI:	4.83
Extinction coefficient:	60390 M ⁻¹ cm ⁻¹ (at 280 nm measured in water)

bRD96N (Fig. B.5):	
Number of amino acids:	249
Molecular weight:	26930.8 g/mol
Theoretical pI:	4.97
Extinction coefficient:	60390 M ⁻¹ cm ⁻¹ (at 280 nm measured in water)

ORF including SopI (Fig. B.6):	
Number of amino acids:	234
Molecular weight:	25422.8 g/mol
Theoretical pI:	7.27
Extinction coefficient:	48360 M ⁻¹ cm ⁻¹ (at 280 nm measured in water)

ORF including SopII (Fig. B.7):	
Number of amino acids:	230

B. Plasmids and protein constructs

Molecular weight: 24682 g/mol
Theoretical pI: 7.97
Extinction coefficient: 42400 M⁻¹cm⁻¹ (at 280 nm measured in water)

ORF including Chop2 (Fig. B.8):

Number of amino acids: 319
Molecular weight: 35675.3 g/mol
Theoretical pI: 6.32
Extinction coefficient: 76360 M⁻¹cm⁻¹ (at 280 nm measured in water)

ORF including EmGFP (Fig. B.10):

Number of amino acids: 279
Molecular weight: 31475.3 g/mol
Theoretical pI: 5.81
Extinction coefficient: 29005 M⁻¹cm⁻¹ (at 280 nm measured in water)
